Multiple Imaging Modalities for Investigating Soft Hard Tissue Interfaces

Submitted by Eve Nebbiolo, to the University of Exeter as a thesis for the degree of Doctor of Philosophy in Engineering, May 2023.

Supervisors: Dr Junning Chen, Prof. Francesca Palombo, and Prof. Peter Winlove

Faculty of Environment, Science and Economy (ESE)

University of Exeter

Abstract

Interfaces of hard and soft tissues in the body play a crucial role in processes such as skeletal growth, as well as distributing stresses during load bearing activities. The mechanically dissimilar tissues are able to be studied individually, but how they integrate at the interface, both by collagen, and mineralisation, is an under explored research area. This is of importance due to these interfaces being particularly prone to damage. In the case of the endplate, hypermineralisation of the cartilaginous endplate has been correlated with degeneration of the intervertebral (IVD) discs and chronic lower back pain. For the skull of infants, abnormalities in mineralisation of the cranial sutures leads to deformities of the skull, resulting in increased inter-cranial pressure, and developmental complications for the child. Specific questions addressed in this thesis include, how does the osteocyte lacunae canaliculi network (OLCN) in irregular bones compare to the previously studied long bone?, how are collagen fibres arranged at the soft-hard tissue interfaces?, and how does the mineral density change with distance from the soft-hard interfaces?

This PhD project has investigated these research questions via experimental methods, with the spine experiments using the central section of the 1 year old Lumbar 4-5 ovine samples in the coronal plane, to assess the vertebral body - endplate - IVD interfaces cranial to the IVD. The skulls used intact 6 week old murine samples to assess the suture-cranial plate interface for the interfrontal, sagittal, squamous, and cranial sutures. These were dissected, dehydrated, stained, embedded, and polished in polymethylmethacrylate, followed by multimodal imaging. The imaging techniques used have been confocal laser scanning microscopy, to assess the OLCN, scanning electron microscopy to map the spatial distribution of minerals, and second harmonic generation for investigating the collagen across these mechanically complex tissues.

Analysis for the OLCN in the spine has used Python scripts to quantify the network density, the lacunae density, and the direction of the network with respect to the nearest blood vessel. Quantification of minerals in the skull used Quantitative Backscattered Electron Imaging to get the calcium weight % from the pixel intensity. Polarised second harmonic generation was used to quantify the principle direction of the collagen bundles, as well as the dispersion of the collagen fibres making up the bundles.

Results have been both qualitative and quantitative in this project. Mineralisation patterns in the vertebral endplate (VEP) show heterogeneity, with higher degrees of mineralisation in the mineralised cartilage. The values for canaliculi density within the VEP range from 0.05-0.14 $\mu m/\mu m^3$, similar values reported in long bone, and the collagen across the cartilage and bone interface has the same principle direction, but the cartilage has a greater degree of dispersion. For the suture-cranial plate interface, the mineral density values ranged between 15-22%, with higher values located at the sites of growth, and edges close to non-mineralised tissues. The collagens have continuity across the mineralisation face, with changes in collagen structure to become more ordered once within the bone tissue, or as Sharpey's fibres which span the soft-hard interface. The soft-hard interface, which defines the boundary of mineralised tissue, is spatially distinct from the interface between the major collagen types: type I and type II. This observation is seen in both the spine and the cranial sutures.

This thesis outlines reliable methods to image and quantify the OLCN, mineralisation, and collagen in mechanically dissimilar tissues, and establishes a baseline for future experiments to expand on how these features may change with age or disease. The results are in agreement with similar findings in literature, and are novel in that these specific tissues have not been quantified by their OLCN, mineralisation, and collagen arrangement at this scale before. Findings in this thesis show that there are multiple spatially distinct interfaces of the different constituent components as tissues transition from mineralised to non-mineralised.

Key Words: Collagen; Endplate; Multiphoton Microscopy; Mineralisation; Osteocyte Canalicular Network; Cranial sutures; QBEI; pSHG

Acknowledgements

I would like to acknowledge and thank the people who have supported me in a a variety of ways throughout this PhD. First of all, I would like to thank the biomechanics and biophysics research group, especially Ellen, for the frequent chats in the lab about everything under the sun and always being a warm and welcoming smile in the laboratory. Thank you to my secondary and co-supervisors, Francesca and Peter, who have been great at keeping me motivated and have a contagious enthusiasm for research. I am very grateful to Hong at the Imaging Suite, and Pia at the RILD for letting me book so many hours on the different microscopes across multiple sites for this project.

I want to give my immense gratitude to my principal supervisor, Junning. I could not have asked for a better supervisor, as Junning has not only guided me through developing the skills for research, but has also been a friend who I have enjoyed an excessive amount of coffee with, and has introduced me to some lovely food. Thank you for your patience with me, Junning!

Thank you to my assessors, Professor Andrew Pitsillides and Professor Jude Meakin, for taking the time to assess both this thesis, and meet me for my viva.

I am thankful for my family, who have been there for me as both a source of turkey legs for biomineralisation side projects, as well as a very welcome distraction when I would rather play peek-a-boo with my little nieces.

Meg and Ro, I want to say a huge thanks for the evenings spent being cosy and chatting about politics, and the chaotic holidays that miraculously haven't got any of us severely injured yet. This PhD has honestly been relaxing compared to spending a few weeks in a desert with you guys, yet I look forward to planning our next adrenaline-filled adventure, whilst you take on your PhD.

Finally, thank you to David who has, despite geographical obstacles initially, put up with me throughout the pandemic, made me many cups of coffee in the unmotivated mornings, and now bears the brunt of me converting his VR room into my thesis writing space. Thank you so much for your support and encouragement throughout these last four years.

Acronyms

- **AC** Articular Cartilage
- **AF** Annulus Fibrosus
- **BMD** Bone Mineral Density
- **BSE** Backscattered Electron
- **CaDn** Canalicular Density
- **CaWt%** Calcium Weight %
- **CEP** Cartilage Endplate
- **CT** Computerised Tomography
- **DEXA** Dual-energy X-ray absorptiometry
- **ECM** Extracellular Matrix
- **EDX** Electron Dispersive X-ray
- **EP** Endplate
- **FWHM** Full Width Half Maximum
- **HA** Hydroxyapatite
- **IVD** Intervertebral Disc
- **NP** Nucleus Pulposus
- **OA** Osteoarthritis
- **OLCN** Osteocyte Lacunae Canalicular Network
- **PD** Probability Distribution
- **PSHG** Polarised Second Harmonic Generation
- **PMMA** Polymethylmethacrylate
- **QBEI** Quantitative Backscattered Electron Imaging
- **SAXS** Small Angle X-ray Scattering
- **SEM** Scanning Electron Microscope
- **SHG** Second Harmonic Generation
- **TPEF** Two Photon Excited Fluorescence
- **VEP** Vertebral Endplate
- **WAXD** Wide Angle X-ray Diffration

Contents

List of Figures

List of Tables

Chapter 1

Introduction

The interface between mineralised and non-mineralised tissues in the body, are known as soft-hard tissue interfaces, and are the location of a variety of processes which can both aid, or hinder health. These interfaces are responsible for skeletal growth, and continuously change as we age.

As we get older, the soft-hard interfaces often become hypermineralised, which coincides with other ailments such as the breakdown of cartilage in osteoarthritis (OA), or degenerated intervertebral discs (IVDs) in chronic lower back pain. With an ageing population these diseases are becoming more prevalent, with concerns both arising in patient well being in their day to day life, as well as the economic cost of sick days and treatments [1–5]. The cost of lower back pain in the US projects their national costs to be over $100 billion [6], but osteoarthritis in joints elsewhere in the body are even more prevalent, with direct costs of treatments on their own at £852 million in 2010, a 66% increase from 2000 [7]. However, problems arising at mineralising interfaces is not unique to those older in society. The skulls of infants are known to be soft to ensure safer delivery through the birth canal, and then they harden until what is left of the soft tissue are thin su-

tures between the cranial plates. In some cases of craniosynotosis, one or more of these sutures mineralises prematurely, which then leads to abnormal growth of the skull and health complications for the child.

Due to the nature of how diseases such as OA and back pain progress, the common trait of degeneration of the soft tissue is where the focus has been in research and therapeutics [8, 9]. These changes are notable in that the collagen structure breaks down, and the proteoglycan concentration decreases. The main function of proteoglycans is to bond to water, and so a high concentration increases the osmotic pressure of the tissue [10]. The reduction in swelling pressure with disease means the tissue is unable to resist compression, which is when patients notice that there is pain or limited movement. Treatments for chronic back pain range from pain medication to spinal fusion, where the quality of life for patients post surgery is still compromised [11]. For OA, lifestyle changes and pain medication are the common therapies until entire joint replacement is required. For cases of craniosynostosis, depending on the severity, the child can undergo cranioplasty, a surgical method with still no consensus on which materials are best to use [12, 13].

All of these conditions arise from abnormal behaviour at this soft-hard tissue interface, which is why the interplay among the interface constituents is the focus in this thesis. The aims of this research has been characterising quantitatively the mineral distributions, collagen dispersion and direction, and the network of microscopic channels between cells in bone, known as the osteocyte lacanue canaliculi network (OLCN). By assessing these features across healthy samples, further work can assess how the minerals, collagens, and cellular network architecture changes in the bone and the interface with disease, which could help in

designing specific treatments in the future.

1.1 Thesis Outline

This thesis details on experiments carried out to better understand osteochondral interfaces in terms of their structure and variability. Chapter 2 covers the basic theory required to understand the biology of the samples in these experiments, with the basic constituents outlined initially, followed by the specific anatomy of the soft-hard interfaces in the spine and skull.

Chapter 3 is the theory of the imaging techniques used, and how they are used for imaging the features of interest in this thesis. However, the specifics of each experimental set up are will be outlined in the methods sections of the relevant experiment chapters. The imaging techniques covered include confocal laser scanning microscopy (CLSM), multiphoton microscopy and the processes of second harmonic generation (SHG) and two photon excited fluorescence (TPEF), polarised SHG (pSHG), and scanning electron microscopy with modalities of backscattered electrons (BSE), secondary electrons, quantitative backscattered electron imaging (QBEI), and energy dispersive x-ray spectroscopy (EDX).

Chapter 4 covers the studies on the spine. The quantifiable values of the OLCN and their comparison to long bone is addressed from the images obtained by CLSM, as well as how the mineral density changes between the two soft-hard interfaces of the endplate, and the growth plate, by BSE. The collagen organisation has been investigated by pSHG to assess how the collagen principle direction and dispersion changes across the soft-hard interface of the endplate.

In Chapter 5 the interface of interest is the sutures of the skull, where the focus has been quantifying the mineral density distribution around these sutures

by QBEI, and how this mineral density changes as a function of distance from the nearest soft tissue. The collagen orientation and dispersion has been quantified by pSHG across the sutural-cranial plate interface, with the variations of lamellar and woven bone at this site also taken into consideration so that the different bone types can be compared, by both collagen organisation and mineral density.

Finally, a summary of the key points from each chapter and further work that would be complimentary to the experiments carried out for this thesis are discussed in Chapter 6. The broader aims of this thesis were to assess the interplay between collagen organisation and minerals across the soft-hard interface. Chapter 6 summarises how the changes in collagen are spatially-resolved from the change in mineral density, and so these regions of interest contain multiple interfaces of changing tissue constituents.

1.2 COVID-19 Statement

In March 2020 the University was closed due to a coronavirus pandemic (COVID-19). This led to an extended period of time during my studies where I was unable to access the laboratories and upon reopening, the time in the laboratories was restricted due to maximum building occupancy rules. By the time this closure was announced I had already spent 1.5 years planning the experiments, and so during the University closure, I spent the time optimising the analysis codes for the preliminary data I have previously accumulated, and planning my writing.

Due to the interruption to sample preparation and more importantly, imaging time, there are fewer samples imaged than I had originally planned for, and the data analysed in this thesis is from samples prepared and embedded upon re-opening of the University.

Chapter 2

Review of Tissue Interfaces

2.1 Biointerface bridging soft and hard tissues

The soft-hard tissue interfaces in the body are where there is a change in mechanical properties between mineralised tissue, such as bone or mineralised cartilage, and unmineralised tissue, such as cartilage, tendons, or ligaments. Examples of these interfaces include the bone-articular cartilage interfaces at joints, which provide shock absorbency and low friction movement of joints, and the bone-tendon interface, or enthesis, which transmits the stresses of muscular movement from the soft tendon, to the hard bone [14–16]. This chapter looks into the collagen and minerals across these soft-hard interfaces, the similarities and differences of these components in different tissues, and how the organisation and spatial gradients of these constituent parts give rise to the mechanical differences seen in anatomy.

2.2 Interfacial Constituents and their Spatial Gradients

2.2.1 Organic Constituents

The organic components that make up tissues include collagen, elastin, and other non-collagenous proteins. These components aid in the mechanical properties of the tissues, such as elastin having a strong ability to undergo morphological changes without undergoing plastic deformation [17–19]. The most prominent organic constituent of tissues is collagen, which has over 30 unique types with different properties.

Collagens are made of three left-handed helical protein chains, linked together by various chemical bonds and then coiled to create a right handed triple helical structure. Common primary protein chains have the structure X_{aa} Y_{aa} Gly_{aa}, where Gly_{aa} denotes the amino acid Glycine, and X_{aa} and Y_{aa} represent different amino acids in the triplet, with Proline, Hydroxylysine and Hydroxyproline often present. Glycine is a small amino acid with no side chains, which allows for hydrogen bonding and intermolecular crosslinks to keep the α helical structure stable, as seen in Figure 2.1a [20–23]. Each collagen molecule is held together by intramolecular hydrogen bonds which arise from hydroxyl groups on amino acids, like Hydroxyproline, and is depicted in Figure 2.1b. Whilst stability of the collagen molecule itself is due to intramolecular hydrogen bonds, a few amino acids (Proline and Hydroxyproline) have ring structures, which allow for easier interactions between neighbouring collagen molecules, which is how collagen fibres are formed, shown in Figure 2.1c. The specific amino acid groups are what are responsible for the extent of how much a collagen type forms bundles, and the fibres stability [20, 24]. In order to create the strong fibrillar hierarchy, lysine

(or hydroxylysine) needs to be present in the neighbouring molecules, where the aldehyde or ketone functional groups present undergo a condensation reaction, which create strong Aldol cross links [25, 26]. At the ends of the protein chains, there is the absence of the repeating X_{aa} Y_{aa} Gly_{aa} pattern, which means the helical structure is not viable. The chains of amino acids which make up the ends of the collagen molecule are called telopeptides, and are sites of bonding along the axis of the collagen fibre, creating sites known as gap zones, as the collagenous structure is typically less dense [27–30].

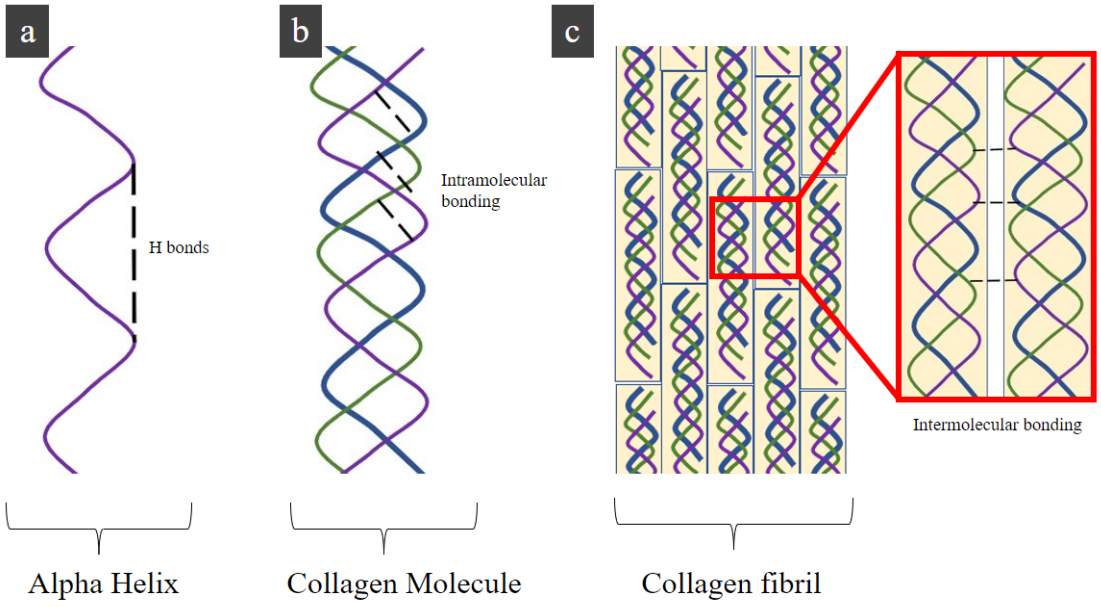

Figure 2.1: Schematics of collagen hierarchy. a) The protein chain forming an α helix by hydrogen bonds between the amino acids. b) The triple helical structure of a collagen molecule, comprising of 3 α helixes, bonded together by intramolecular bonds. c) The bundling of the collagen fibril, consisting of many collagen molecules organised and made stable by intermolecular bonds.

The synthesis of collagens starts within the cells, with the transcription and translation of mRNA into early forms of the protein chain. Hydroxylase enzymes add functional groups such as lysine and proline, and glycosylation occurs on the chain, which results in assembly of the α helix, in Figure 2.1a. The hydroxyl groups on 3 different α chains start bonding, creating the collagen molecule. The organisation of collagen is determined prior to exiting the cell, in protuding plasma

membrane features known as fibropositors [31, 32]. The formation of collagen fibrils occurs outside of the cell, after the collagen molecule is transported by vesicles from the cell to the ECM. In the ECM the lysine and hydroxylysine groups of neighbouring collagen molecules form the fibrils [33]. The cells responsible for the production of collagen vary with the tissue, but fibroblasts and osteoblasts primarily produce type I collagen, whereas chondrocytes primarily produce type II [34, 35].

Each type of collagen is distinguished by the amino acids making up the individual protein chains, but the two types most prominent in the tissues described in this thesis are type I and type II. Type I is the most common collagen in the body, and has an amino acid composition which allows it to form thick fibrils with itself, giving it a similar structure to rope, and is inherently strong due to this entwined pattern [35, 36]. Type II is cartilage-specific, and although does bond with other type II fibrils, it does not form the large bundles as seen with type I. The α helices that make up type II collagen have a higher frequency of hydroxylysine compared to the α helices which make up type I [16].

These fibres undergo tension during mechanical loading and deform to contribute to the larger scale tissue mechanical properties. The differences in amino acid composition mean that type II collagen can more readily bond to the water present in the interstitial fluid [37], which means that the type II rich, and therefore high water potential cartilage can deform under mechanical loading, and the nutrients can flow through the tissue due to its porosity. Type I is common in structures that need to be load bearing, such as bone, tendons, and ligaments [38–40]. The mechanical behaviour of type I collagen is complex in that the elasticity is non-linear at the nanometre scale, with the low strain (0-15%) seeing strain stiffening

of the fibres, whereas above 15% there is strain softening [41].

The cross linking to form fibrils is important for mechanical properties, but too many cross links results in impaired mechanical function of the fibrils [42]. The unfolding of these proteins results in a higher water potential for the collagen structure, which changes the mechanical properties of the entire tissue [43]. Diseases such as osteoarthritis are characterised by a change in mechanical properties of the cartilage resulting from the breakdown of the collagen structure, an increase in tissue hydration, and a decrease in the elastic modulus [44–51]. Changes in collagen which have been shown to reduce the water potential include the glycation (Maillard reaction of a sugar with an amino acid) of collagen, which increases with age [52].

2.2.2 Inorganic Constituents

Hydroxyapatite crystals are the biological minerals that make up one of the inorganic components of the tissue matrix. The chemical formula is $Ca_5(PO_4)_3(OH)$ which forms crystals in platelet shapes that vary in size. The size depends on numerous factors, such as the type of bone, how quickly the mineral is formed, and how recently it was deposited, with dimensions ranging from $15 - 50\ nm$ in width, and $50 - 100\ nm$ or more in length, and a thickness of $2 - 5\ nm$ [53–55].

The synthesis of these apatite crystals starts with mineral forming cells (osteoblasts, chondrocytes, tenocytes, etc.) producing matrix vesicles containing the constituent components of the apatite, such as calcium ions and the phosphate groups. The rate of mineral production is regulated by the presence of enzymes, such as alkaline phosphatase, in these cells [56]. These matrix vesicles have the ability to bind to collagen, where the components inside the vesicle undergo

nucleation, resulting in growth of the hydroxyapatite crystal, until it exceeds the dimensions of the matrix vesicle [57–61].

The spatial distributions of crystal deposition and growth within biological samples is a growing field of research which has advanced with super resolution imaging techniques and with better sample preparation methods [62–65]. Once bone is fully mineralised, the mineral density is not uniform despite values of overall bone density being given and used to characterise certain diseases, such as osteoporosis [66]. The distribution of these minerals plays a huge role in skeletal stability and so more recent research has been focused onto the microscopic and nanoscopic patterns seen in the mineral matrix [67, 68].

On the scale of the osteocyte lacunae canaliculi network (OLCN), when the bone is starting to mineralise the minerals are initially deposited further away from the canaliculi, and in separate mineral patches. These patches grow until they meet each other, and form a dense mineral wall. Once bone is matured there is a higher concentration of minerals adjacent to the canaliculi, as well as nearer the Haversian canal of the osteon that can be quickly reabsorbed and used for remodelling and calcium homeostasis [69, 70].

These minerals are initially deposited within the gap zones of the collagen fibrils, where they then nucleate and grow [30, 71]. Growth of the crystals occurs longitudinally along the axis of the collagen fibril, independent of neighbouring bundles [72] and occurs both within the collagen bundles, as well as outside of them [53, 73].

The role of these minerals is to provide rigidity to the bones, as well as provide a reservoir for calcium for pH regulation in other regions of the body [74–76]. A decrease in mineral density causes bones to have lower stiffness and

strength, which are vital mechanical properties for the load-bearing capabilities of the skeleton [77]. Despite the minerals providing rigidity to the tissue, the crystals themselves also deform, albeit to a lesser extent than the other components of the tissue [78].

The apatite crystals can have impurities that are suspected to decrease the crystallinity of the mineral component [79]. The most common variations in the crystal composition is the phosphate group (PO_4) being substituted by a carbonate group (CO_3) [54, 80], but other trace amounts of impurities such as magnesium and sodium ions can also be detected [81]. Bone that is not being remodelled, and therefore not undergoing a process of frequent mineral absorption and deposition, gradually undergoes this substitution of a carbonate molecule for the phosphate chemical group in the crystal [82]. The ratio of carbonate to phosphate content is then an indicator of the remodelling rate, with a high carbonate to phosphate ratio indicating a lower remodelling rate due to more phosphate groups being substituted. This ratio to assess remodelling has shown that older bone samples have a lower remodelling rate, and this ratio itself can also vary between regions of the same bone sample [64, 82–85].

The overall packing of the apatite crystals determines the bone mineral density (BMD), which is a major factor in bone health, with a decrease in BMD resulting in osteoporosis and greater risk of fracture [65, 86–89].

2.2.3 Variations of bone organisation

At the macroscale, there are four categories of bones found in the human body. Long bones make up the axis of limbs, are longer than they are wide, such as the femur and humerus, and are typically load bearing bones that provide strength.

Short bones share similarities in structure to long bones, but without the diaphysis. They are found in hands and feet, such as the carpal bones, and with several aligned together connected by joints, provides dexterity [90]. Flat bone examples include the skull and ribs, and are flat with curvature to give their shape. These are located in the body where joints would not be beneficial and protect internal organs [91, 92]. Irregular bones are ones which do not have a defined characteristic shape, and are found in the bones which make up the spine. The complexity of the irregular bone structures in the spine mean that they fulfill the role of load bearing and form a protective sheath around the spinal cord [93, 94].

On a smaller scale, there are two main bone structures which make up all of these structures which aid in their functions. The two main types of bone discussed in this thesis are compact (or cortical), and spongy (or cancellous/trabecular). Cortical bone is dense, with only 30% of the volume being occupied by vascular channels, and is often what makes up the surface of the bone [95]. Cancellous bone appears as sponge, with the mineralised tissue forming trabeculae struts around unmineralised regions, which contain the marrow, adipose, and blood vessels [96].

Cortical bone consists of mostly fibrolamellar bone which has collagen densely packed within lamellae and is remodelled to have directionality to sustain mechanical loading [73, 97]. In cortical bone there is a small amount of woven bone characterised by a disorganised collagen arrangement and is seen as a primary bone, laid down rapidly, before remodelling occurs in the periosteum [98, 99].

The hydroxyapatite crystals have the same shape in both lamellar and woven bone, but the overall size of the crystals is smaller in the woven [53]. Woven bone is typically more highly mineralised than lamellar [100–104], but some reports

have claimed otherwise [105]. The minerals in both bone types are crystalline at the nanoscale, but due to woven bones less ordered collagen arrangement, the apatite crystals on the tissue level are also less ordered, compared to lamellar bone [53].

Osteons are a repeating unit of bone present in large mammals and serve as a building block to ensure nutrients can be accessed easily within large structures, and to aid in strength of the bone [106–109]. They contain a central blood vessel within a Haversian canal, and form a cylindrical shape with concentric rings of collagen and osteocytes connected by the canaliculi, shown as a diagram in Figure 2.2. The shape of the osteon structures and the arrangement of them within the bone is dependent on both lifestyle factors, as well as genetics. They typically have a diameter of $\approx 100 - 150\ \mu m$, and lengths ranging from $1 - 10\ mm$, depending on species, age, sex, and lifestyle [107, 110–113].

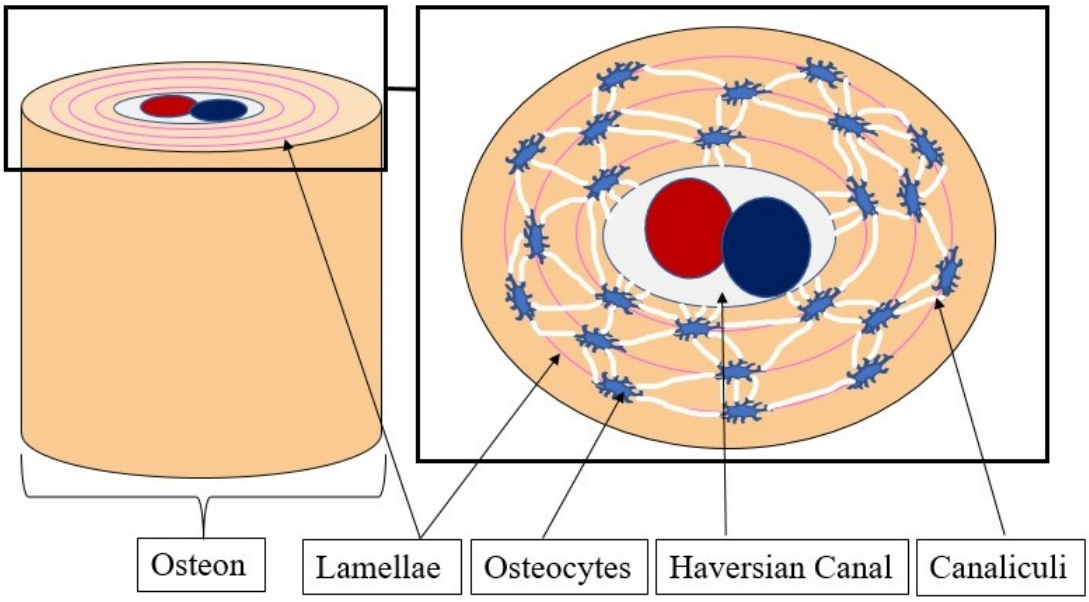

Figure 2.2: Schematic of osteon structure, containing the central Haversian canal, which houses the blood vessels, surrounded by concentric lamellae of type I collagen (pink) and the osteocytes (blue) which are connected to each other via canaliculi (white).

2.2.3.1 Endochondral Ossification

Endochondral ossification is the process where the mesenchyme undergoes chondrogenesis (i.e. differentiates into cartilaginous tissue), which then has an ossification centre where mineralisation of the tissue occurs to become the mineralised bone tissue [14].

On a smaller scale, the mesenchymal stem cells (MSC) differentiate into chondroblasts, which secrete a matrix rich in collagen and proteoglycans, as seen in Figure 2.3a. These cells then mature into chondrocytes which then secrete molecules that promote mineral deposition (Figure 2.3b) and the invasions of blood vessels into outer membrane of the bone. The nutrients provided by the blood vessels causes the mesenchymal stem cells to differentiate into osteoblasts, which excrete minerals until they are surrounded by a mineralised matrix shown in Figure 2.3c. Since bone is a dynamic tissue, this also occurs as osteoclasts start dissolving the minerals to initially create the medullary cavity. Whilst the primary ossification centre is creating recognisable bone from hyaline cartilage, the chondrocytes gather towards the longitudinal areas of the shaft, repeating the same behaviour and therefore creating growth of the bone in the longitudinal axis. The chondrocytes form columns for longitudinal growth at the neck of the epiphysis as secondary ossification centres occur within the epiphysis (Figure 2.3d). The use of these secondary ossification centres allow structural integrity of the skeleton, whilst the chondrocytes remain present within a thin line of cartilage known as the growth plate, so that growth of the bone can still continue after birth, as seen in Figure 2.3e [14, 114].

This process only lasts so long and eventually the growth plate becomes mineralised, fusing the ossified regions of bone together and ending the process of

endochondral ossification in that bone, as seen in Figure 2.3f. Throughout growth and after the growth plate has fused, there is still remodelling in the bone. The fusion of the growth plates occurs between the end of puberty and 25 years old for humans [14, 115–118].

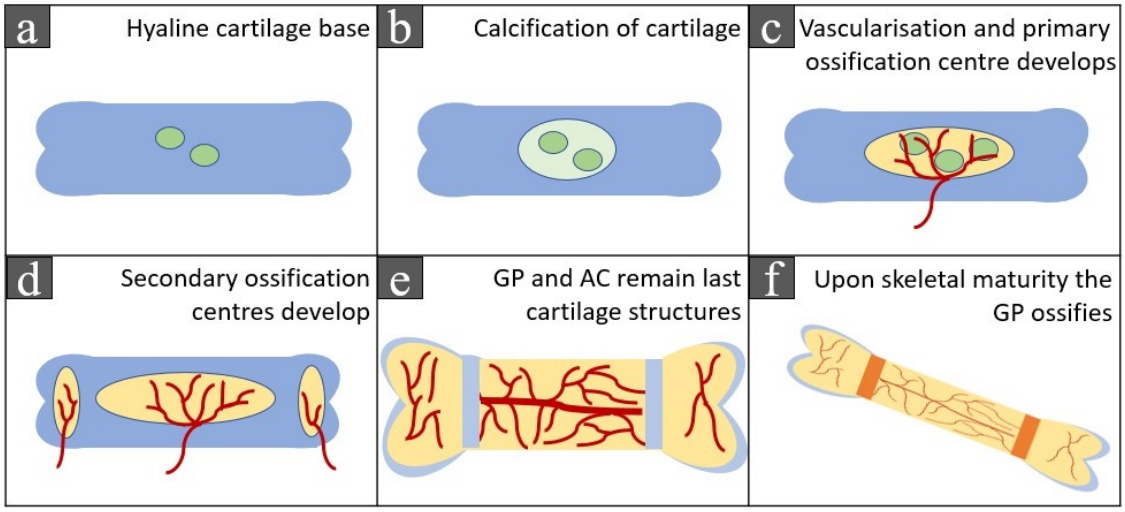

Figure 2.3: Diagram showing the steps of endochondral ossification. a) The MSC first form a hyaline cartilage tissue. b) The chondrocytes then promote the calcification process and in c) the blood vessels enter the tissue and the ossification centre is formed. d) Growth of the primary ossification centre and the development of secondary ossification centres at both ends of the long bone. e) Vascular bone tissue is established throughout the tissue with the only cartilage remaining being at the very peripheries as articular cartilage (AC), and at the growth plate for continued longitudinal growth. f) At the end of endochondral ossification the growth plates become ossified, and longitudinal growth stops. Only remaining cartilage is the AC at the peripheries.

2.2.3.2 Intramembranous Ossification

Intramembranous growth of bone occurs in bone tissues like the cranium, and the the radial direction of long bones. The initial step of this process is to have a base of collagen rich tissue with MSC, as seen in Figure 2.4a. The MSC differentiate into osteoblasts and secrete an osteoid matrix, which mineralises to become the ossification centre [119], as seen in Figure 2.4b. The osteoblasts surrounded by the matrix then further differentiate into osteocytes [119–121] (Figure 2.4c), and osteoprogenitor cells (stem cells partially differentiated to have characteristics of

bone cells) neighbouring this ossification centre then become osteoblasts and this process is repeated as the bone grows, shown by Figure 2.4d. The different structures of trabeculae vs cortical depend on if the initial osteoid is secreted around an existing capillary, seen in Figure 2.4e. Osteoid which calcifies with a porous network of capillaries will be less dense than the neighbouring tissue with just the osteoid and cells present, and so this differentiation creates a dense cortical shell, and the growth of the mineralised tissue occurs at the boundaries, as seen in Figure 2.4f.

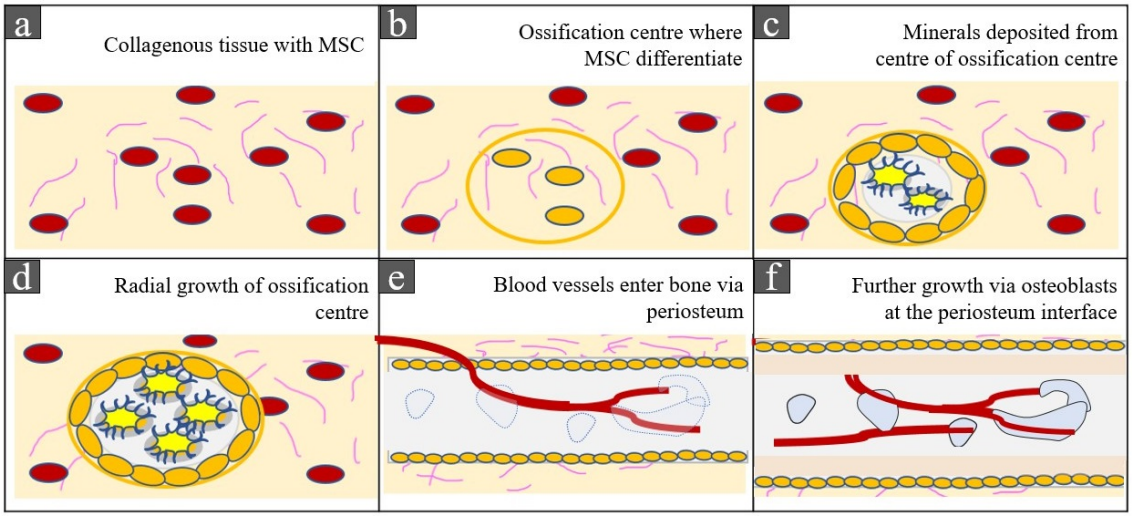

Figure 2.4: Schematic of the process of intramembranous ossification. a) The tissue starts of as fibrous tissue with undifferentiated mesenchymal stem cells (red). b) The MSC differentiate into osteoblasts (yellow) in an area known as the ossification centre (yellow ring). (c) These osteoblasts deposit minerals until they mature into osteocytes (light yellow with blue outline), and osteoblasts at the edge of the ossification centre continue to deposit minerals for growth of the ossification centre in (d). Vascularisation of the bone occurs in (e) with blood vessels (red lines) entering the mineralised tissue through the periosteum. (f) The bone is established with a blood supply and a cortical shell (light orange), with the potential for continuous growth.

2.2.4 Cells

When it comes to cells in specific tissues, they are specialised to maintain and regulate the matrix around them. Since the following experiments look into bone and cartilage, the types of cells most prominent are osteocytes and chondrocytes,

and with fibroblasts being present in tissues such as the sutures and annulus fibrosus. The origins of these cells are the MSC, with differentiation pathways of each summarised in Figure 2.5.

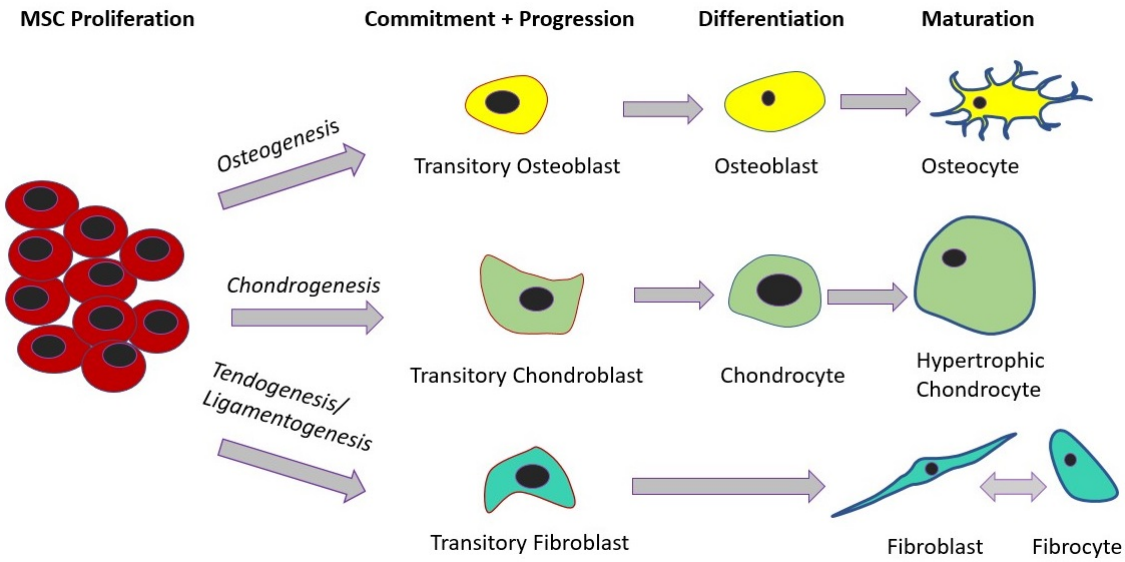

Figure 2.5: The cell differentiation pathways for osteocytes, chondrocytes, and fibroblasts. All originate from stem cells, which proliferate and then undergo either osteogenesis, chondrogenesis, or tendo/ligamentogenesis to eventually differentiate into the matrix regulating cells.

2.2.4.1 Chondrocytes

Chondrocytes have a slower metabolic rate than most cells due to the anaerobic environment they reside in [122]. Their morphology is dependent on location within the cartilage, with proximity to a blood supply and the health of the tissue being two major factors which influence their shape [16, 123–125].

Since articular cartilage is avascular, the more spherical chondrocytes are present closer to the bone, and more flat and oblique are located at the superficial region [16, 126]. This is because the chondrocytes are relying on the diffusion of nutrients from the vascularised subchondral bone. A larger surface area to volume ratio in the superficial zone means that the uptake of nutrients by diffusion is more efficient, and means that the chondrocytes remain viable [127].

However, some studies show that in mature cartilage, the majority of nutrients are accessed from the synovial fluid rather than the bone. This contradicts the theory that the vascularised bone is the main nutritional pathway for the cartilage, and that hypermineralised cartilage inhibits the flow of nutrients, which then affects the health of the soft tissue [128]. The immediate environment for chondrocytes is the pericellular matrix (PCM), which makes up the unit known as a chondron [129–131]. This PCM is a region of collagenous matrix, with a distinct composition and mechanical role than the surrounding extracellular matrix (ECM) of the cartilage [16, 131–133].

Work on the mechanical properties of the chondron structure against isolated chondrocytes evidences towards the pericellular matrix component resisting compression to prevent chondrocyte damage [134–137]. Whilst the pericellular matrix prevents excessive force on the chondrocyte itself, the process of mechanotransduction converts mechanical stress applied to the pericellular matrix and chondrocyte into biochemical signals which then stimulate the chondrocyte to build and repair the ECM as required [132]. In the superficial and transitional zones of articular cartilage (AC) the chondrocytes produce collagens of type II and IX, which aids in the ECMs role of distribution of both compressive and tensile loads [125, 138]. Chondrocytes in the deep zone also produce a different collagen type, type X which coincides with hypertrophic chondrocytes, and the subsequent hypermineralisation of cartilage [138].

The mineralisation of cartilage is a process carried out by the hypertrophic chondrocytes which produce the matrix vesicles containing the core components, described earlier in this chapter (section 2.2.2) [58, 59, 139].

2.2.4.2 Osteocytes

Osteocytes are matured osteoblasts that have become encased in the mineral matrix. The typical shape of these is an elongated cell body with cell processes emerging in all directions. These features are typical of osteocytes but can exhibit changes to their morphology and dendrite number depending on the mechanical and chemical environment each one is in [74, 140–145].

The void in the mineral matrix where the cell body resides is the lacuna, and the cell processes branch out into the canaliculi, small microscopic channels which create a network between neighbouring osteocytes where fluid and nutrients can be transported, and biochemical and mechanical signals can be transmitted. This network is the osteocyte lacunae canaliculi network (OLCN).

The osteocytes and their lacunae have different shapes and orientations based on the principle loading direction, and exhibit different cell membrane stiffnesses which alter the strain response on the osteocyte [140–144]. Osteocyte body shapes and sizes also vary with the immediate mineral environment. A lower bone mineral density (BMD) has been associated with rounder and larger osteocytes, whereas higher BMD regions have more oblate osteocyte cell bodies, with a larger surface area to volume ratio [145].

The OLCN is the series of microscopic channels connecting the lacunae to each other in boney tissues. It is a large network, capable of multiple roles to assist bone health [146]. The three main roles of the OLCN are: mineral homeostasis; transport of nutrients and waste disposal; and mechanosensation.

Mineral homeostasis is the process of transferring mineral ions, primarily calcium, Ca^{2+}, to where they are needed most. This isn't just for bone health, in the case of aiding remodelling, but is also for the overall working of the human body,

such as these being used to regulate blood pH [14, 147, 148]. The distribution of minerals mentioned previously means there is a reservoir of usable calcium ions to aid in rapid remodelling and homeostasis, without compromising the structural integrity of the bone [69, 70].

For the transport of nutrients, there has to be movement of the fluid which resides in the OLCN. Small molecules have the ability to diffuse through the mineral matrix, but larger molecules require the OLCN network and the medium of the interstitial fluid for efficient transport [149–151]. Mechanical loading of the tissue makes the process of nutrient, waste, and signalling molecules flow through the canaliculi more efficient [152, 153].

The OLCN has multiple features which contribute to its collective mechanosensitivity [154–156]. The orientation of oblate lacunae has significance to the microfracture risk in bones that have a dominant loading direction according to FEA models, but in osteporotic fracture in biological samples the data is varied and inconclusive [157, 158]. Within the canaliculi, the interstitial fluid used for transporting nutrients is also rich in ions, and the cell processes are tethered to the canaliculi walls which ensures sensitivity to the hydraulic, electrical and chemical signals that are transmitted through the interstitial fluid [149, 159].

Communication between osteocytes which regulate these processes can be simplified into two categories, volume transmission, which involves the use of biochemical signals such as hormones, and wiring transmission, which includes mechanical strain, such as movement of fluid [160, 161].

2.2.4.3 Fibroblasts

Fibroblasts are the active form of fibrocytes, depositing a range of organic ECM components for the soft tissue in which they are situated [162]. The shape of cultured fibroblasts from different sites has shown to be similar, with an elongated spindle shape, which is seen throughout healthy tissues in the body [163, 164]. Changes in fibroblast morphology occur when they differentiate into fibrocytes, a reversible process, or upon certain pathologies, resulting in excessive production or loss of ground substance in the ECM [165–167].

Fibroblasts are sensitive to biochemical, physical, and mechanical conditions that affect their behaviour [168]. Compression stresses have been shown to promote cell proliferation in cardiac tissue [169, 170], and within sutures mechanical stimulation results in greater production of collagen by the fibroblasts [171].

2.3 Physiological Functions of Biointerfaces

2.3.1 The Vertebral Endplate

2.3.1.1 Embryonic Development of the Spine

The vertebral bodies of the spine grow by endochondral ossification, the same as long bones, but their embryonic origins vary slightly as the intervertebral disc (IVD) contains remnants of an evolutionary milestone: the notochord [8, 172]. The notochord structure is what differentiates the phylum 'Chordata' and is the first structure that resembled a skeletal support for long organisms. During embryonic development, the notochord becomes surrounded by sclerotome, which later become the vertebrae and annulus fibrosus (AF) [173]. Once the sclero-

tome starts to differentiate into AF and vertebrae, the notochord segments contract away from the vertebrae to reside within the AF. The structure that was once the notochord, becomes the nucleus pulposus (NP), and by the time humans are born, the vertebrae, AF and NP are all distinguishable by their distinct mechanical properties [173]. The formation of the cartilage endplates (CEP) is combined with that of the IVD, but is less understood. The contraction of the notochord creates a continuous structure (AF) around the NP, and the caudal and cranial sections of this structure later differentiate into the CEP [174].

2.3.1.2 The Vertebral Body Structure

The vertebral bodies are irregular bones, comprising of trabecular bone, surrounded by a dense cortical shell. They are formed by endochondral ossification, and contain two cartilaginous growth plates or rings near the caudal and cranial ends. The vertebral bodies are separated from each other by an intervertebral disc and two endplates, depicted in Figure 2.6.

There are 33 vertebral bodies, and in the coccyx, and in some cases the sacrum, the vertebral bodies become fused together. The volume of each vertebral body depends on the location, with larger volumes seen in the lumbar region [175]. Adjacent posteriorly to the vertebral bodies are the vertebral arches that help house the spinal cord and form connections by muscle and ligament connections [66, 173].

The internal structure of vertebral bodies contains trabecular bone surrounded by cortical bone and the endplates, shown in the diagrams in Figure 2.6.

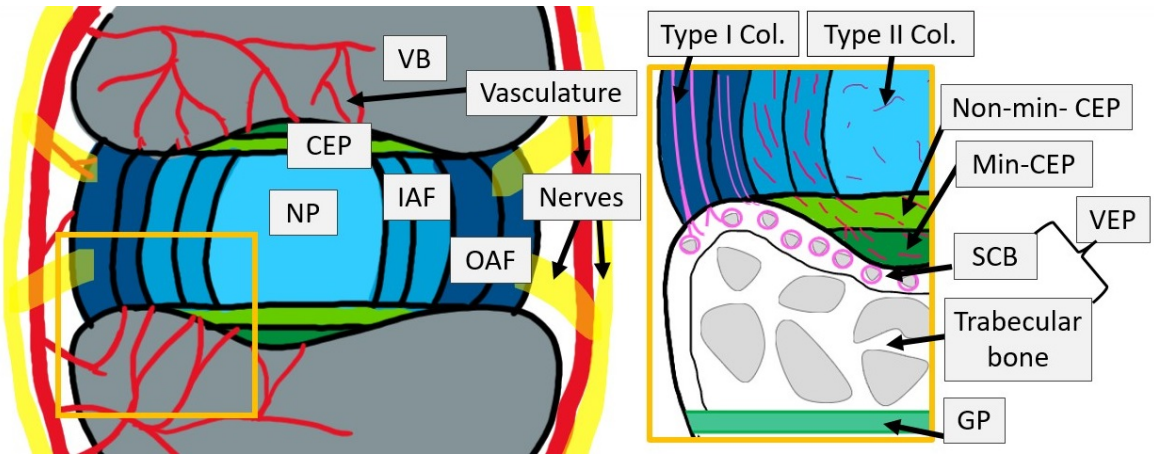

Figure 2.6: The structure of the spinal motion segment, showing the intervertebral disc (blue) between two cartilaginous endplates (green) and vertebral bodies (grey). The vasculature is shown in red, and the nerves in yellow. The boney structures of the vertebral body and collagen arrangement at the interface is shown in the orange box, with the collagen being depicted as pink.

2.3.1.3 The Intervertebral Disc Structure

The intervertebral disc (IVD) contains a gelatinous nucleus pulposus (NP) (light blue in Figure 2.6), peripherally surrounded by the annulus fibrosus (AF) [16, 173] (blue and darker blue in Figure 2.6). The NP is a hydrated tissue with a higher water potential than the surrounding tissues, and the collagen network has a random orientation [173, 176, 177]. The AF by comparison is less hydrated, and the concentric rings are made up of collagen bundles with alternating directions [178–180]. The AF collagen types vary between the rings, with a higher type II content in the central rings next to the NP, that decreases radially, and type I which has a lower content in the central rings, but gradually becomes the dominant collagen type at the peripheries [181, 182], shown by the pink lines in Figure 2.6. This varying structure allows the IVD to aid in load bearing and flexibility by having a deformable central NP that can distribute stress, and the fibrous outer AF with alternating layers that prevents excessive bulging of the IVD [183–185]. The cells present in the IVD also vary, with remnants of notochord cells, which are

morphologically similar to chondrocytes, found in the NP. In the AF the cells are fibroblasts, with the more slender, and more characteristically fibrous cells being found in the peripheries where there is a higher content of type I collagen [182].

The variation in the IVD's structure has an important role for its function. The randomly orientated, type II dominant collagen network in the NP means it deforms readily under load. The concentric rings of the AF that gradually increase in type I collagen content from the centre to the peripheries allows some deformation to occur in the centre, but very little changes at the edges. Having the deformable centre allows for flexibility, whereas the firmer peripheries means the disc does not excessively bulge and come into contact with other tissues, such as the nervous tissue shown in yellow in Figure 2.6 and the spinal chord [186, 187].

2.3.2 The Endplate: Structure and Role

The endplates (EPs) of the spine contain several distinct regions, and there is variation of terminology used in literature with what specific structures constitute as the endplate [188–192]. In this thesis, we followed the terminology used by Newell, Ashinsky, Rodrigues, et al [186, 188, 189], to define this interface. There is the non-mineralised hyaline-like cartilaginous EP that borders the NP and inner AF, shown in light green in Figure 2.6; the mineralised cartilaginous EP, which is adjacent to the non-mineralised EP, and the bone, shown as a darker green in Figure 2.6. The vertebral EP, or sometimes referred to as the boney EP, is the region between the cartilaginous EP and the growth plate, shown in Figure 2.6. This multilayered structure between the NP and AF of the IVD, and the growth plate, is collectively known as the endplate (EP), with each layer having distinct mechanical and biochemical properties to aid in specific roles.

The first role of the cartilaginous endplate (CEP) is to be a nutritional pathway to the IVD. The pores in the mineralised CEP allows nutrients to flow into the non-mineralised CEP and IVD, from the vascular boney tissue, and for metabolic waste to flow out [193, 194]. This is essential for the health of the IVD, as the IVD is the largest avascular tissue, which means without fluid flow through the endplates, the cells in the IVD would not be viable, and the IVD ECM would not be regulated [195–199].

Another role of the CEPs is to distribute loads. The non-mineralised CEP allows the load to be distributed more evenly across the entire IVD, so that there is less risk of damage to the IVD, and then to the vertebral bodies themselves [184, 200, 201]. The mineralised CEP has different mechanical properties due to the minerals, resulting in less deformation under load than the neighbouring non-mineralised CEP.

The mineralised CEP is thought to aid in anchoring the unmineralised EP and IVD, to the mineralised bone of the vertebral endplate (VEP), to reduce the risk of fracture at the interface between the CEP and VEP [202, 203]. The biomechanical environment of the EP exhibits six degrees of freedom, in the form or tension, compression, and torsion [204], and frequent locations of fracture in the spine include the tidemark (the interface between non-mineralised and mineralised tissues), and at the cement line (a boundary line within mineralised tissues usually associated with osteon boundaries in bone as well as the interface between mineralised cartilage and bone) [205–208].

The collagen content in the CEP is both type I and type II, and stems from the collagen in the inner AF. In the VEP the collagen is predominantly I, and in animal models appears to be similar to the epiphysis seen in long bone by hav-

ing a cortical shell surrounding trabecular bone, and a growth plate which fuses upon skeletal maturity. However, the visual similarity of the VEP is only relevant for some animal models [209, 210]. The main differences are that in humans and primates, there is the epiphyseal ring peripherally, and the growth plate cartilage is adjacent to the CEP, leading some publications to include the growth plate cartilage as part of the endplate [210–213]. Whereas in ovine samples, the CEP borders the subchondral bone (SCB), and the growth plate cartilage is surrounded by boney tissue on either side.

The difference between the epiphyseal ring structure seen in primates, and the growth plate in other mammals is shown in Figure 2.7.

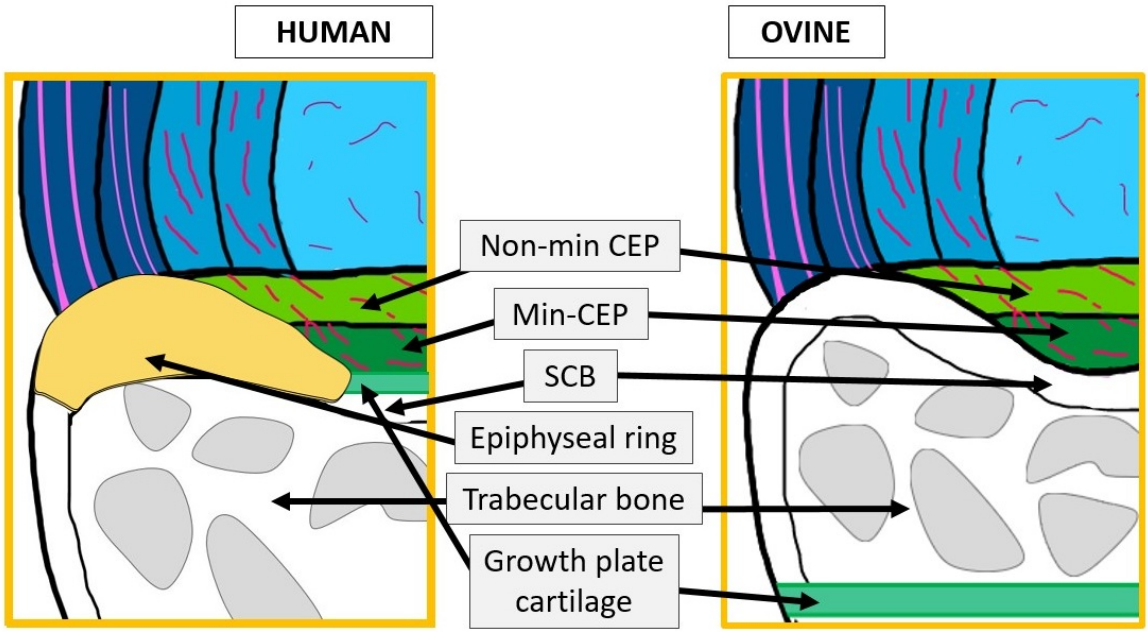

Figure 2.7: Diagrams of how the interface between vertebral bodies and IVDs differ between human and ovine samples. In humans the growth plate cartilage is adjacent to the CEP and there is an epiphyseal ring, whereas in the ovine, the growth plate is separated from the CEP by the SCB and trabecular bone.

The boney structure of the VEP has a varied structure within itself. Adjacent to the mineralised CEP and AF is a cortical shell, composed of osteons, visible by the Haversian canals and concentric rings of collagen and cell lacunae [14, 203]. Further into the VEP in animal models, there are marrow channels separated with

a trabecular bone structure characterised by continuous long bundles of collagen following the axis direction of the trabecular bone. Humans have these structures as well but, due to the absences of a growth plate and the presence of an epiphyseal ring, the VEP in humans is defined differently, and is considered separate to the cortical shell [192, 214].

Studies into the dimensions for the individual human lumbar VEP structures have found the cranial VEPs (relative to the IVD) to be thicker than the caudal, with average values of $1.03\ mm$ and $0.78\ mm$ respectively, with the thickness for each increasing from L1 to L5, and is higher in samples with degeneration in the neighbouring IVD [215, 216]. Other studies into both the thoracic and lumbar region agree with these findings but consider the caudal and cranial terms with respect to the vertebra. The thinner caudal EP (with respect to the IVD) has been related to the higher fracture risk of this region, observed in clinical data [217–219]. All studies into the morphology of the endplate confirm that the endplate becomes thinner at the centre, where it is adjacent to the NP [209, 215, 217]. The porosity of the VEP has been found to be inversely related to the VEP thickness, with a greater porosity in the central region where the EP neighbours the NP, where exchange of nutrients occurs [194, 196, 220].

2.3.2.1 Collagen Organisation in EP

Collagen in the CEP has been studied using second harmonic generation (SHG) by Ferguson et al, and the images show that the collagen fibres from the non mineralised CEP are continuous going into the mineralised CEP. Such a finding would mean that the SHG signal alone is unable to distinguish between the soft tissue and mineralised interface [221]. A later study using multiphoton mi-

croscopy combined both the SHG and two photon excitation fluorescence (TPEF) signal and the mineralised cartilage had an increased TPEF signal, similar to the bone [203]. The source of fluorescence in bone is thought to be from a few amino acids in the collagen [222,223], but the fact the TPEF shows a higher intensity signal in the mineralised CEP indicates that if these are the source, then this region of the CEP has a different collagen composition, even if the structure appears the same under SHG. Other observations between the non-mineralised and mineralised CEP found that the bundles start forming subbundles at the tidemark and further into the mineralised CEP which is hypothesised to aid in anchoring the non-mineralised CEP to the mineralised CEP [203].

The collagen anchoring mechanisms at the peripheries are better understood, as the mostly type I collagen fibres at the outer AF anchor directly into the bone as Sharpey's fibres, with other components such as elastin [224, 225].

2.3.2.2 Mineralisation in VEP

The average bone mineral density assessed by μCT concludes that the mineral density is higher in cranial VEPs [215]. The BMD of the neighbouring trabecular bone to the VEP in both thoracic and lumbar studies shows the mineral density being lower in the anterior regions, and higher in the posterior arches [218]. In the cervical region of the spine, the distribution of minerals in the transverse plane exhibits a higher mineral density in the peripheral VEP, than the central VEP, and the anterior section getting increasingly more mineralised from segments C3-C7 [226]. The difference between anterior and posterior mineralisation patterns is likely due to the curvature of these difference spinal sections.

A study into how the mineral crystals vary between the bone, and the miner-

alised fibrocartilage at the AF-vertebral body interface indicates that the size of the hydroxyapatite crystals themselves do not vary between the bone, and mineralised cartilage, but there is an increase in the degree of mineralisation in the mineralised cartilage [227].

Raman spectroscopy has been carried out in the region of the endplate to look at how the biochemical composition changes between the non-mineralised CEP, mineralised CEP, VEP and vertebral body, and these were compared under the NP and the AF [83]. The ratios of mineral to matrix (carbonate and phosphate to Amide I peak respectively) were found to be higher under the NP region than the AF in all mineralised regions, with the amount decreasing from bone, to mineralised cartilage (MC) to minimal amounts in the non-mineralised cartilage (NMC) and even less in the IVD. The ratio of carbonate components in bone has previously been shown to be an indicator of the rate of remodelling in bone tissue: where a higher rate of carbonate to phosphate, or carbonate to Amide I ratio, is indicative of lower rate of remodelling since carbonate crystals are gradually substituted into the mineral matrix over time [82]. This same principle in the Raman study would indicate that the higher carbonate to amide I ratio under the NP means that there is a higher rate of remodelling under the AF [83]. This seems to contradict what has been claimed in another paper, that uses the mineral density as a marker for remodelling in human vertebral endplates, and shows that there is a higher mineral density, and hence a lower rate of remodelling, in the peripheries [226]. However, in the human study, the motion segments were from the cervical region, which has a different mechanical environment to the lumbar region. Whether this discrepancy is due to animal model limitations or due to different sections would need to be investigated further. The human study was also

conducted using a different method, computed-tomography-osteoabsorptiometry, which is assessing the density of the tissue rather than looking at spectra at the specific bonds, which might show a difference: the carbonate crystals are not the only molecules contributing to mineral matrix (6-9% in humans) as the majority of bone is hydroxyapatite, and varies between species [14].

2.3.3 Structure of Skulls and The Cranial Sutures

Skulls are the skeletal structures that house the brain, and provide protection to the brain and other facial organs. They consist of cranial plates, which are flat bones, joined together by the fibrous sutures, shown as a schematic diagram in Figure 2.8.

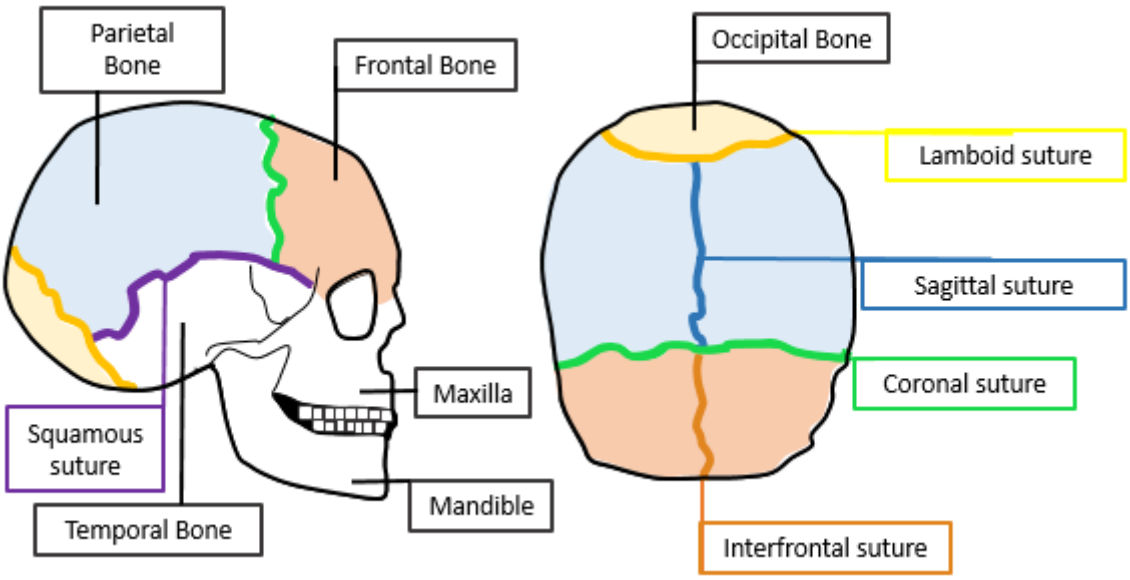

Figure 2.8: Schematic of a human skull, showing the cranial plates. The parietal bone is in a light blue, the frontal is in a light orange, and the occipital bone is a pale yellow. The sutures connecting these plates are highlighted and include the lamboid suture (yellow), squamous suture (purple), sagittal suture (blue), coronal suture (green), and interfrontal suture (orange)

Both intramembranous and endochondral ossification are responsible for the growth of the skull, with the cranial vault bones of the parietal, frontal, and part

of the occipital growing intramembranously. Endochondral ossification occurs in the temporal bone, the occipital closer to the temporal region, as well as smaller cranial base bones [228]. These methods of growth of the cranial plates are sensitive to cyclic loading [229].

The cranial plates, away from the sutures, contain two surfaces at the interior and exterior of the skull, which consist of dense cortical bone. The centre of the flat bone is made up of diploe, a type of trabecular bone found in the skull [230].

2.3.3.1 Calvarial Sutures

The sutures that connect the flat bones of the skulls are a collagenous network with mesenchyme and fibroblasts whose functional role is to facilitate the growth of the plates and to distribute stress [231–233]. Elastin is another major component within the suture ECM, contributing to the tissue's ability to withstand loads without permanent deformation [234].

The skull maintains a structurally stable curvature of the cranial plates throughout growth by continuous remodelling, where the mineralised matrix neighbouring the dura mater is absorbed by osteoclasts, and mineral deposition occurs on the external surface by osteoblasts. Upon skeletal maturity the sutures are completely ossified and no further growth of the skull occurs.

The structure of the sutures can take a few different shapes depending on the age and mechanical environment of the suture, but all of them during growth contain the unossified centre, and two osteogenic fronts at the neighbouring cranial plates. The morphology of these sutures dictates how the mechanical stresses are dissipated across the interface [235].

The different formation sutures are shown in Figure 2.9, which indicates differ-

ent forms and degrees of interdigitation, which arises throughout ageing due to externally influenced stresses on the suture [236–238]. The sutures sensitivity to changing stresses, and the responding mechanotransduction to the cells are what drive the bone growth at this interface. After exposure to higher stresses there is evidence that there is a higher level of interdigitation of the sutures [239, 240], whereas the overall width of the sutures narrows gradually during the fusion process [241].

The ages at which each suture fuses has a lot of variability [242–248], but the typical age ranges provided by literature are summarised in Table 2.1.

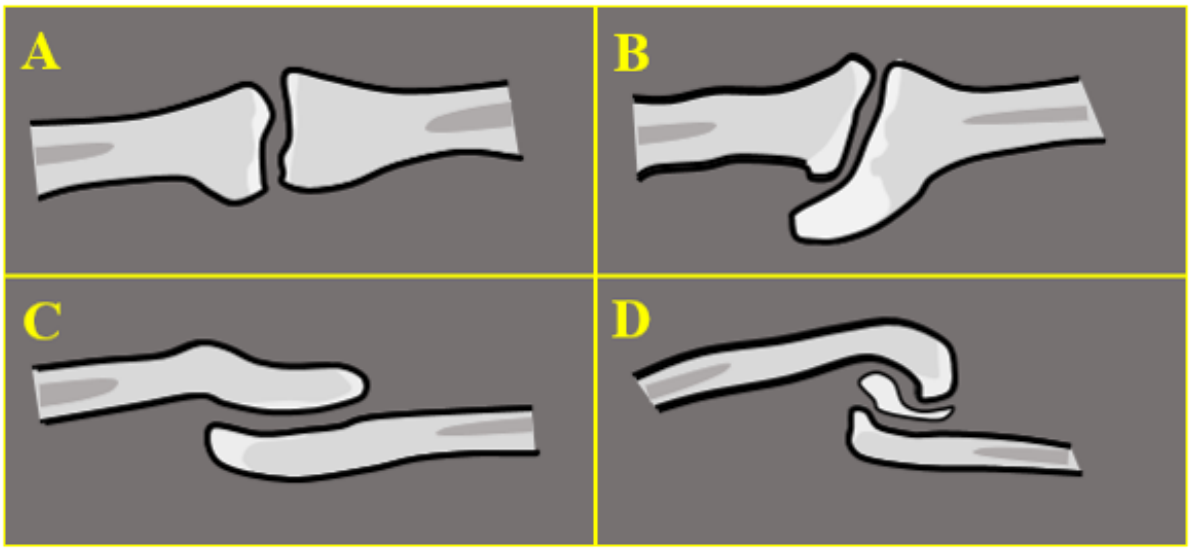

Figure 2.9: Different forms of sutures. A) An abutted suture, with no apparent interdigitation. B) Bevelled suture, with minimal overlap. C) Interdigitated pattern, and D) Highly interdigitated pattern, common in sutures with a very high stress environment. The paler grey of the bone near the sutures indicates the location of higher mineral density of woven bone, and the dark grey indicates marrow channels within the lamellar bone.

Table 2.1: Table of the Suture Fusion Ages in Humans

Suture	Typical age range for complete fusion	References
Sagittal	18-65 years	[243–245]
Squamous	>70 years	[246]
Coronal	56-70 years	[244, 245]
Interfrontal	3 - 9 months	[247, 248]

2.3.3.2 Collagen in Calvarial Sutures and Cranial Plates

The collagen in the cranial plates is predominantly type I, and like other bones, the majority is lamellar and parallel to the surface of the bone. Within the suture, the fibrous tissue contains mostly type I collagen arranged in such way that at the borders of the soft tissue the fibre alignments are almost parallel, whereas in the centre of the suture there is no dominant direction, and is shown as a diagram in Figure 2.10 [249–251]. The collagen type expressed in the suture is susceptible to the mechanical environment, as when the sutures undergo mechanical stress, the cells produce type III collagen rapidly as a response [252].

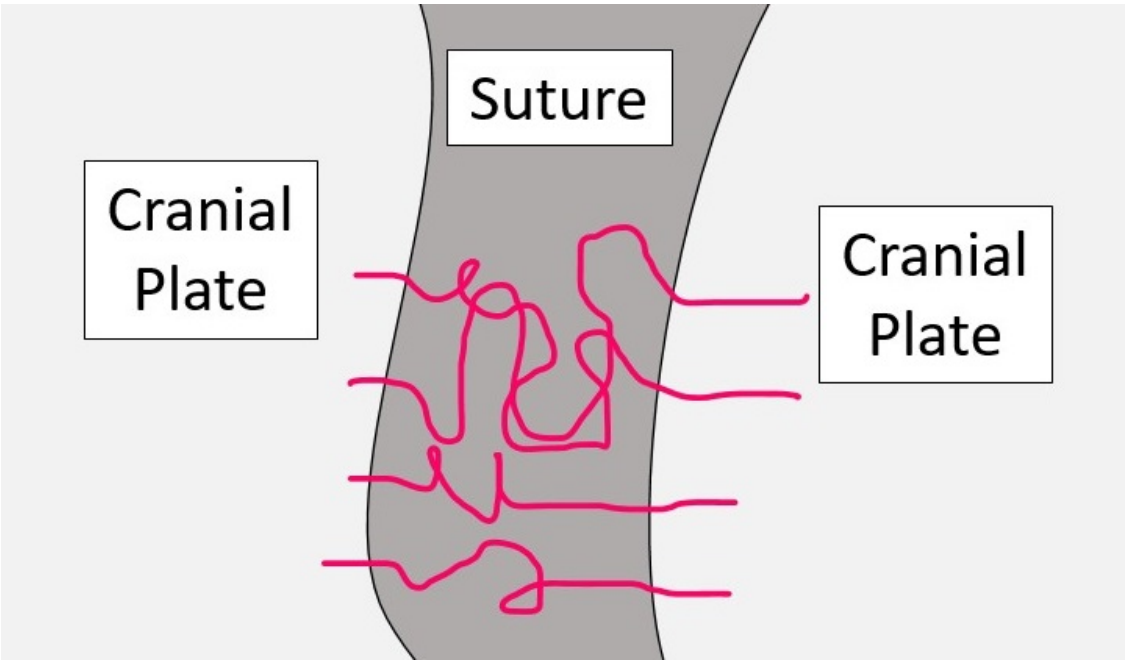

Figure 2.10: Schematic of collagen arrangements in the cranial sutures. The two cranial plates are shown at the sides, with the suture in dark grey in the centre. The collagen is shown by the pink lines, where the fibres in the suture have a disordered spatial arrangement. These pink lines represent all collagens, including type I and III in this circumstance.

2.3.3.3 Minerals in the Cranium

The bone mineral density of the skull vault has been evaluated to be $2.19 - 2.3$ g/cm^2 in premenopausal women [86, 253], and with other studies showing the BMD of the skull depending on age and sex of the sample [254]. These studies have looked at the entire region of the cranial vault, and so do not provide the smaller level detail needed to understand the mineral heterogeneity on the micrometre scale.

Work on characterising the minerals on the nanoscale at the suture-cranial plate interface has focused on the biochemistry of the crystals, and how that changes through fetal development [85, 255]. These have verified that the mineralisation process described in section 2.2.2, where the apatite crystals grow once within the collagen structures, occurs at this interface also, and that there

are variations of apatite minerals present, detected by Raman spectroscopy [85].

2.3.3.4 Mechanical Properties

Due to animal models being required for early research [256], a schematic of a mouse skull is shown in Figure 2.11 which visibly has a different morphology to the human skull depicted in Figure 2.8, but the sutures and cranial bone organisation is comparable. The mechanical properties of the frontal and parietal plates have been compared as well as the unmineralised suture, and it has been found that the frontal is mechanically stronger, but that the parietal has a ductility. The sagittal and coronal sutures display no major differences [257]. When comparing these mechanical values to the diseased state, the frontal bone in mice mutated to have craniosynostosis has a lower elastic modulus than the wild type, but the parietal bone did not show this difference, and there was no difference between the elastic moduli of the sutures themselves [258].

The facial sutures and their mineralisation fronts have been investigated by nano-indentation, and has shown that there are differences between the elastic modulus of the sutures themselves, as well as the bone neighbouring them [259]. This indicates that each suture will have a different composition and structure, related to the mechanical environment which it experiences.

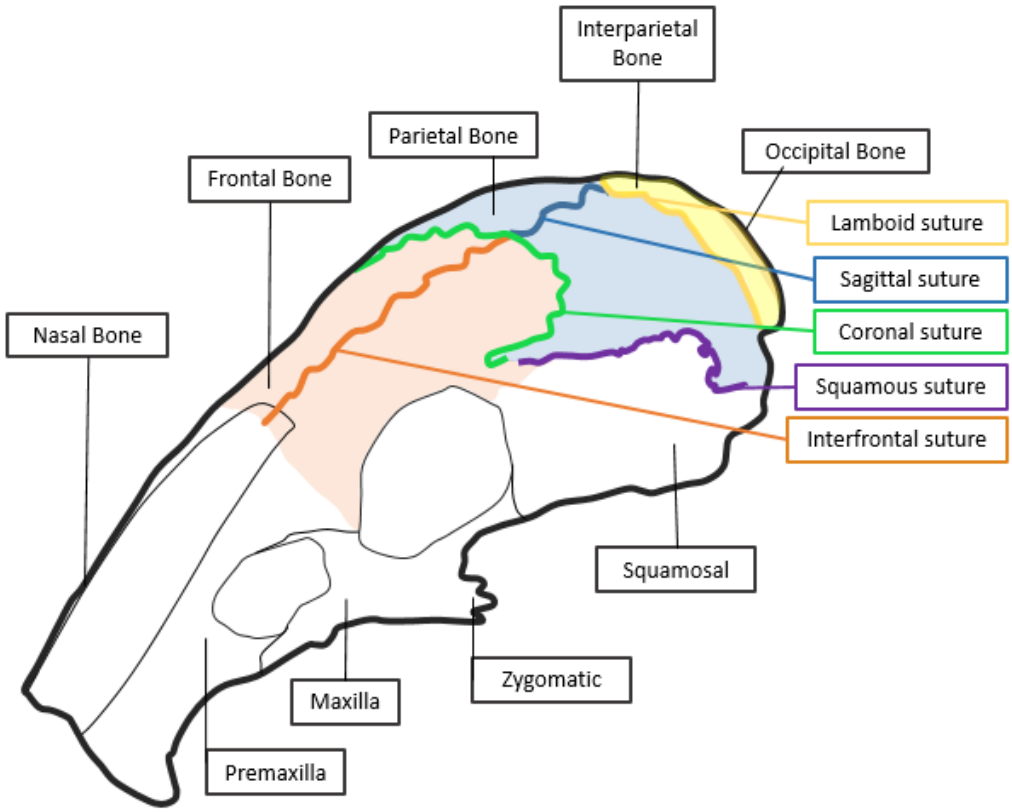

Figure 2.11: Schematic of the sutures of interest and the relevant cranial plates for a mouse skull. The sutures are in thick coloured lines, and the plates are a pale colour.

2.4 Dysregulation of Biointerfaces

2.4.1 Clinical Relevance of Endplate changes

One of the most common disabilities in the UK is chronic back pain, and a common physical symptom is that of degenerated IVDs [1, 260, 261]. Since the nutrition of the IVD comes from the endplates, the hypermineralisation of these endplates later in life has been associated with the degeneration of the IVD, leading to altered mechanical function of the tissues [8, 11, 199, 214, 262]. The degenerated disc is characterised by a breakdown of the NP-AF boundary, excessive bulging, reduction in IVD height, and ingrowth of vasculature and nerves into the normally avascular and aneural tissue. Meanwhile the neighbouring bone has

been observed to have the formation of osteophytes at the peripheries, and more centrally, there is the presence of Schmorl's nodes, where the IVD tissue, most commonly the NP, penetrates through the EP into the vertebral body [263].

These pathologies occur commonly with ageing, and how the healthy tissue compares to this degenerated state is shown in Figure 2.12.

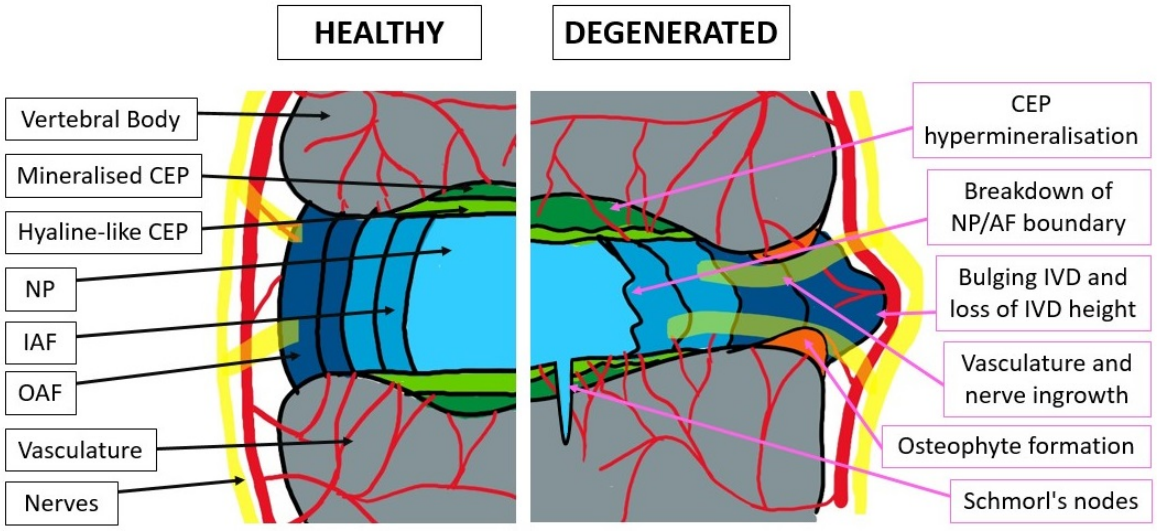

Figure 2.12: A diagram comparing a healthy spine to one with a degenerated IVD. The main changes in the degenerated state are hypermineralisation of the CEP, bulging of the IVD and loss of IVD height, protrusion of vasculature and nerve vessels into the IVD, and in the bone there is the formation of osteophytes.

2.4.2 Disease associated with mineralisation of calvarial sutures

Premature mineralisation and closure of the sutures leads to deformities that can increase intracranial pressures, in a disease known as craniosynostosis [66]. Craniosynostosis effects 1 in 2000 newborns and has symptoms of visual damage, disrupted mental development, and occasionally death [264,265]. There are characteristic skull deformations that arise from craniosynostosis, where the differences arise from which sutures fuse prematurely in comparison to the others. Most commonly it is the sagittal suture which fuses early, resulting in scaphocephaly [66]. The causes of craniosynostosis are thought to be primarily genetic,

with over 50 gene mutations so far which are responsible for the premature fusion of the sutures [266]. With current therapies for this disease involving breaking and reshaping the skull of infants [13, 267], it is of interest to understand the mineralisation process at this interface and how less invasive methods of treatment could be achieved.

Chapter 3

Imaging Techniques

This chapter introduces the microscopy techniques which were used to image the tissues described in chapter 2. The systems used consist of a confocal laser scanning microscope (CLSM), a multiphoton microscope (MPM), and a scanning electron microscope (SEM), to image the OLCN, the collagen, and the minerals respectively. The details include the physical set up of how the microscopes achieve high resolutions, and how the signal is produced in the tissue to give the spatial information on the feature being imaged.

3.1 Confocal Laser Scanning Microscopy

A confocal system is one which uses a pinhole to filter out out-of-focus light. The principles of a confocal microscope are shown in Figure 3.1, where the beam path of the light emitted by the sample is manipulated to get a strong signal from the focal plane of the objective lens, and a confocal pinhole is used to filter out the signal that originates from other planes, producing an image that isn't degraded by light originating from out-of-focus planes in the sample. A conventional confocal microscope includes a series of lenses, to focus the laser, and a dichroic mirror

with different reflective and transmission properties depending on the wavelength, to ensure the initial laser beam (green in Figure 3.1) is reflected and focused by the objective lens towards the sample (yellow in Figure 3.1). The emitted fluorescence from within the sample, with a different wavelength (red in Figure 3.1), is captured and collimated by the objective lens, and transmitted through the dichroic mirror. It is then focused with a lens through the pinhole aperture, which filters out the signals generated from other planes within the sample, to create a high-resolution image [268, 269].

The wavelength of the laser is chosen along with a dye to show up features of interest with a high quality. In this thesis, the dye is Rhodamine 6G, with an excitation wavelength of $525\ nm$, and an emission wavelength of $548\ nm$ [270].

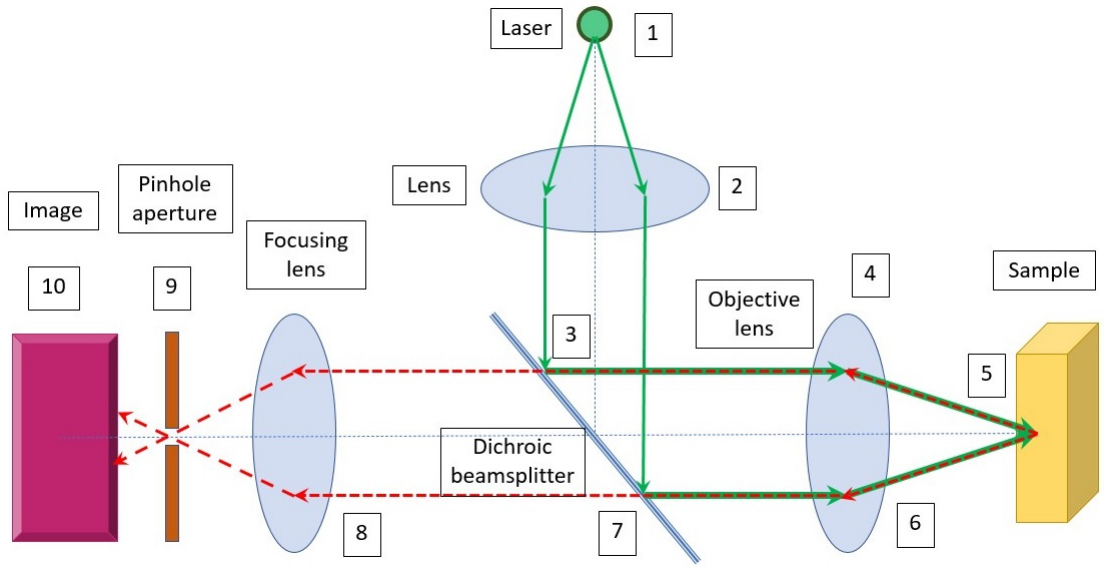

Figure 3.1: Basic principles of confocal microscopy, where a laser beam (1) is collimated by the lens (2) to a dichroic mirror (3). At this mirror, most of the light from the direction is then reflected towards another lens (4) where it is focused onto the sample (5). The light emitted by the sample (now red arrows), is then collimated by the objective lens (6), passed through the dichroic mirror (7) and focused by another lens (8) to get the signal through the pinhole (9) to create the image (10).

A CLSM was used in the osteocyte canalicular network part of this project, where a laser of $488\ nm$ was used. 3D image stacks were acquired in addition to large area images, which were acquired by tiling multiple fields of view.

3.2 Multiphoton Microscopy: Second Harmonic Generation

MPM involves the use of a long wavelength, high intensity lasers to image various features within a sample by the near simultaneous absorption of two or more photons, which are then emitted as one higher energy photon. Frequency doubling is the phenomenon where two photons of frequency f, get absorbed, to produce one photon with a frequency of $2f$, and is also known as second harmonic generation (SHG). SHG is used to image chiral structures, such as collagen. Chiral structures have no centre of symmetry, and so the second term of the non-linear polarisation polynomial ($\chi^{(2)}$ in equation 3.1) does not tend to zero, leading to a comparatively strong second harmonic signal with respect to other mediums. In samples with inversion symmetry, the second term tends to 0 due to the electric dipole approximation [268, 271].

$$\mathbf{P}(E) = \epsilon_0\big(\chi^{(1)}\mathbf{E} + \chi^{(2)}\mathbf{E}^2 + \chi^{(3)}\mathbf{E}^3 + ...\big) \tag{3.1}$$

In equation 3.1 the polarization is the vector $\mathbf{P}(E)$, ϵ_0 is the permittivity, χ is the susceptibilty of the medium and **E** is the electric field vector of the incoming field [272].

The principles of Second harmonic generation are shown in Figure 3.2, where the resultant photon is exactly twice the energy of a single incoming photon.

On the molecular level, fibrillar collagen forms an ordered and non-centrosymmetric material which makes it an efficient generator of the second harmonic signal near infrared light. As a result, SHG microscopy has become the gold standard for studying the microscopic orientation and organisation of fibrillar collagen.

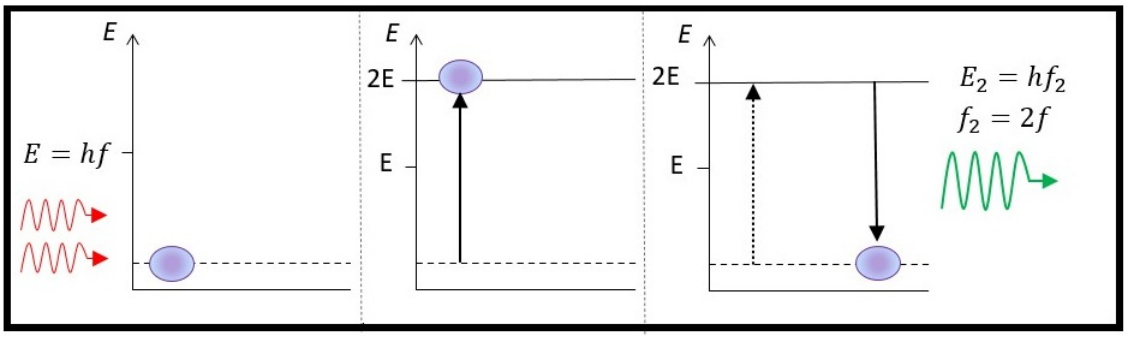

Figure 3.2: The energy diagrams showing the process of a purely elastic multiphoton emission process, where two lower energy photons (red) are absorbed near simultaneously and emitted as one higher energy photon (green), with no energy lost.

3.2.1 Polarisation Dependent SHG

The SHG signal intensity is dependent on the polarisation of the incoming laser, and the orientation of the structure producing the SHG signal. A polarisation sensitive SHG (pSHG) data set consists of a series of SHG microscopy images acquired from the same field of view, with each image being acquired with a different incident polarisation. The maximum intensity will be when the 3D structure of the collagen fibrils is aligned with the incoming laser polarisation. A schematic of this can be seen in Figure 3.3a, where the incoming laser has a polarisation angle of α, and when the collagen bundle also has a principle direction of α, the SHG signal is brighter. As the angles change to become less aligned with the incoming laser, the intensity reduces, depicted by the darker yellow collagen bundles in Figure 3.3.

For each pixel, when scanning through the angles, the intensity can be plotted to a cosine fitting function to show this polarisation dependence, and the maximum intensity is indicative of the principle collagen orientation. The degree to which the SHG intensity is modulated by the rotation of polarised light is a measure of the dispersion of the collagen molecules. If all collagen fibres and bundles

are aligned, as seen in Figure 3.3b in red, then the SHG intensity detected from the sample will be strongly modulated by the effect of the polarisation rotation. However, regions that have collagen fibrils with a greater degree of dispersion, such as in Figure 3.3b in green and blue, the SHG signal will be originating from structures with a variety of directions, and therefore the amplitude of peaks and troughs in the SHG intensity will be reduced. With these measurements, it is therefore possible to directly measure the orientation at the fibrillar level, and probe the organisation at the molecular level [273–275].

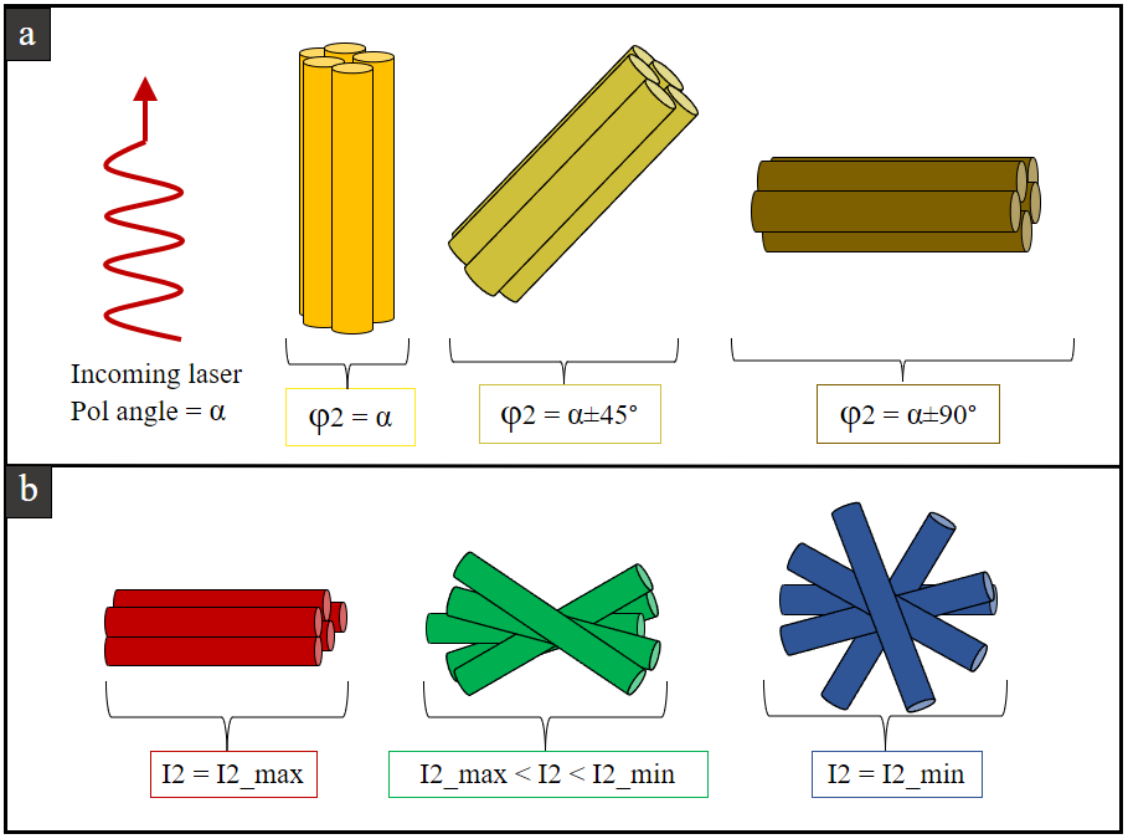

Figure 3.3: The schematics of how the collagen structures effect the SHG signal at different polarisation angles. a) The principle direction of the collagen bundle determines the intensity at a given polarisation, with a brighter signal when the polarisation angle matches the orientation. b) The degree of dispersion of the collagen is responsible for how much the intensity changes with polarisation angle, and must be within the region of I2=1, where all bundles are perfectly aligned, seen in red in this schematic, down to I2=0, shown in dark blue, where all bundles have a maximum degree of dispersion and are not aligned.

The circular functions used to parametise the modulation of SHG intensity at

each image pixel as a function of the incident polarisation angle are shown in equations 3.2 and 3.3, where $I_{SHG(\alpha)}$ is the overall intensity of the SHG signal at a polarisation angle α. I_2 and ϕ_2 are the second order parameters for intensity and phase respectively, and I_4 and ϕ_4 are the fourth order counterparts. [17,274–277]. The coefficients are a_0, a_2, a_4, b_2 and b_4 and are calculated by projecting the measured data onto the circular functions defined in equation 3.2 [277]. For this thesis, it is the second order parameters of intensity (I_2) and phase (ϕ_2) which are obtained by the coefficients, shown in equation 3.4.

$$I_{SHG(\alpha)} \propto a_0 + a_2 cos2\alpha + b2 sin2\alpha + a_4 cos4\alpha + b_4 sin4\alpha \tag{3.2}$$

$$I_{SHG(\alpha)} \propto a_0 + I_2 cos2(\alpha - \phi_2) + I_4 cos4(\alpha - \phi_4) \tag{3.3}$$

$$I_2 = \frac{\sqrt{a_2^2 + b_2^2}}{a_0}, \phi_2 = \frac{1}{2} tan^{-1}\Big(\frac{b_2}{a_2}\Big) \tag{3.4}$$

Since I_2 values depend on how much the intensity changes throughout the stack, the value depends on the dispersion of the collagen fibrils, as seen in Figure 3.3. If the collagen fibrils are perfectly aligned, then the signal will experience a greater change in intensity as the polarisation angle changes, and there will be a greater value for I_2. However, if the the collagen is dispersed, there will be minimal changes in intensity (low I_2) as for each pixel there will always be a small amount of collagen generating the signal for each angle. With this theory, the pSHG quantitative process is shown in Figure 3.4, where Figure 3.4a shows the raw image stack taken with multiple polarisation angles. Figure 3.4b shows the plotting of one pixel with varying intensity, and the fitting curve to obtain the

coefficients. The results for the values of I_2 are expressed in two ways, one with a histogram to show the entire spread of values, and one with a colour map to show where these values come from within the raw image, both shown in Figure 3.4c. The range of $\Phi 2$ values are visualised within a polar plot in Figure 3.4d to show the 90° range of bundle directions within the sample, and how certain directions are more prominent. The final data is shown in Figure 3.4e, where small areas of I_2 and $\Phi 2$ data are averaged, and a line is plotted with the angle of the average $\Phi 2$ for that smaller area, and in the colour of the average I_2, so that we can see the spatial distribution of the I_2 and $\Phi 2$ values on the sample imaged.

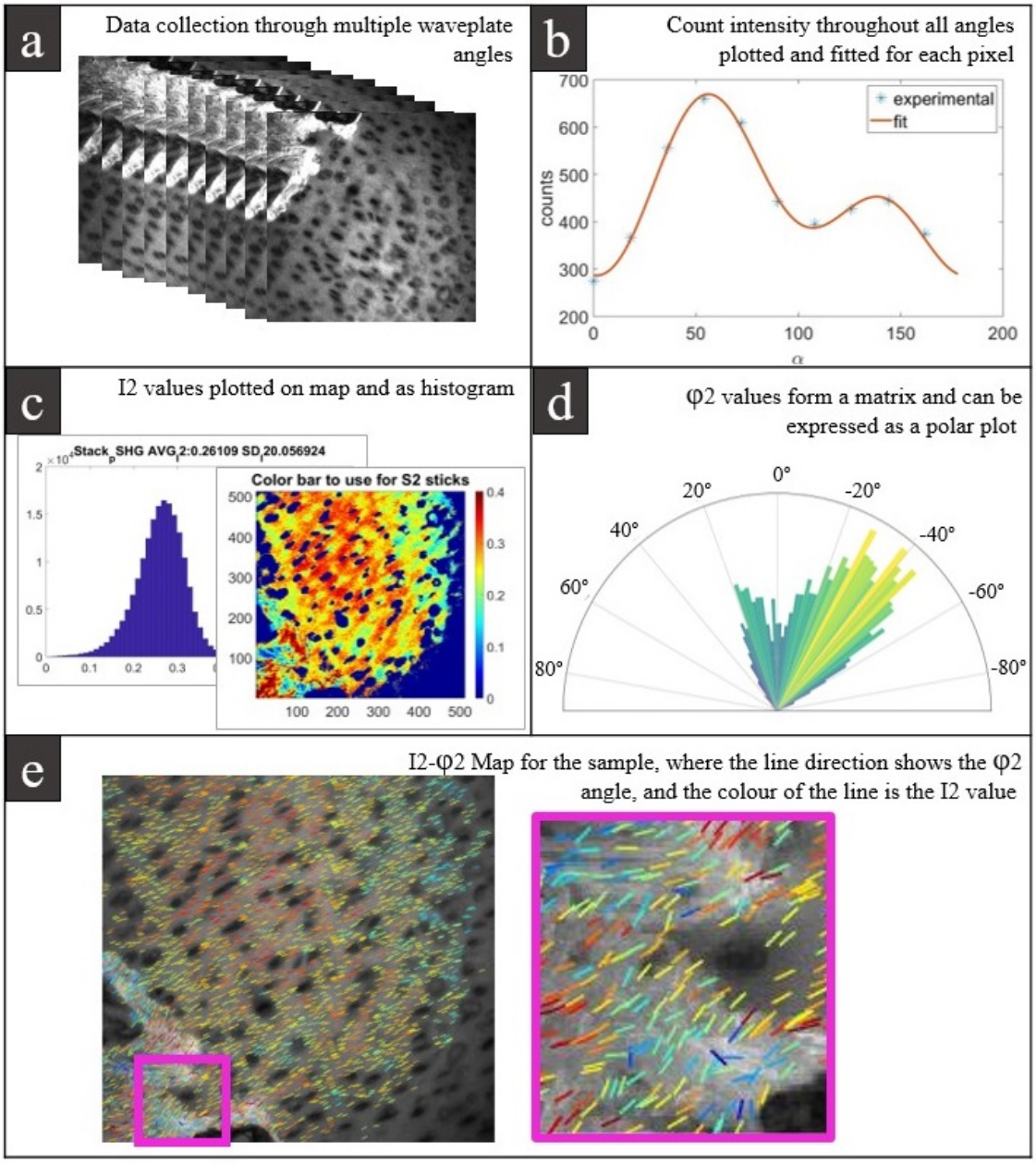

Figure 3.4: An example of the steps of pSHG quantitative analysis on articular cartilage at the cartilage and subchondral bone interface. a) The raw data is collected as a stack of the same location with different polarisation angles for each slice. b) Each pixel count is plotted as a function of polarisation angle, and fitted with a cosine function. In c) the results of I2 are shown, as both a histogram, as well as a colour map. d) The polar plot of $\Phi 2$ values, and in e) the final I2-$\Phi 2$ map overlayed with the averaged raw data to show the spatial distribution of the values, where the lines direction represents the principle orientation ($\Phi 2$), and the colour of these lines is indicative of the dispersion (I_2 value).

3.3 Multiphoton Microscopy: Two-Photon Excitation Fluorescence

MPMs are also routinely used to acquire images of two-photon excited fluorescence (TPEF), a nonlinear optical process that occurs when two co-incident photons combine to promote an electron to a higher energy state. In fluorescent molecules, some of the excitation energy is lost to thermal relaxation processes before emitting a fluorescent photon in order to return to its electronic ground state. A TPEF signal is produced by the same experimental set up that is used to excite SHG, and so both of these are acquired simultaneously by two separate detectors. The principles behind TPEF are shown in Figure 3.5, where the difference between TPEF and SHG can be visually seen by the thermal relaxation occurring in Figure 3.5, yet not in the SHG process shown in Figure 3.2.

Due to the lower energy emissions of TPEF compared the SHG, the detectors can filter the signals by their wavelength, with a bandpass filter with a narrow range at $2f$ required for the SHG channel, and a wide bandpass filter for $< 2f$ for the TPEF.

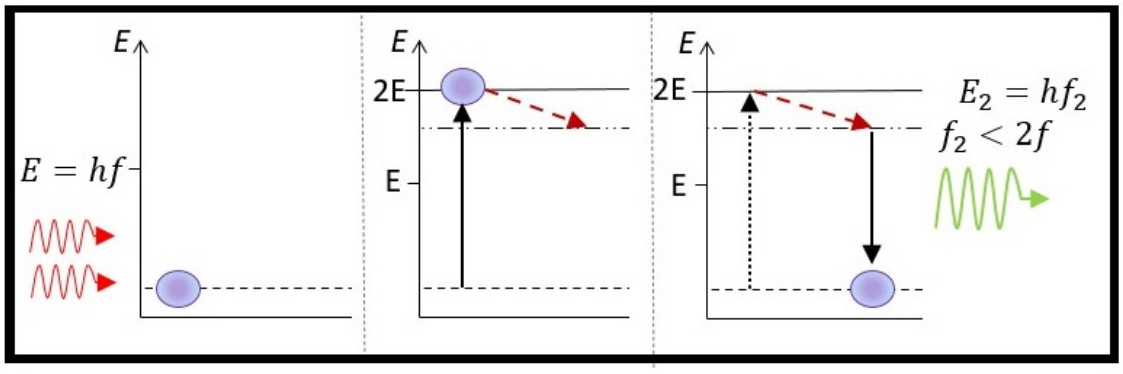

Figure 3.5: The energy diagrams of the multiphoton emission process, where two lower energy photons (red) are absorbed simultaneously, and emitted as one (green), but there is energy lost during thermal relaxation (vibrational energy in dark red dashed line).

3.4 Scanning Electron Microscopy

Electron microscopy can be used as a microscopy technique to image features smaller than the wavelength of light, and also to obtain the elemental composition at the surface. The principles of the electron microscope are shown in Figure 3.6, where an electron source produces a stream of electrons, which are then collimated and focused by a series of charged and magnetic lenses. This beam then scans across a sample, and there are a variety of interactions with the sample that produce unique signals that can be detected, seen in Figure 3.7. The signals from the secondary electron interaction, and the backscattered are explained in more detail, as those are used in the experiments in later chapters.

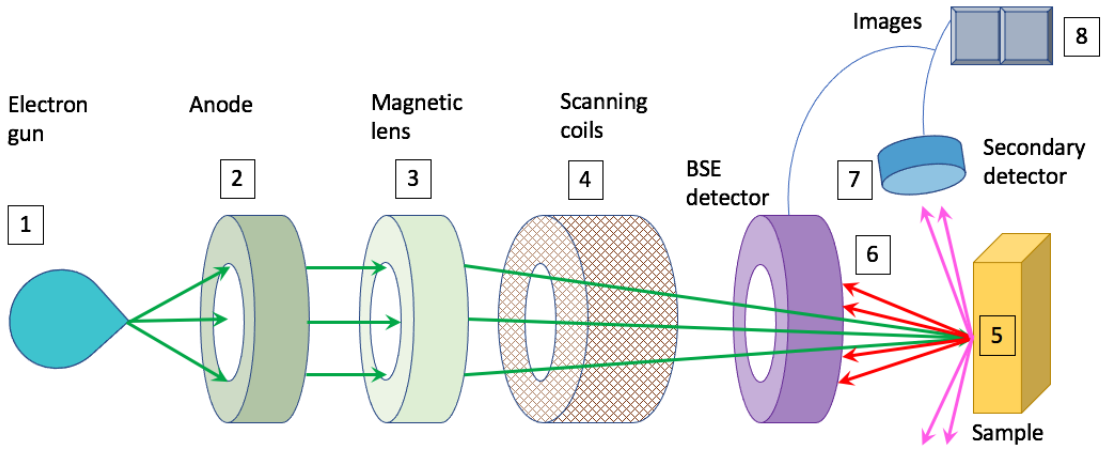

Figure 3.6: A schematic of the electron microscope set up. An electron gun emits a source of electrons (1) that are then collimated by an anode (2). The beam of electrons is focused with a magnetic lens (3), and the scanning coils allow for the raster movement of the beam (4) on the sample surface (5). The 2 main signals are back scattered electrons (6), and secondary electrons (7), which provide different information, and therefore two images (8)

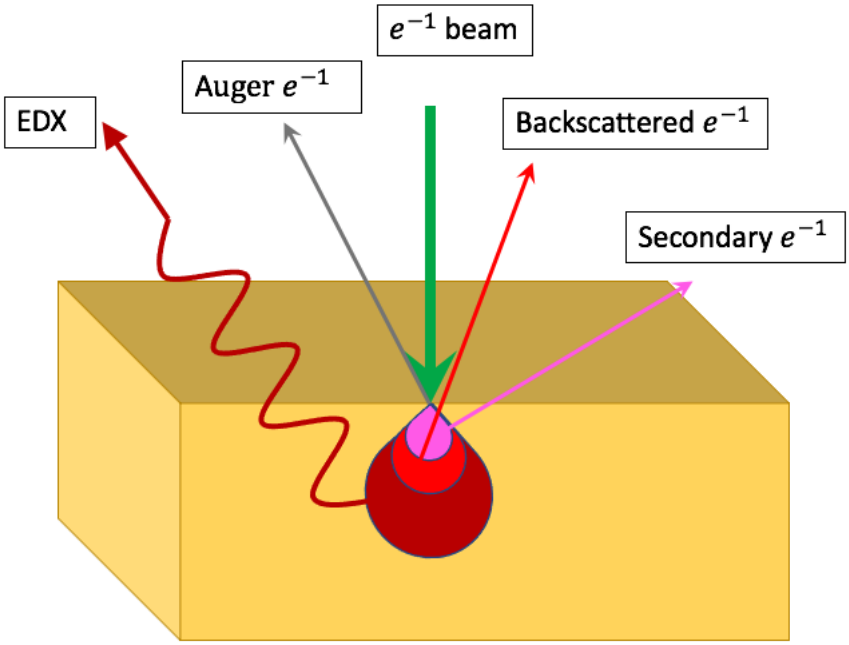

Figure 3.7: Location of where the electron signal comes from when scanning with the electron microscope. Secondary electrons are emitted by the incoming beam exciting the electrons in the atoms. Backscattered electrons are the elastic scattering of the initial electron beam EDX is the detected X-ray photon released from deeper within the sample, where the source is an electron filling a vacant shell from a previous emitted electron. Auger electrons (grey) are very rare, and can only be detected from the very surface as a by-product of secondary emission leaving a vacant shell, and the energy of orbital filling being transferred to another electron which is enough to eject it from the atom.

3.4.1 Secondary Emissions

Secondary electrons (pink in Figures 3.6 and 3.7) are emitted from the first few nm of the sample and so produce an image of the topography of the sample. The energy range is typically $< 50\ eV$, lower than the incoming beam due to inelastic processes. They are sourced from the ionisation of the atoms at the surface, where the excitation process causes the ejection of an electron. The production of secondary electrons at the atomic scale is visualised by the Bohr models in Figure 3.8.

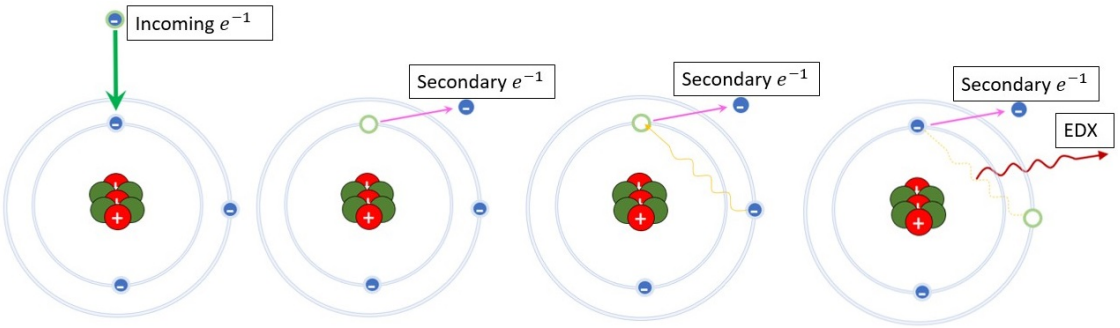

Figure 3.8: The process in a Scanning Electron Microscope of how the secondary electrons are produced, as well as the EDX signal. The secondary electrons are electrons already part of the sample atoms, that are displaced due to the incoming electron beam. The EDX signal is a characteristic photon emitted when the orbital vacated by a secondary electron is filled.

3.4.2 Back Scattered Electrons

Back-scattered electron (BSE) imaging is the signal from the electrons that are elastically reflected back from the material. Since the process is elastic, the energy of the backscattered electrons is higher than the secondary electrons, and the electrons are the same ones from the original beam. The typical energies are similar to that of the initial incoming electron beam, and it is a combination of both the different energies, and the different detection angle that distinguishes BSE and Secondary electron signals. The images produced with BSE contain information from deeper within the sample than secondary electrons, and the pixel brightness is determined by the atomic number of the sample. Elements with a more positively charged nucleus are able to back scatter a greater proportion of the incoming electrons, leading to a stronger signal, and are therefore seen as a brighter pixel. This scattering process is shown in Figure 3.9 on the atomic scale.

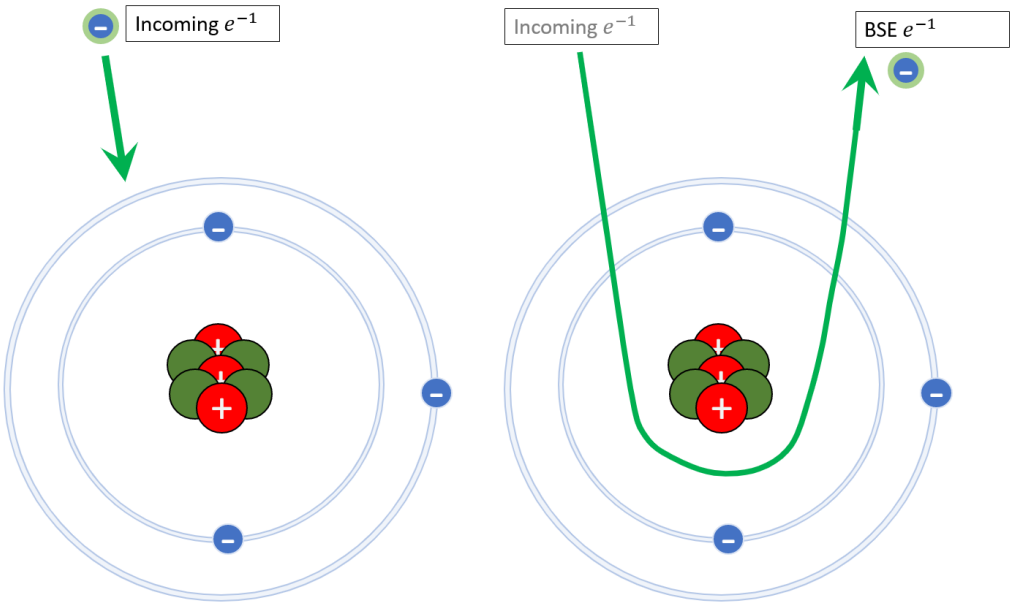

Figure 3.9: The process of backscattered electrons, where the electron is the same as the incoming electron, but has been elastically diverted from the originally beam path, due to the strong positive charge of the nucleus.

3.4.2.1 Quantitative Backscattered Electron Imaging

Quantification of the degree of mineralisation in a tissue was obtained using Quantitative Backscattered Electron Imaging (QBEI). This process used the theory of how signals are produced in a BSE image, alongside reference materials to quantify the mean atomic number (Z_{mean}) of the tissue, as well as the calcium weight % (CaWt%). The proportion of backscattered electrons, and hence the intensity of the signal, is linearly dependent on the mean atomic number of the elements being scanned. On the image produced this was displayed as a brighter intensity on the pixel where there were heavier elements. Due to this linear relationship between the pixel intensity and mean atomic number, the mean atomic number of a variable sample was calculated with the use of known reference materials imaged under the same conditions. In this project, the reference materials used were Carbon (C), Magnesium Fluoride (MgF_2), and Aluminium (Al), which

were used to create a linear plot with the following format:

$$Intensity = mZ_{mean} + C \tag{3.5}$$

This equation was then used to extract the Z_{mean} value from the raw image with unknown Z_{mean}, where m was the gradient, and C was the y-intercept.

In mineralised tissues the majority of the BSE signal comes from the calcium in the hydroxyapatite crystal. The variations in intensity, and therefore Z_{mean}, in the tissues further allowed us to calculate the CaWt% in the tissue. The known CaWt% of pure hydroxyapatite is 39.68%, with a Z_{mean} of 14.06. The CaWt% of osteoid, or unmineralised tissue is 0%. With the Z_{mean} of hydroxyapatite known, the theoretical pixel intensity was obtained by the first linear relationship (equation 3.5). A second linear equation was then obtained, relating the pixel intensity, to CaWt%, using the theoretically calculated hydroxyapatite value for pixel intensity under those conditions, and the osteoid tissue imaged in the sample. The format of the new equation was:

$$CaWt\% = m_2 Intensity + C_2 \tag{3.6}$$

This second equation can then be applied across all pixels to convert the intensity into a CaWt%, where m_2 is the gradient, and C_2 is the y-axis intercept.

3.4.3 Energy Dispersive X-ray Spectroscopy

Energy Dispersive X-ray Spectroscopy (EDX) relies on the process of secondary electron emission, as this means that higher energy electrons drop down to a lower, vacated state, and emit a photon with a specific energy. Since every ele-

ment has a unique emission spectra, the elemental composition can be acquired from detection of these photons, as well as the relative amount as a percentage. This process is shown in Figure 3.8, where relaxation of an electron in an higher energy orbital, releases this characteristic photon.

Chapter 4

Multimodal Study of the Endplate

4.1 Introduction

The endplate (EP) is the multi-layered tissue which connects the cartilaginous growth plate of the vertebral body to the intervertebral disc (IVD). The layer of EP neighbouring the IVD is a layer of hyaline-like cartilage, referred to as the non-mineralised cartilage endplate (CEP). Adjacent to the non-mineralised CEP is a layer of mineralised cartilage, which is known as the mineralised CEP. Between the CEP and the cartilaginous growth plate lies the vertebral endplate (VEP). The VEP, sometimes referred to as the boney endplate, or the osseous endplate, is where literature is inconsistent with terminology [188, 203, 209, 215, 278]. The combination of these three layers of non-mineralised CEP, mineralised CEP, and VEP, collectively make the whole EP structure, as is seen in Wojtków et al. [209].

This three layered structure is important for flexibility, withstanding heavy loads, and transporting nutrients. With degeneration of the tissue these functions are impaired, and changes in this structure leads to back pain and further degeneration in both the soft IVD, and an increased risk of fracture in the boney tis-

sue [201, 279–281]. The complex organisation of the VEP imposes a significant challenge in studying its structure-mechanics relationship and the changes in ageing or pathological conditions. However, understanding the structure and mechanics of this region is critical to both the preventative and therapeutic clinical methodologies, due to the increased risk of fracture that occurs at this boundary [217, 279, 282, 283].

The constituents of the EP which give rise to its mechanical properties are the minerals and collagens, and the organisation within each layer is vital for the functionality. The non-mineralised CEP does not have minerals for rigidity, but the hyaline-like collagen structure helps to distribute the loads across the IVD so compression and flexion can be achieved without pain or damage [9, 187, 284]. The mineralised CEP contains collagen fibres which are continuous bundles from the non-mineralised CEP, but are also encrusted with the mineral pellets which gives it rigidity [203, 221]. The VEP contains type I collagen, with large bundles of collagen being parallel to the VEP-CEP interface in the central region [285]. At the peripheries of the VEP, the collagen fibres changes direction to create Sharpey fibres which join the collagen bundles in the outer annulus fibrosus (OAF) of the IVD [224]. The continuous collagen between the two regions of the CEP are what keep these two mechanically different tissues connected, and the minerals serve as an anchor between the CEP and the VEP. The VEP is the result of secondary ossification centres in the vertebral body, and therefore has a role in growth, as well as being highly vascularised and porous so that there is a supply of nutrients to the cartilaginous tissues [209, 214, 262, 284, 286, 287].

In order to enable material exchange across this three-layered structure and reach the avascular IVD, there is a multiscale transport system to bring in nutri-

ents and remove metabolic wastes [196, 288]. The boney VEP has vasculature and has the osteocyte lacunae canalicular network (OLCN) as a transport network between the blood vessels and the osteocytes to keep the cells viable in the boney tissue [146, 150]. Despite the dense mineral matrix, the mineralised CEP is still porous, so that the neighbouring soft tissue can receive nutrients and dispose of waste [196, 288]. However, the nature of molecule transport across the multiphase CEP is still to be determined. The porosity of the mineralised CEP has been reported to be higher in the central regions adjacent to the nucleus pulposus, with channels permeating through the mineralised tissue and terminating as buds at the tide mark. Some researchers have hypothesised that these channels may contain either blood vessel loops or lymphatic vessels [203, 287, 289–291]. These channels are assumed to be the route of large molecules to flow between the bone and IVD [198], and the reduction of these channels has been correlated with a greater degree of degeneration [198]. For small molecules, diffusion through the tissue suffices as the main transport mechanism in healthy samples [193, 196, 288]. However, as mineralisation of the CEP increases, the overall diffusivity of the CEP decreases, and this change in transport property also negatively affects the cells in the IVD [188, 288]. With these nutrition and waste pathways becoming obfuscated, there is a greater role in dynamic loading later in life to ensure the IVD remains healthy [184, 193].

Much of the research on the spine has focused on characterising the IVD and how that changes with age. The changes experienced by the soft tissue can be captured by techniques, such as magnetic resonance imaging (MRI), to show the breakdown of boundary between the nucleus pulposus and the annulus fibrosus, and bulging of the IVD [186, 190, 292–294]. However the effects of degeneration

on the neighbouring boney tissue is sparse, with conflicting data, such as where channels terminate prior to the disc, and how the permeability of the mineral matrix changes with age [191, 193, 203, 290, 295].

The VEP is a point of interest due to the complex mechanical environment, and high risk of failure in older patients [217, 279, 282, 296–298]. The mineralised CEP has been explored by backscaterred electron imaging (BSE) to compare the mineralisation interface in both healthy and aged or diseased samples [221], but have yet to be characterised by both the mineralisation and cellular network, both which are indicators of bone health [69, 299–302]. The connection between these mechanically different tissues has gained attention more recently. Whilst the collagen structure between the non-mineralised CEP and mineralised CEP has been investigated by second harmonic generation (SHG) to show continuity across the tidemark [203, 221], the collagen structure between the mineralised CEP and VEP and the spatial correlation between the collagen, minerals, and cellular organisation are still to be explored. Observations on osteochondral interfaces found elsewhere in the body, such as articular cartilage on joints, have the collagen bundles anchor directly into the subchondral bone [16, 126, 303, 304]. However, the VEP and CEP interface does not have a near-perpendicular insertion of fibres across the interface [284, 285], which could be a prominent factor in the high fracture risk in this region. The spatial correlation between the mineralisation and the osteocyte lacunae canalicular network and collagen is where there is a significant gap in knowledge, but would provide insight into how these factors may influence each other in such a mechanically dynamic tissue interface.

Recent work in long bones has used multiple imaging modalities in order to characterise features such as the OLCN and mineral density distribution using

confocal laser scanning microscopy (CLSM) and scanning electron microscopy (SEM) respectively [69, 299, 300]. These features can be an indicator of the bone's ability to respond to changing environment, and can therefore provide insight into how the VEP changes with age, and correlates to the degree of degeneration more commonly seen in the IVD. The same samples can be imaged using SHG and two photon excitation fluorescence (TPEF) to obtain information on the collagen structure to assess the organisation of the collagen in these tissues [17, 87, 126, 268, 303, 305]. The collagen organisation across boundaries is where stresses are dissipated and detailed studies into the collagen orientation and dispersion can therefore provide insight on why there is an increased fracture risk at these boundaries.

In this chapter, the focus is on the VEP, the boney structure spanning between the CEP and the growth plate. This chapter focuses on characterising the structure of the EP in young, healthy animal models, by assessing the mineral distribution and OLCN in the tissues, and illustrating how the VEP is connected to CEP. The aims are to answer the following research questions:

- How does the arrangement of the OLCN, and more specifically the canalicular density compare between the irregular bones of the vertebral bodies in sheep models, and the already established long bones in multiple animal models?
- Is the mineral distribution in the VEP homogenous, or heterogenous, and if the latter, what is the spatial pattern?
- Where within the EP structure does the collagen change from predominantly type II to type I, and how does the dispersion of these collagen fibres change between the mechanically dissimilar tissues?

The EP is studied by three imaging techniques in this chapter, each giving complementary data to help build up a more comprehensive picture of the structures making up this interface. CLSM in combination with rhodamine staining is applied to investigate the OLCN distribution in the VEP. The BSE data focuses on the distribution of minerals and uses Energy dispersive x-ray spectroscopy (EDX) data to assess the ratios among elemental compositions. The polarisation-resolved SHG (pSHG) is used to obtain maps of the collagen orientation in the VEP, and further information on the structural gradient of collagen organisation between the VEP and CEP.

4.2 Methods

4.2.1 Sample Preparation

Due to lack of accessibility of human spine for research animal models are an important substitute to ensure consistent results. Ovine spine has been commonly used to study the spine [190, 306–309], and it is adopted in the following experiments. To be noted, the main difference between ovine and human spine is that sheep have a clearly identifiable VEP, with the growth plate separate from the other cartilaginous tissue. In human, the growth plate is part of the EP structure and there is an epiphyseal ring, as described in chapter 2.

The sheep spines were collected from nearby farms, and frozen upon collection. Three were from sheep less than a year old, as they were the by-product of the meat industry, and only one older spine (4yrs old) was from a breeding ewe. For young spines, these remain intact, whereas the older spines had already been split through the sagittal plane and the spinal cord was removed at the abattoir to minimise the risk of prion related diseases.

They were stored at -20°C until they were ready to be used. The specific details of the samples used for the the data within this chapter are outlined in table 4.1.

Table 4.1: Specimen Information for Analysed Samples

Reference	Section	Age	Farm	Preparation
OvL45_1yr_Oct20_Bant	L4-L5, Anterior segment	1 year	Farm 1	Embedded
OvL45_1yr_Oct20_Cant	L4-L5, Anterior segment	1 year	Farm 1	Embedded
OvL45_1yr_Oct20_Dant	L4-L5, Anterior segment	1 year	Farm 1	Embedded
OvL45_4yr_Oct20	L4-L5, Anterior segment	4 year	Farm 2	Embedded
OvL56_1yr_Fresh_C	L5-L6, Anterior segment	1 year	Farm 1	Defrosted

For the embedding procedure, the lumbar sections were dissected to obtain a complete IVD and cut through the L4 and L5 vertebral body with a hack saw (Figure 4.1a). They were then cut in the mid coronal plane to separate the anterior and posterior sides (Figure 4.1b).

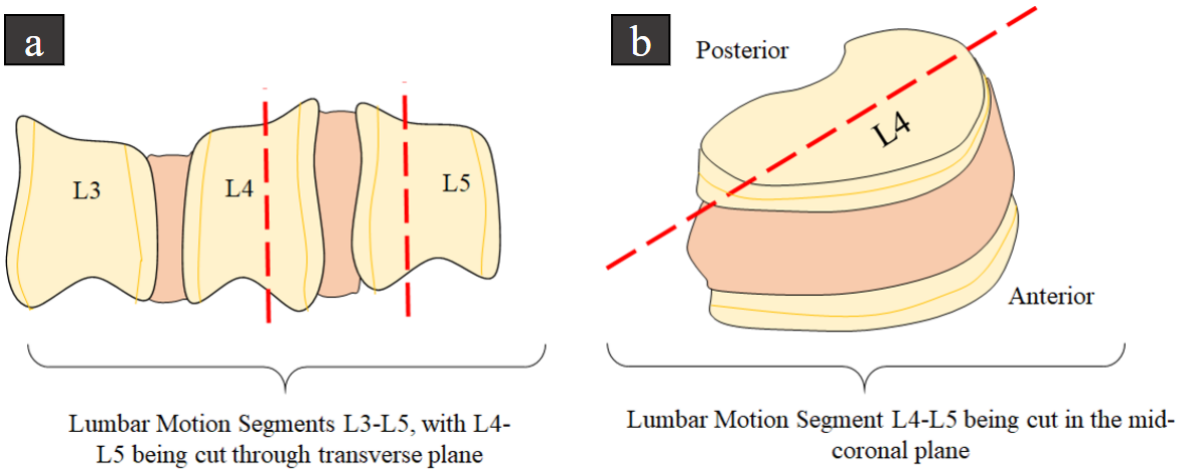

Figure 4.1: a) Lumbar segments L3-L5 with the red lines showing where cuts are made in the transverse plane to isolate the L4-L5 motion segment. b) The L4-L5 segment isolated with the red line showing where the mid coronal cut is made to expose the centre of the IVD and EP.

The samples were then gradually dehydrated in ethanol, stained with rhodamine 6G, and then rinsed in xylene, with an established protocol used in previous studies [70,299,309]. Two embedding protocols were adopted in this project,

by using cold polymethylmethacrylate (PMMA) Technovit 9100 (Kulzer Technik) and epoxy resin (EpoFix, Struers). The former has the advantage of minimised shrinking and heat damage and more importantly, enabling immunohistology on the same samples, but the immunohistology was not carried out in this PhD study. The latter has the advantages of cost and efficiency. The timescale for each procedure in the protocols were adjusted to suit the large samples in this project by trials and errors, with the final steps detailed in table 4.2 and 4.3.

Table 4.2: Sample Preparation With Cold PMMA

Step	Name	Process	Conditions
1	Dehydration 1	70% ethanol for 3 days	4°C
2	Dehydration 2	80% ethanol for 2 days	4°C
3	Dehydration 3	96% ethanol for 2 days	4°C
4	Dehydration 4	100% ethanol for 2 days	4°C
5	Staining 1	Rhodamine solution for 1.5 days	4°C on an orbital table (150rpm)
6	Staining 2	Rhodamine solution for 1.5 days	4°C on an orbital table (150rpm)
7	Xylene rinse 1	Xylene for 1 hour on orbital table (150rpm)	STP, fume cupboard
8	Xylene rinse 2	Xylene for 3 hours on orbital table (150rpm)	STP, fume cupboard
9	Xylene rinse 3	Xylene for 3 hours on orbital table (150rpm)	STP, fume cupboard
10	Preinfiltration 1	Preinfiltration solution for 24 hours in air tight containers after 10 minutes of vacuum	4°C
11	Preinfiltration 2	Preinfiltration solution for 2 days hours in air tight containers after 10 minutes of vacuum	4°C
12	Infiltration 1	Infiltration solution for 3 days in air tight containers after 10 minutes of vacuum	4°C
13	Infiltration 2	Infiltration solution for 3 days in air tight containers after 10 minutes of vacuum	4°C
14	Embedding	Stock solution A and B mixed in a ratio of 9:1 while cold, and poured over positioned samples in their holders	Fume cupboard in a polystyrene box with ice packs.

Table 4.3: Sample Preparation With EpoFix Resin

Step	Name	Process	Conditions
1	Dehydration 1	70% ethanol for 3 days	4C
2	Dehydration 2	80% ethanol for 2 days	4C
3	Dehydration 3	96% ethanol for 2 days	4C
4	Dehydration 4	100% ethanol for 2 days	4C
5	Staining 1	Rhodamine solution for 1.5 days	4C on an orbital table (150rpm)
6	Staining 2	Rhodamine solution for 1.5 days	4C on an orbital table (150rpm)
7	Xylene rinse 1	Xylene for 1 hour on orbital table (150rpm)	STP in fume cupboard
8	Xylene rinse 2	Xylene for 3 hours on orbital table (150rpm)	STP in fume cupboard
9	Xylene rinse 3	Xylene for 3 hours on orbital table (150rpm)	STP in fume cupboard
10	Preinfiltration	Epoxy resin soak overnight (15hours)	4C
11	Embedding	Solution of Epoxy resin + Hardener (15:1 by volume) in the sample holders	STP in fume cupboard

Once embedded, the samples needed to be ground and polished to get a flat surface on the Struers LaboPol-25 before imaging. Grinding with the SiC sheets started at a grit coarseness of #500 (approximately $17 - 19\ \mu m$) with water as the lubricant, and the size was gradually decreased to #1200 ($6.5\ \mu m$). Polishing was then carried out on the same machine but using the diamond suspension

solutions, from $6\mu m$, gradually down to $0.25\ \mu m$ with the LaboDoser and MD Sat, Sac, and Nap polishing cloths. The details of the grinding and polishing steps are listed in Table 4.4.

Table 4.4: Conditions for Polishing

Step	Name	Mat	Lubricant
1	Grinding 1	#500	Water
2	Grinding 2	#800	Water
3	Grinding 3	#1200	Water
4	Polishing 1	MD Sat	DiaPro $6\ \mu m$
5	Polishing 2	MD Dac	DiaPro $3\ \mu m$
4	Polishing 3	MD Nap	DiaPro $1\ \mu m$
5	Polishing 4	MD Nap	DiaPro $0.25\ \mu m$

Once polished, multiple imaging modalities were performed in a specific order (Figure 4.2). The first imaging technique used was the CLSM, followed by repolishing to remove residual microscope oil. The samples were then carbon coated for the SEM. The samples were once again repolished and then finally imaged with the multiphoton microscope. These steps are documented in detail in the following section, and the workflow could be optimised for future study as discussed later.

The fresh samples were imaged using only the multiphoton for extended scanning times required for pSHG.

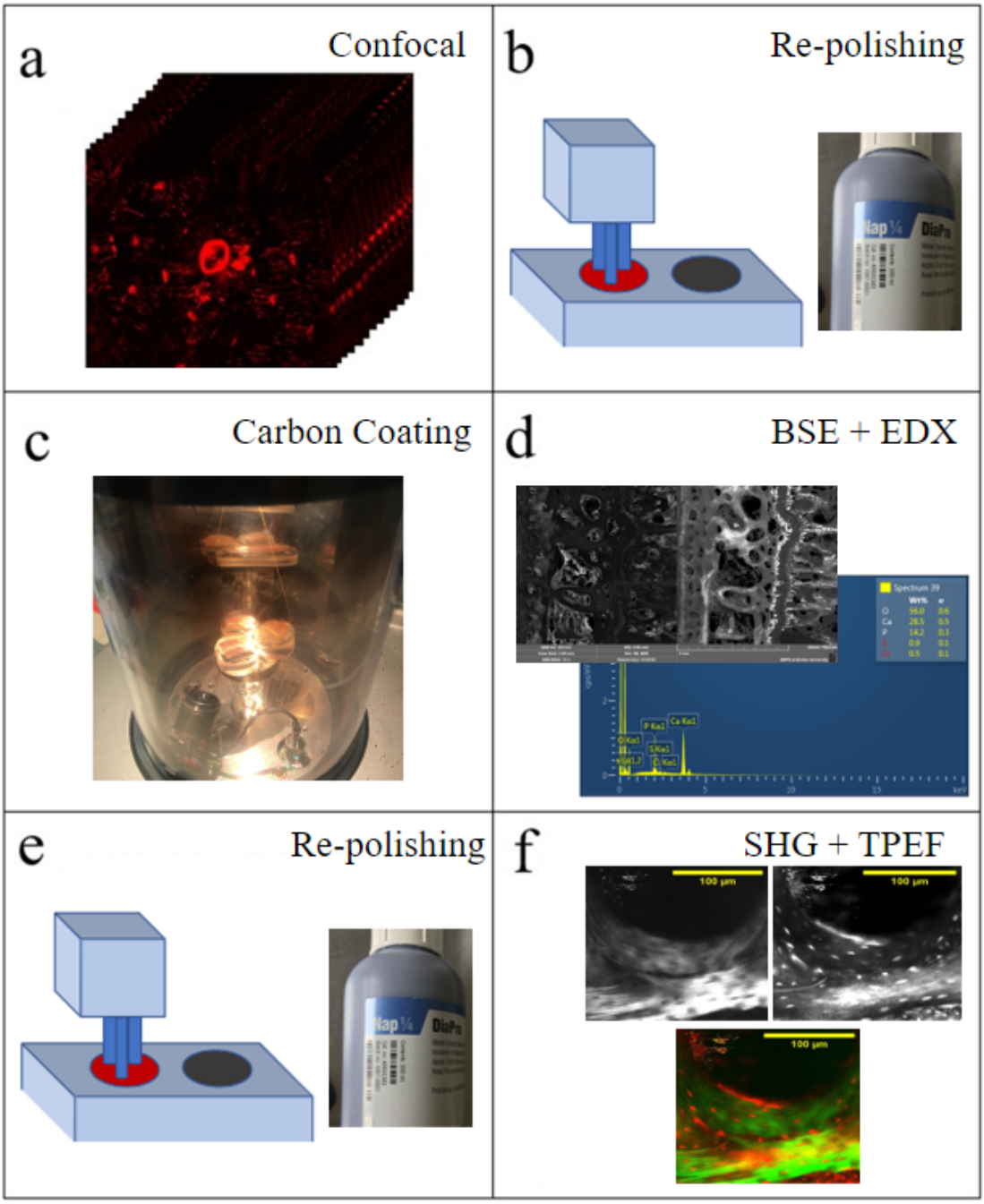

Figure 4.2: The steps taken to allow multimodal imaging of each sample. They are first imaged with the confocal microscope (a), and then repolished in (b) and carbon coated in (c) and then scanned with the SEM (d). They are then repolished in (e) and finally imaged with the multiphoton microscope (f).

The region of the samples imaged was the cranial L4-L5 VEP, with respect to the IVD, in the mid coronal plane, in the region adjacent to the nucleus pulposus (NP), shown in Figure 4.3.

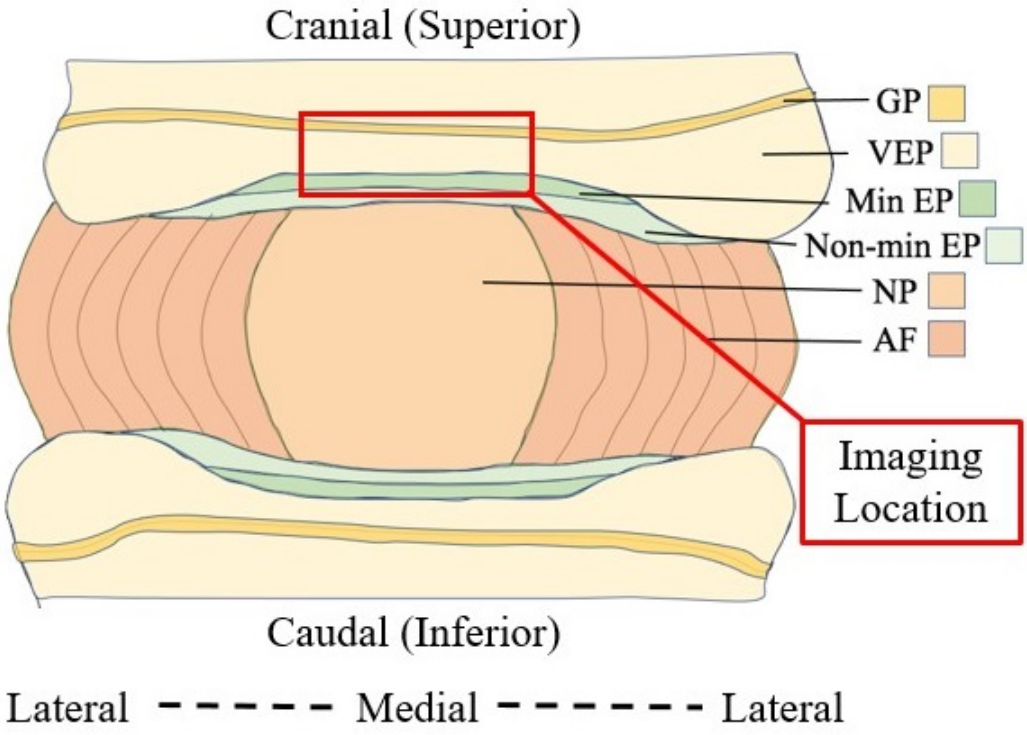

Figure 4.3: Sample schematic showing the region of interest. All imaging was done in the cranial EP, in the central area adjacent to the NP.

4.2.2 Confocal Laser Scanning Microscopy (CLSM)

4.2.2.1 Data Acquisition

The VEP was first scanned using the confocal microscope (Leica DMi8 Inverted, Leica Microsystems). Initial mapping of the sample was taken with a lower magnification lens (HC PL FLUOTAR L 20x/0.40 DRY), to quickly capture a large field of view (pixel size of $1.14\ \mu m$) of the specimen so that features that were scanned at a higher magnification (pixel size of $0.38\ \mu m$) could be located. When taking a 3D stack of images of a region, a 63X oil lens (HC PL APO CS2 63x/1.40 OIL) was used and the settings chosen were to maximise the contrast to ensure visibility of canaliculi. The imaging conditions for the z-stacks are listed in table 4.5. The excitation wavelength for rhodamine 6G is $525\ nm$ but $488\ nm$ was used due to availability of lasers. The emission spectra ranges from $548 - 600\ nm$ [270],

and so the detection range of $500 - 625\ nm$ was selected to ensure all signal from the dye was captured. Due to the nature of signal intensity decreasing when imaging further into the sample, the Z compensation feature was used where the laser power was adjusted for each slice to ensure the same level of contrast was achieved. With the image stack requiring to capture entire lacunae for analysis, the Z depth was between $24 - 40\ \mu m$, and the stack is then exported into a sequence of images in the TIFF format.

Table 4.5: Conditions for CLSM Imaging at the RILD.

Objective lens	HC PL APO CS2 63x/1.40 OIL
Z step size	$0.3\ \mu m$
Scanning speed	$400\ Hz$
Excitation wavelength	$488\ nm$
Detection range	$500 - 625\ nm$
Stack size	Approximately 80-130 slices
Gain	400 or lower
Laser power setting	40-50% (a.u.)

4.2.2.2 Image Segmentation and Network Digitalisation

Since it is not just the network which gives a signal, but also the Haversian canals and other soft tissue areas, the regions for segmentation needed to be labelled by masking. An example of a stack with a Haversion canal and the mask to remove such features are shown in Figure 4.4a. Masking was done with the Simpleware software (Simpleware, Synopsis), and after painting over the regions to be excluded from analysis on every 5 or 10 slices, the software can extrapolate

the mask to all of the slices. This can then be exported as a binary image with intensities of only 255 and 0, where 255 represents the areas to include, and 0 are the regions omitted. This creates a stack of the mask seen in Figure 4.4b, where the black is the region with a pixel intensity of 0, and represents the Haversian canal to be excluded. With Fiji, this is then superimposed slice by slice onto the entire stack and multiplied, leaving behind a stack of images with only the lacunae and canaliculi showing as the masked regions will have a pixel intensity of 0.

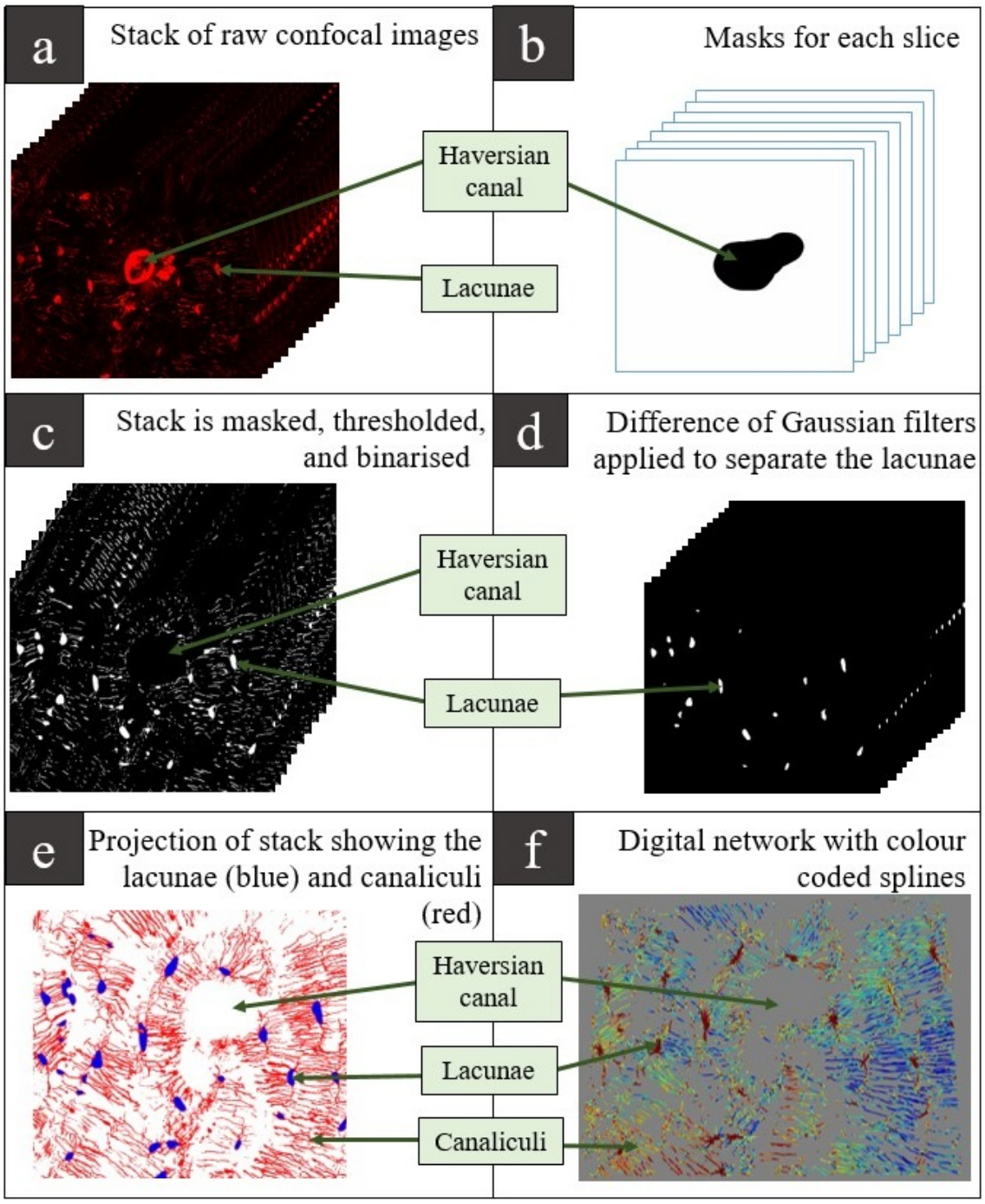

Figure 4.4: a) Stack of confocal images. b) Mask of the blood vessel from Simpleware that gets superimposed onto (a). c) The masked, thresholded and binarised stack. d) Thresholded stack to contain just the lacunae (separate from canaliculi). e) A projected image of the lacunae (blue, from (d)) and canaliculi (red). f) Mayavi 3D plot of the network colour coded by cylindrical coordinates.

4.2.2.3 Network Topology Quantification

Quantitative analysis was done using TINA (Tool for Image and Network Analysis) which is a tool developed by Felix Repp [310,311] (MPIKG) in Python. It seg-

ments the canalicular network and cell lacunae from a stack of images through the process of thresholding, binarising, and skeletonisation. Features that can be quantified by TINA include the length, orientation, and connectivity of canaliculi, and the cell volumes, oblateness, and orientations of osteocyte lacunae [310].

In the segmentation process, adaptive thresholding was applied and the difference in gaussians (DoG) of localised pixel intensity was used to identify the edges of canaliculi and lacunae. The background signal was filtered out, without losing low intensity signal regions containing features that are of interest [310]. In a nutshell, the DoG method filters images by applying 2 separate Gaussian smoothing functions, differentiated by the width of their kernels (i.e. the shape of Gaussian distribution), and taking the difference between the two resulting images to result in highlighted details at different scales, with reduced noise. TINA used the ratio between two images smoothed with specified kernel widths to obtain the canaliculi, and the process was repeated with two different kernel widths to create a DoG filter for the osteocyte lacunae. The six DoG parameters (two kernel widths and the threshold ratio for both canaliculi and lacunae) were chosen by an interactive script in Jupyter Notebook so that the effects of the kernel widths and threshold ratio value could be seen in real time when adjusting the values via widgets for the optimised settings. The thresholded stack was then binarised so that the lacunae and network had the maximum intensity grey scale values of 255, and the mineralised matrix and masked regions had the lowest intensity values of 0. An example of a binarised stack is in Figure 4.4c.

Skeletonisation involved the surface voxels in the binarised stack with high intensity being erased from the 3D structure until there was a continuous thread through the stack of 1 voxel thick. The continuous threads of pixels were the

canaliculi, and the lacuane remained in volumes of pixels [312, 313]. The analysis of lacunae and canaliculi could then be separated, which Figure 4.4d shows by the isolation of the cell lacunae in the binarised and skeletonised stack. A projected image of the skeletal 3D stack is shown in Figure 4.4e, where the canaliculi are shown as red, and the lacunae are blue, and correspond to the 3D lacunae data in Figure 4.4d.

Four topological parameters are then quantified on the architecture of the canalicular network. The first parameter is the canaliculi density ($CaDn$) which is the total length of the skeletonised network ($L_{Network}$) divided by the 3D stack volume (V_{All}) minus the volume of the lacunae ($V_{Lacunae}$) (Eq. 4.1). The unit for $CaDn$ is in $\mu m/\mu m^3$.

$$CaDn = \frac{L_{Network}}{V_{All} - V_{Lacunae}} \tag{4.1}$$

The CaDn for these samples are assessed as a function of the % distance between the non-mineralised CEP, and the growth plate, with the saturation of rhodamine in the two soft tissues in the low magnification maps providing identifiable landmarks for the analysis.

The second parameter quantified is the orientation of the network, calculated by applying parametric splines to the skeletonised network, fitted with a third order function (k=3). These fitted splines result in the quantification of the orientation and length of each segment of the network by replacing the discrete points in the skeletonised network with a series of nodes (points of branching in the canaliculi) and smooth splines with a length scale comparable to a voxel [310, 314]. The cartesian and polar coordinates and angles for these splines are exported and can be used for plotting the 3D network to visually determine the patterns in

canaliculi direction. For this chapter, polar cylindrical coordinates are used, and the frame of reference is that the centre of the Haversian canal is the centre axis of the cylindrical system. The splines are then individually colour coded depending on their angle to the Haversian canal. Figure 4.4f shows the digitalised network with colour coded splines, where the dark blue splines point into the direction of the Haversian canal (radial), and red splines are circumferential. The Haversian canals in long bone are predominantly organised with the length parallel to the loading axis in long bones, and the canaliculi network in the corresponding osteons has a dominant orientation which is radial to the centre of the Haversian canal (centre of the osteon) [315, 316].

Thirdly, the locations of where branching occurs in the network, known as nodes, and the degree of connectivity for each node are assessed by the number of neighbouring voxels at each point. A voxel with only one neighbour is going to be the network at the edges of the image stack, or at artefacts with dead-ends. Two neighbours is the continuous skeletal form of the canaliculi, and so are not considered nodes. Three nodes or more are what are physically significant for the connectivity of the network. Three nodes are where branching occurs in the network, and is the most frequent of these nodes. A degree of connectivity or four or more do exist, but becomes statistically more improbable with higher values [310]. Lastly, using the clusters of the voxels in the skeletonised model, the morphology and coordinates of the lacunae are determined and exported, with the same coordinate system as the canaliculi. For this data, a Matlab script was developed to plot the Voronoi diagram of these locations in 2D and colour coded to represent the relative area of the Voronoi cells. The Voronoi cells at the edge of the data sets were excluded due to edge effects skewing the data. This

graph shows the area of the matrix which is regulated by each cell.

For the analysis of these quantities, the tissue volume imaged was partitioned into small subvolumes so that the heterogeneity throughout the stack can be assessed. To choose an appropriate size for the subvolume, a convergence test was conducted on subvolumes ranging from 50 μm^3 to 300 μm^3. If the volume was too small, the quantities would not be representative to the local regions and only show extremities. If the subvolume was too large, the spatial distribution of the CaDn could not be observed due to the fact that the average CaDn per subvolume encompasses too large a percentage of the stack. The effects of different subvolume sizes are shown in Figure 4.5, where the red data shows a small volume of V=50 μm^3, which has a broader peak than the other data in this graph, and a peak at a higher CaDn. The increasing subvolume CaDn are plotted until V=300 μm^3, where the peak becomes narrower, converging on the average CaDn value for this data set. For the analysis in this chapter, a subvolume size of 125 μm^3, indicated by the green data and fitted line in Figure 4.5, was used.

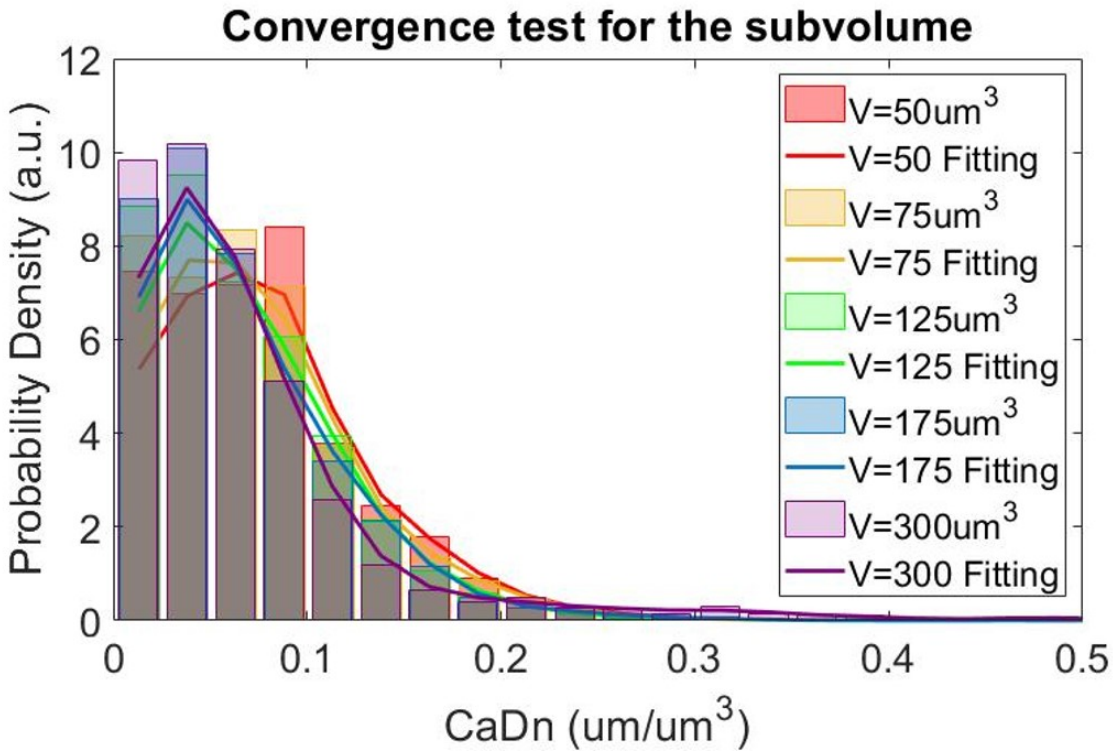

Figure 4.5: Convergence test for the range of CaDn values with different subvolumes. Volumes that are small (red) tend to produce a distribution with extremes of higher CaDn and lower CaDn, whereas volumes that are large (purple) will converge on the overall average, with a narrower distribution.

4.2.3 Back Scattered Electron (BSE) Imaging and Energy Dispersive X-ray (EDX) Spectroscopy

After imaging with the confocal laser scanning microscope, the samples were repolished with the 0.25 μm diamond suspension solution for approximately one minute, in order to remove any residual oil (Figure 4.2b), and sputter coated with carbon (Figure 4.2c). Coating (using the Quorum Q150T ES Plus) was done with the 'pulsed rod evaporation' method to get a carbon coat between 20-30 nm thick evenly on the samples [317, 318].

The coated samples were imaged with the Tescan VEGA3 SEM (Figure 4.2d) with the scanning conditions summarised in Table 4.6. The backscattered electron mode (BSE) was used as the variation in pixel intensity depicts the variation

of mineral density, as explained in chapter 3. EDX was performed over different regions, using the area select tool to get the averages across multiple regions of interest.

Table 4.6: Conditions for SEM Imaging

HV	20 kV
Mag	200x
FOV	1038 μm
Speed	7 or 8 (100 or 320 μs/pxl)
WD	$\simeq$17 mm
Contrast	$\simeq$70%
Brightness	$\simeq$60%
Beam intensity	10
Absorption current	$\simeq$80 pA
Spot size	180 nm

The EDX data was analysed by extracting the weight % of particular elements by the techniques explained in chapter 3, in particular calcium and phosphorous, and comparing these for each spectra, and the values for the different regions were plotted in different colours.

4.2.4 Second Harmonic Generation (SHG) and Two-Photon Excitation Fluorescence (TPEF)

Prior to imaging with the multiphoton microscope, the samples were once again repolished to remove the carbon coat after imaging with SEM (Figure 4.2e). The multiphoton microscope provided two simultaneous modalities (Figure 4.2f). SHG

allowed studying of the collagen organisation, and TPEF captured the rhodamine signals comparabe to CLSM images. A 25x water-immersion lens (Olympus XLPLN25XWMP) provided a balance between the details and the field of view. The field of view is zoomed in by 2x to capture a square frame instead of a circle. The pixel bin factor corresponds to the dwelling time of each pixel, and so a higher pixel bin factor produces images with a greater signal to noise ratio. The detector input voltage was set between -10 and 10 volt to capture the maximised details in the images. These conditions are outlined in Table 4.7. It should be noted that, a higher laser power produces better images, as the signal to noise ratio is higher; however, with the rhodamine staining, a high laser power can lead to burning of the sample. Similarly, an extended scanning time for polarised-SHG (pSHG) was more likely to cause burning samples. Therefore, different scanning conditions were adopted for pSHG and quantitative analysis than the single-frame SHG/T-PEF images. In this chapter, the SHG and TPEF measurements were performed with the embedded samples, whereas the pSHG was done with a fresh spine sample due to the long scanning time required.

Table 4.7: Conditions for Multiphoton Microscopy (MPM) Imaging of both single image acquisition (SHG + TPEF) and the stack collection of pSHG

Condition	SHG + TPEF	pSHG
Lens	25x water	25x water
NA	1.05	1.05
Zoom	2	2
Frame size	512x512	512x512
Pixel bin factor	60	40
Frame average	3	1
Angle of waveplate	20-25°	13-18 °
Gain	700	700
Input voltage	-10:10	-10:10

4.3 Results

4.3.1 Osteocyte Lacunae Canaliculi Network

4.3.1.1 Observable Features under CLSM

The features seen in the confocal images are the result of rhodamine staining of the non-mineralised regions and include the non-mineralised EP, chondrocyte lacunae, osteocyte lacunae, canaliculi, blood vessels and bone marrow channels. An annotated map showing the larger features are seen by both confocal and optical image in Figure 4.6 a and b respectively. These are separate samples but the optical light image illustrates where the rhodamine dye accumulates on this scale (dark pink), and therefore helps to show why there are regions of saturation in the confocal image (red). The IVD and non-mineralised CEP is indicated by the red saturation at the top of the confocal image (Figure 4.6a), and due to the non-mineralised nature of this tissue, the boundary between the non-mineralised CEP and the IVD is unable to be determined via this method. The chondrocyte lacunae within the mineralised CEP are the round red features just below the non-mineralised CEP, and are often situated in pairs or column clusters. The blood vessels are much larger than the cell lacunae, and are continuous within the 3D stack, and show where the Haversian canal of the osteons are. Due to Haversian remodelling, there is interstitial bone present in all samples as a remnant of older osteons (interosteonal bone), situated between the identifiable osteon structures (intraosteonal bone). Other large features seen are the marrow channels situated amongst the trabecular bone, and another cartilaginous boundary is the growth plate, which is indicated by a region of saturation towards the bottom of Figure 4.6.

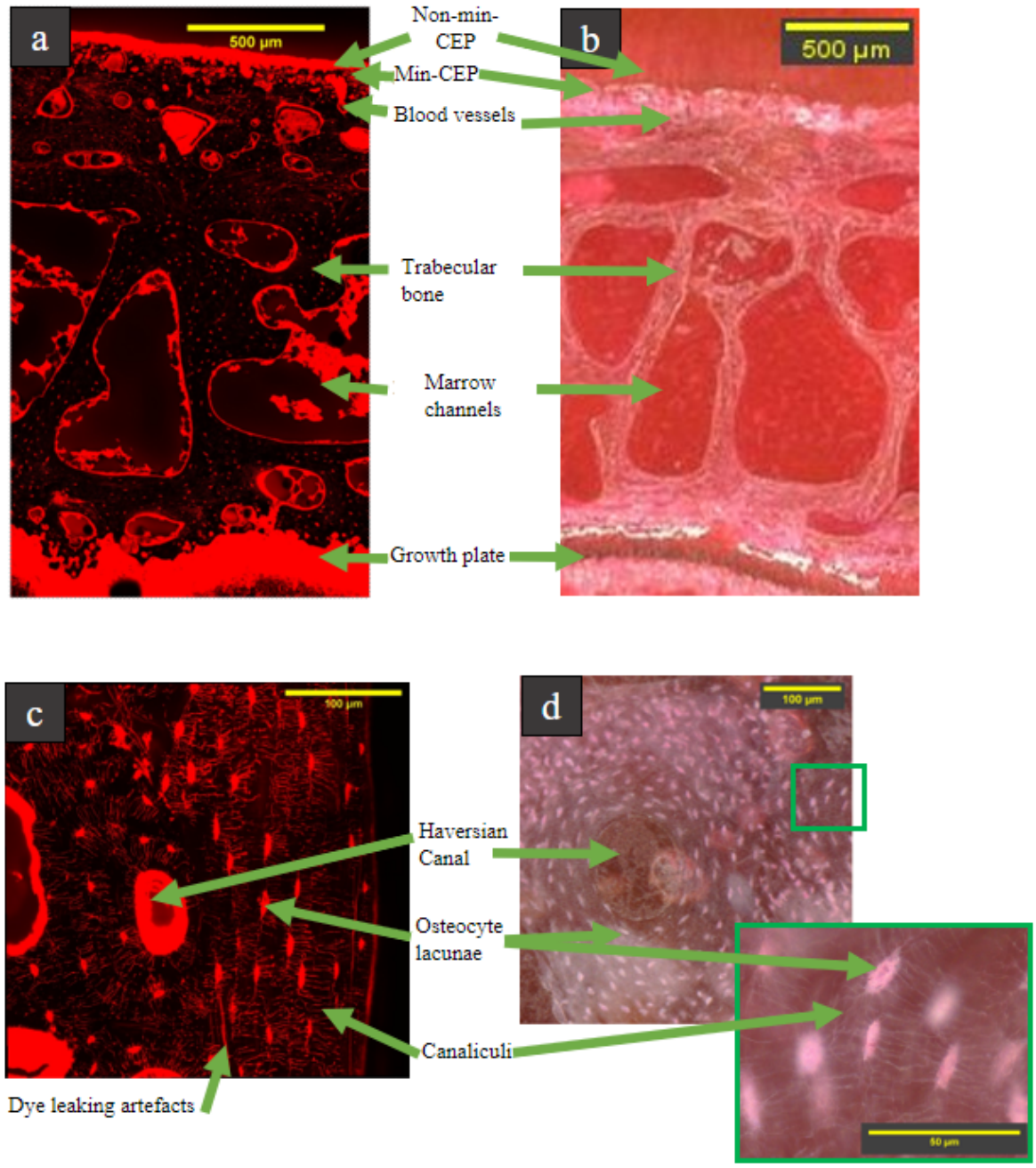

Figure 4.6: Qualitative overview of features within the VEP under CLSM and optical microscopy on different samples but of the same regions. a) A confocal map of a strip of the VEP from the non-mineralised CEP (top of image) to the growth plate (bottom of image), and in b) the same region on a different sample is imaged with the optical microscope . (c) shows the CLSM image on a smaller scale, where the osteon structure, lacunae and canaliculi can be observed. In (d) an osteon structure is imaged by the optical microscope, with the green box highlighting the presence of the canaliculi at this scale.

In Figure 4.6 c and d, smaller structures in the VEP can be seen, with the osteocyte lacunae being easier to distinguish as smaller and more elliptical volumes, with the presence of cell processes, unlike that of the chondrocyte lacunae. The

staining of where these cell processes lie are the canaliculi, which can be seen to connect the osteocyte lacunae to each other and to a blood supply in Figure 4.6c. The corresponding optical image of the canaliculi is shown by the green box in Figure 4.6d. What can also be seen at this scale is dye that does not appear to resemble the canaliculi, labelled as 'Dye leaking artefacts' on the confocal image in Figure 4.6c. These artefacts occur when there are fractures in the mineral matrix and are discussed later in this chapter.

4.3.1.2 3D view of canaliculi direction

When the 3D stacks were imported into Synopsis (SimpleWare, Synopsis) for masking, a 3D model was obtained which provides a different perspective of visualisation than seeing images one by one. One of the features seen in the samples is the apparent change in canalicular direction over a relatively small distance (<100 μm). These two regions, indicated by the purple boxes in Figure 4.7a and the purple 3D models in Figure 4.7b and c, show that the canaliculi direction can change by 90° with the overall direction pointing towards the closest blood vessel.

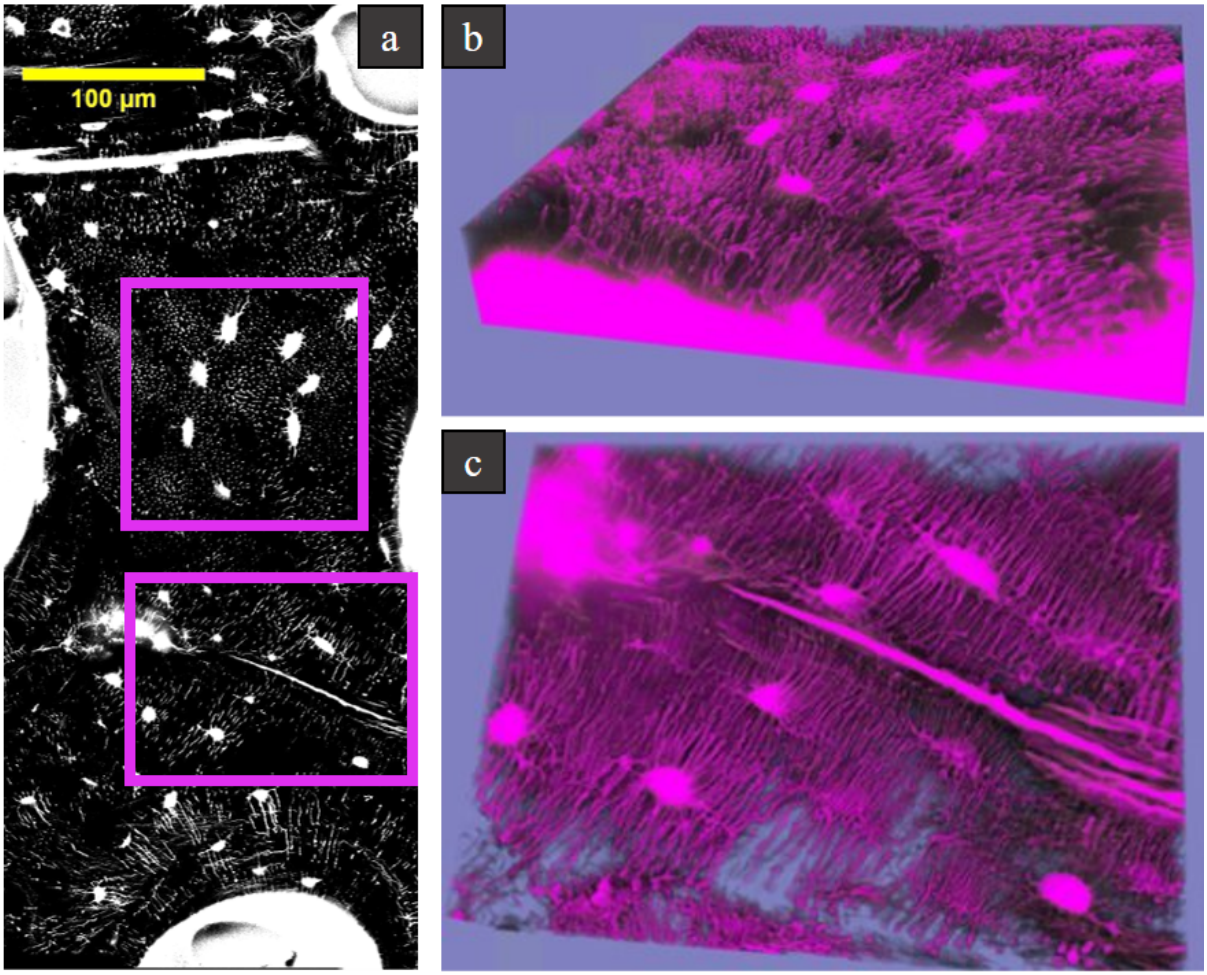

Figure 4.7: a) A slice of the confocal stack, showing the canaliculi as small dots in the imaging plane (top pink square), and as lines (bottom pink square). 3D networks of the regions in purple boxes on the single slice. b) The 3D network showing that the dots in the top square in (a) are canaliculi oriented in a direction in the z-plane, and facing towards a blood vessel (saturation at bottom of stack). c) The canaliculi direction being in the xy plane of the images, corresponding to the region in the bottom square in (a). *N=1*

4.3.1.3 Quantified Lacunae Domains and Canaliculi Densities Across the VEP

The segmented confocal images were projected and shown in Figure 4.8a, in which the red colour indicates the canaliculi of the OLCN and the blue is the lacunae. With the subvolume chosen, the spatial distribution of CaDn is plotted in Figure 4.8b, where the regions with a higher density were shown with yellow, and the lower densities in dark blue. For the lacunae density, a Voronoi plot (Figure 4.8c) was obtained from the coordinates of each lacuna, and colour coded to show the domain of each lacunae. For this, the cells are plotted in 2D to correlate

with the CaDn plot, and so the density for these would be area per lacunae. The dark blue Voronoi cells are smaller lacunae domains, and hence a higher lacunae density, and the yellow shows a more sparse population of lacunae with larger domains.

From these graphs it can be seen that the higher CaDn (yellow regions in Figure 4.8b) corresponds to where the lacunae domains are lower (dark blue in Figure 4.8c).

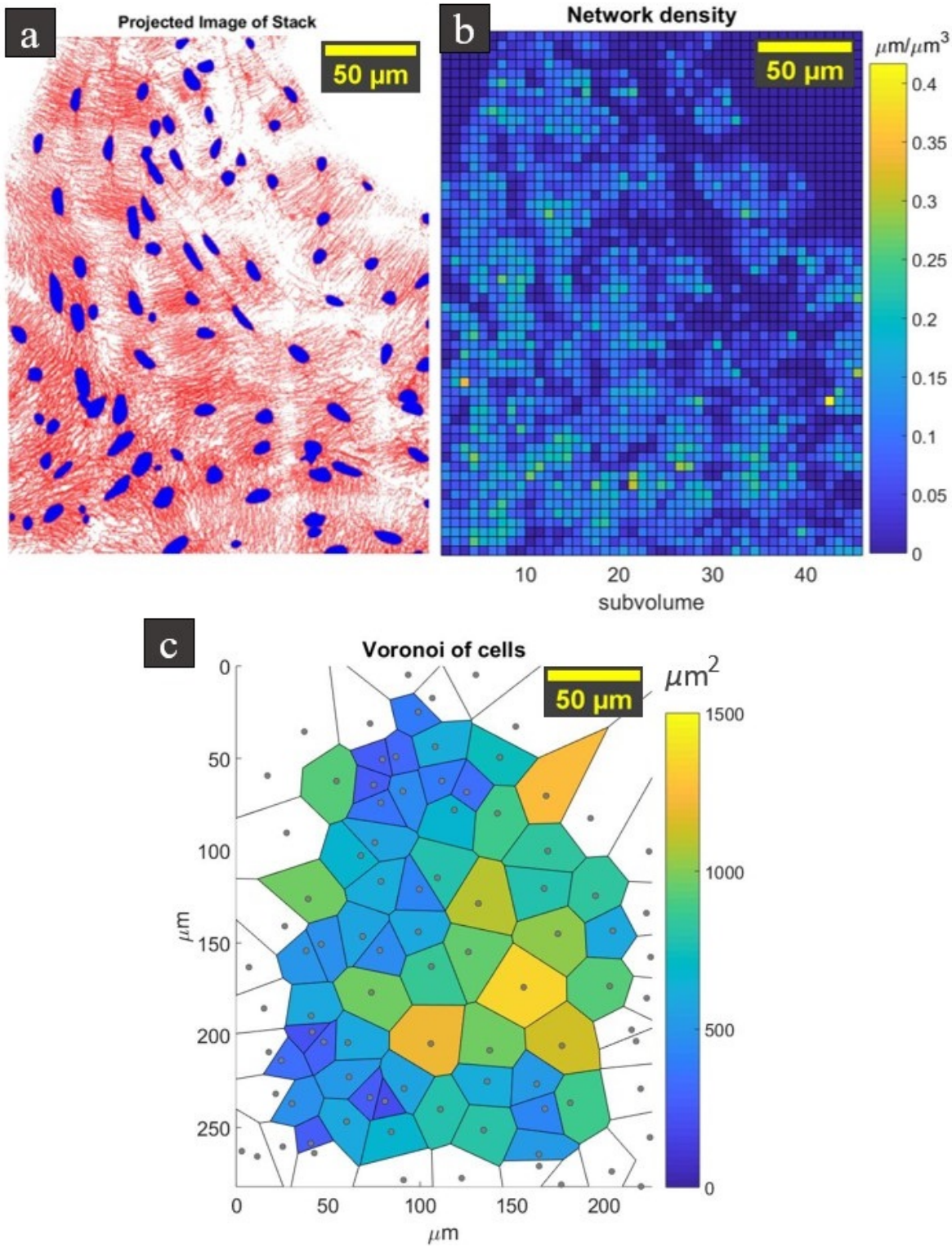

Figure 4.8: Spatial correlation between CaDn and Lacunae density. a) Visual representation of the lacunae and network for the entire stack. b) CaDn values for the average value within a subvolume (square). Dark blue for the network density indicates a low value or an area with none. Yellow subvolumes indicate higher CaDn. c) Voronoi plot of the lacunae area density, where each segment indicates the area (μm^2) closest to that specific lacunae. Areas in yellow have a larger area, whereas blue indicates smaller values. Edge cells have been omitted due to edge effects. *N=1*

4.3.1.4 Canalicular Density

On the large organ scale, the CaDn for each data set has been plotted as a function of the normalised distance from the non-mineralised CEP to the growth plate, and is shown in Figure 4.9. The error bars are the standard deviation for the data sets, and it can be seen that the values of the CaDn range from 0.0451 $\pm$ 0.044 to 0.13 $\pm$ 0.06 $\mu m/\mu m^3$.

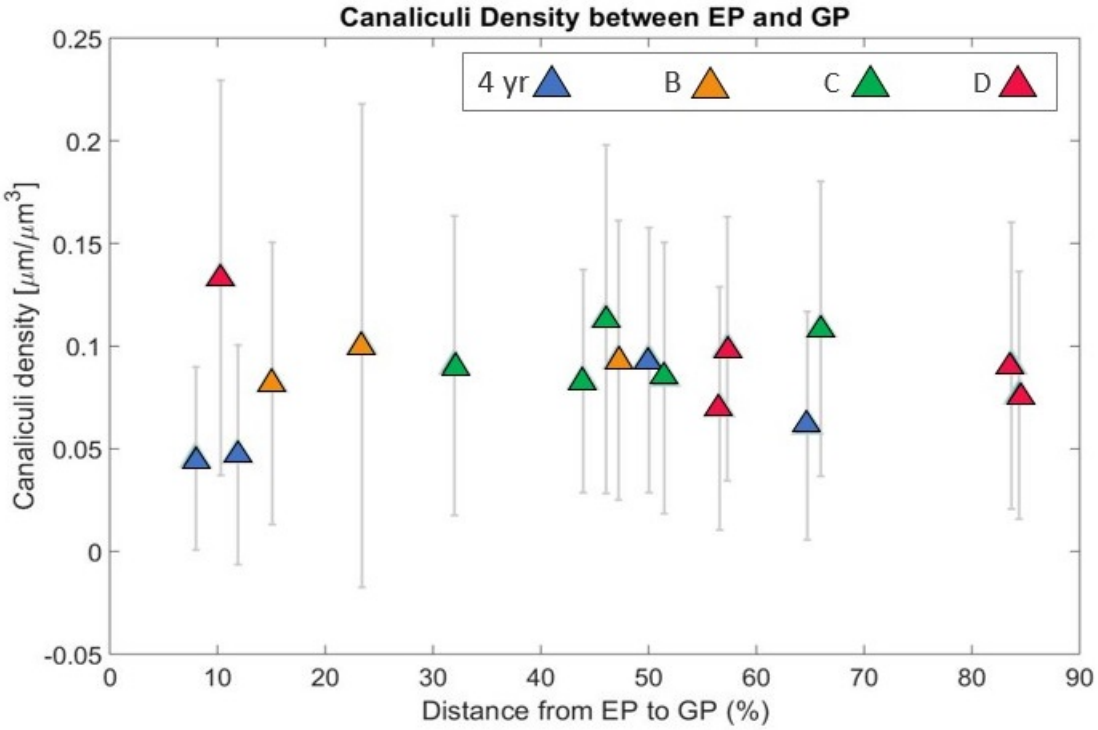

Figure 4.9: Plot of average CaDn as a function of distance from the CEP tidemark to growth plate, with the samples indicated by the colour of the marker. *N=4*

The intraosteon (osteonal) bone region is plotted in Mayavi and shown in Figure 4.10a, where the network colour signifies the direction of the canaliculi. Blue indicates canaliculi direction towards the Haversian canal, and red is perpendicular. In Figure 4.10b, the interosteon space (or insterstitial bone) of the same sample is plotted, with the white asterisks in a and b representing the same location.

To investigate the intra and interosteon variations, histograms of CaDn os-

teonal bone are plotted in Figure 4.10c. The peak positions and the full width at half maximum (FWHM) of these histograms indicate the most probable CaDn value and the heterogeneity of CaDn respectively between the two bone structures. The intraosteon tissue (blue) has a mean CaDn of 0.101 $\mu m/\mu m^3$ and a peak CaDn value of 0.046 $\mu m/\mu m^3$. The interosteon bone (red) also has a peak CaDn of 0.046 $\mu m/\mu m^3$, but with an average CaDn of 0.087 $\mu m/\mu m^3$. Despite the similarity of the peak values, there is a difference in the broadness of these peaks, where the intraosteon bone fitting is wider, with a FWHM of 0.17, and therefore has a greater range of CaDn values, than the interosteon which has a FWHM of 0.14.

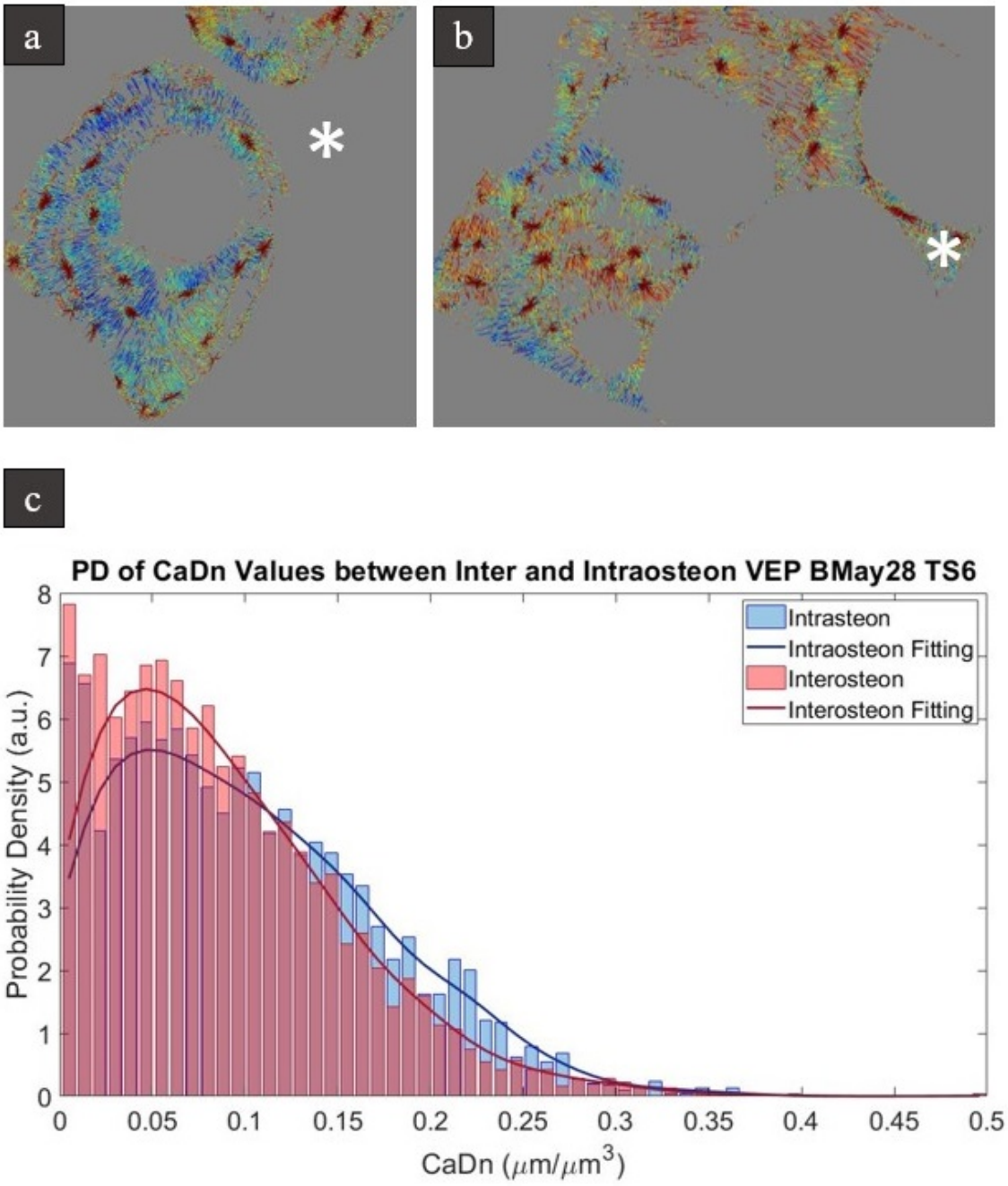

Figure 4.10: a) 3D network plotted by cylindrical coordinates of the osteons which correlates to the intraosteon data in (c). b) The 3D network of the interosteon bone, from the surrounding area of (a), which correlates to the data shown in red in (c). In (a) and (b) the white asterisk represents the same location on the raw data set which has been segmented into intraosteon (a) and interosteon (b) for this data. c) The histogram of the CaDn values for each subvolume between the intraosteon bone (blue), and the interosteon bone (red). *N=1*

4.3.2 Mineralisation Data

4.3.2.1 Back Scattered Electron Imaging and Quantification

With BSE the pixel brightness is proportional to the mineral density, and so brighter regions indicate a higher concentration of calcium in these samples. In Figure 4.11 the width of the VEP has been mapped to show how it varies from both peripheries (yellow box) to the centre (blue box). On this large scale map the notable observations consist of the hypermineralised CEP which does not extend to the peripheries, but is present centrally (more clearly seen in the blue box); the distribution of the marrow channels; and the hetereogeneity of minerals, where there are regions of hypermineralisation in the trabeculae and hypomineralisation within the osteon structures.

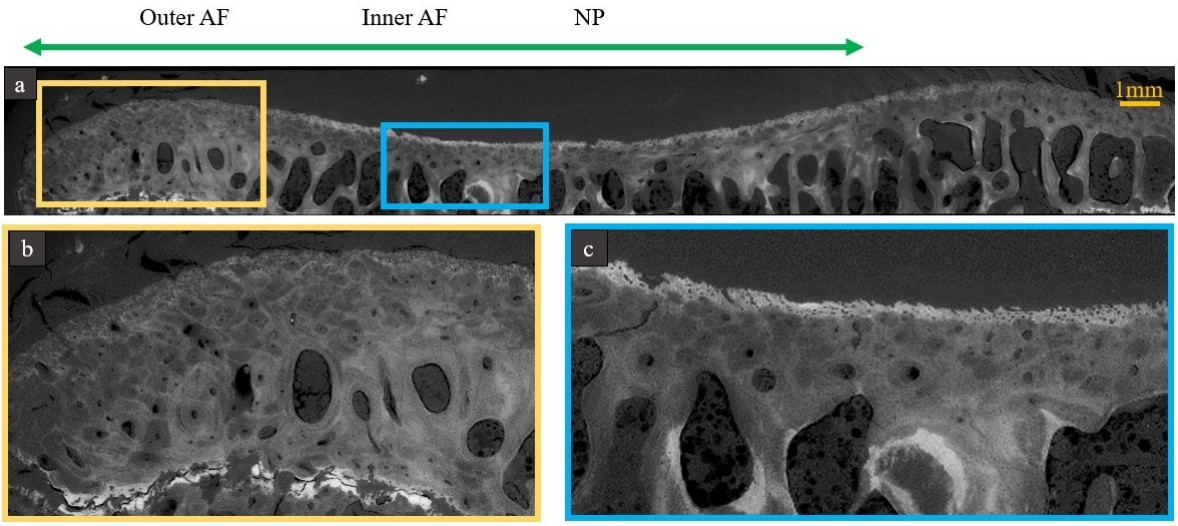

Figure 4.11: (a): BSE images of the cranial L4-L5 vertebral EP. Greater degrees of mineralisation are shown by a brighter pixel, which can be seen in the bottom images, where the periphery in the yellow box, (b), shows comparatively little variation of mineralisation in the VEP except at the growth plate, whilst the central region in the blue box, (c), has hypermineralised regions at the EP, and in areas in the trabeculae. *N=1*

The regions in the centre are segmented into the mineralised CEP, the osteon rich subchondral bone plate (SBP), and the trabecular bone, and the marrow channels and blood vessels are masked out. The pixel intensities of these miner-

alised regions are extracted and plotted in Figure 4.12. From these histograms, the hypermineralisation of the mineralised CEP (yellow) can be seen by the shift of the peak to higher relative pixel intensities, with a peak at 0.49, compared to the two boney regions which both have their peak at 0.31. The FWHM of the mineralised CEP (0.32) shows that there is a greater range of probable values in mineralisation compared to the two boney regions, where the trabecular bone and SBP have FWHM values of 0.23 and 0.16 respectively. Between the SBP and trabecular bone, the wider peak of the trabecular region indicates greater heterogeneity in the degree of mineralisation, than that of the osteon rich SBP.

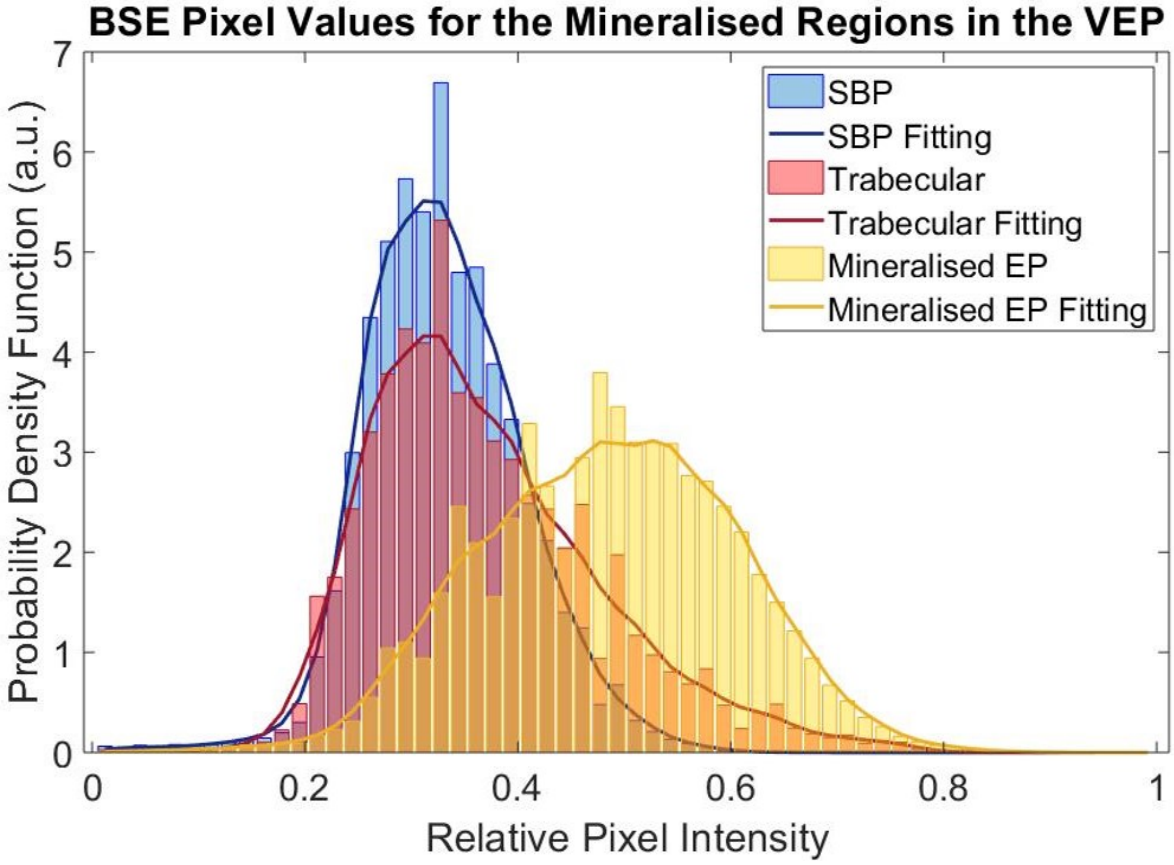

Figure 4.12: Histogram of relative pixel intensity from the BSE data, and hence, degree of mineralisation, of the three distinct regions in the central VEP. The Mineralised CEP has the highest mineral density, and is shown in yellow. The two boney regions are the subchondral bone plate (red) and the trabecular bone (blue), both with a peak at 0.31, but with FWHMs of 0.16 and 0.23 respectively. *N=1*

4.3.2.2 Energy Dispersive X-ray Spectroscopy (EDX) Data

EDX was carried out in the central location of the VEP (above the NP, midway between EP and GP) to determine the elemental composition on the embedded samples, to help verify whether the features seen in the BSE images were differences in mineralisation, or due to artefacts. The EDX spectra were averaged for an area of interest, to ensure the effects from surface contaminants were negligible, and for each feature of interest, several areas of spectra were taken, including hypermineralised and non-hypermineralised lamellar trabecular bone, interstitial bone, and mineralised lacunae.

Figure 4.13a shows the secondary emission image with the areas highlighted in the coloured boxes, with the corresponding BSE signal in Figure 4.13b. The colours of the boxes represent the areas of similar appearance and multiple are used to gather more data and minimise the effects of the lacunae voids.

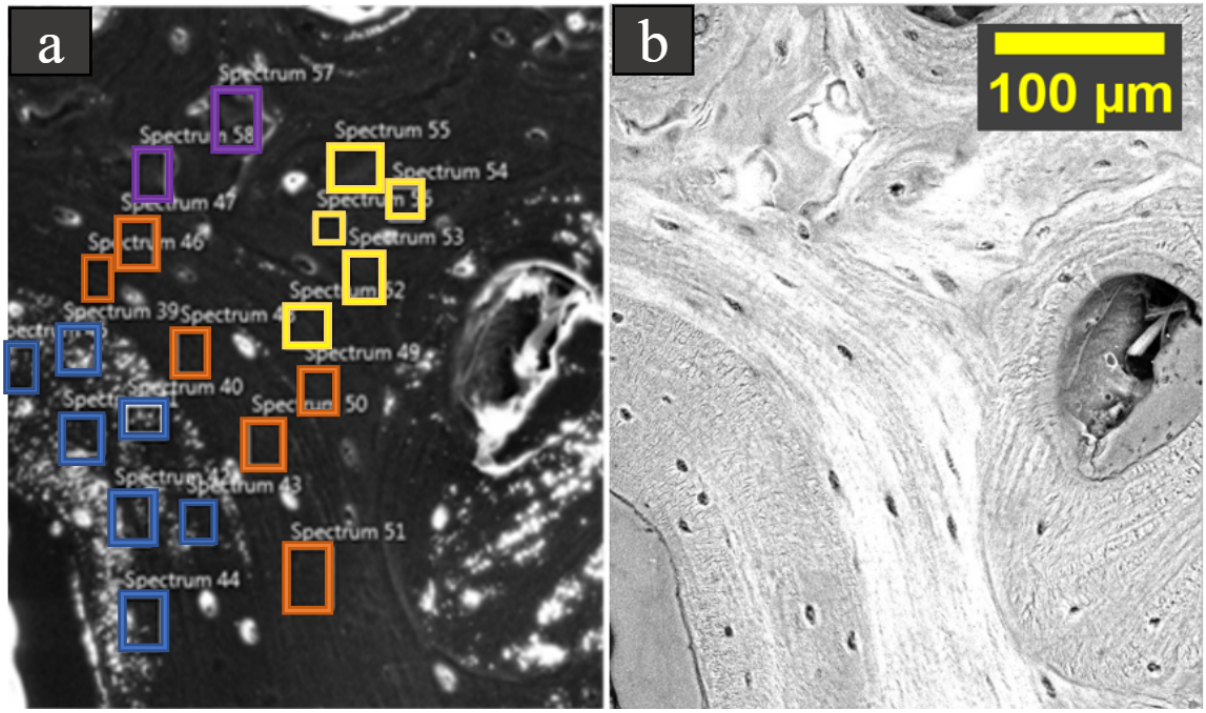

Figure 4.13: The locations of where spectra were taken for EDX in both SEM (a) and BSE (b), to compare the elemental composition of regions with different BSE signals. These regions are the non-hypermineralised trabeculae region, Region 1 (blue), the hypermineralised region, Region 2 (orange), the interstitial (interosteonal) bone, Region 3 (yellow), and the mineralised lacunae of no longer viable osteocytes, Region 4 (purple). *N=1*

Figure 4.14a and b show the calcium and phosphorous weight distribution, where the plots are colour-coded to the areas in Figure 4.13. For the majority of spectra, there is a correlation between the calcium and phosphorous weight content. In Figure 4.14c, the ratio of the minerals for each spectra is plotted to highlight the correlation between the two elements, with Regions 1, 2 and 3 having values between 1.95 and 2.1. However, for the mineralised lacunae in Region 4, the areas which contain the highest pixel intensity, the ratio of the minerals changes drastically, and the relative amount of phosphorous is reduced. The phosphorous ratio is an indicator of remodelling, with low phosphorous indicating a slower remodelling rate due to carbonate substitution. This data is evidence for anomalous regions within the VEP that are hypermineralised and with slow remodelling rates, where osteocytes can no longer orchestrate the mineralisation

process in the bone.

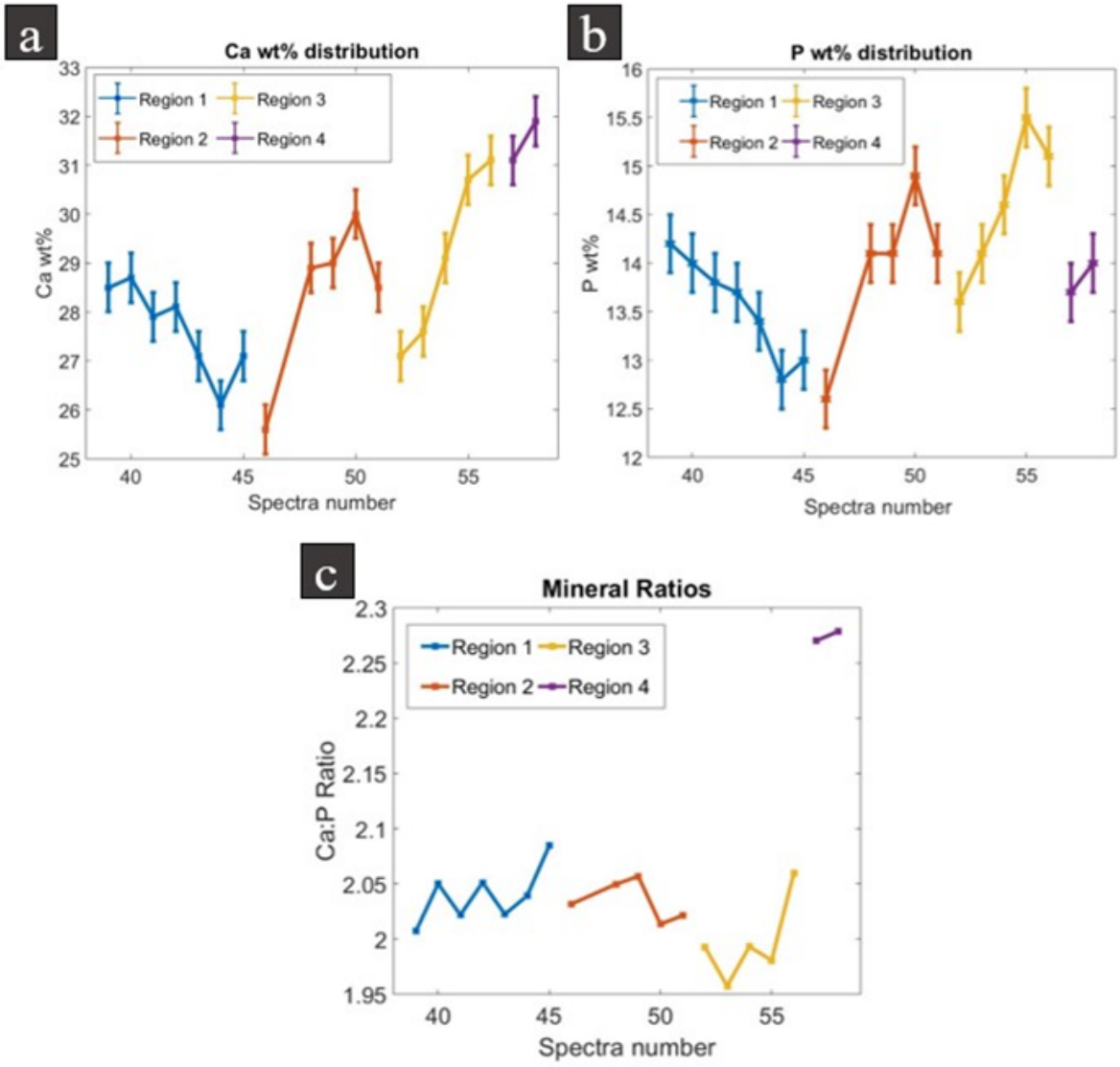

Figure 4.14: The EDX data for the minerals within the VEP, colour coded to match the regions in Figure 4.13. a) Ca wt% for each spectra. b) P wt% for each spectra. c) The mineral ratio (Ca/P) for each spectrum. *N=1*

4.3.3 Collagen Organisation

4.3.3.1 Macroscale Mapping of the 2D Collagen Organisation

Before looking into the microscale organisation of the collagen, it is important to verify and categorise the global distribution of collagen. Figure 4.15 shows a map of the CEP and VEP above the nucleus pulposus, with SHG (Figure 4.15a) showing the collagen, and with the corresponding rhodamine signal shown by

the TPEF signal (Figure 4.15b). The merged image shows how the features in these overlap in Figure 4.15c. In the SHG signal, the boundary between the type I collagen, and type II is apparent, with a sharp boundary between the bone and the mineralised cartilage. The soft tissue is saturated with rhodamine, and so the TPEF signal provides evidence of the boundary between the mineralised CEP and the non-mineralsed CEP. Other structures seen include osteons, located in the VEP close to the EP, which have a radial collagen (SHG) pattern, and a central blood vessel indicated by a lack of SHG and a bright TPEF signal at the blood vessel wall.

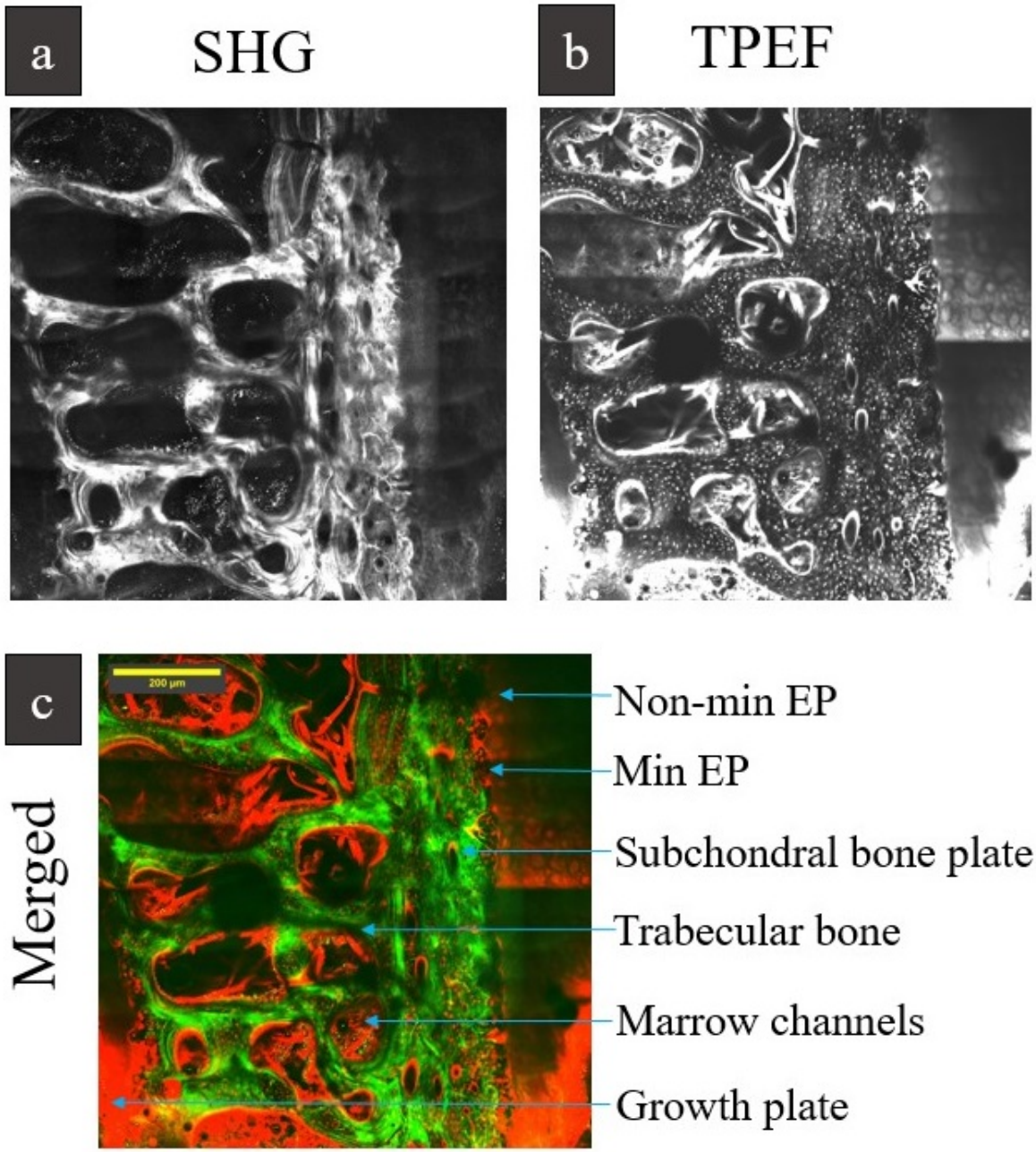

Figure 4.15: A stitched map of the central region of the CEP, with the SHG being shown in (a), and as green in the merged image (c). The TPEF (rhodamine signal) is shown in (b), and in red on the merged image (c). On the left of these maps is the growth plate, whereas the CEP is on the right. *N=1*

In Figure 4.16 a map of the peripheral region of the EP is shown. The VEP with trabeculae and the marrow channels are still noticeable, but the boundary has a different collagen alignment. At the periphery of the VEP, the type I collagen bundles of the outer annulus fibrosus (OAF) anchor directly into the bone, in the form of Sharpey fibres, visible in Figure 4.16a. These can be seen here with the

fibre direction continuing between the two mechanically different tissues, and the OAF having a more fibrous structure than that of the CEP. The TPEF signal in Figure 4.16b shows where there are regions of rhodamine accumulation, which on this scale shows the growth plate, marrow channels, and non-mineralised EP. Figure 4.16c shows the merged image of the SHG (green) and TPEF (red), and the distinct regions are annotated.

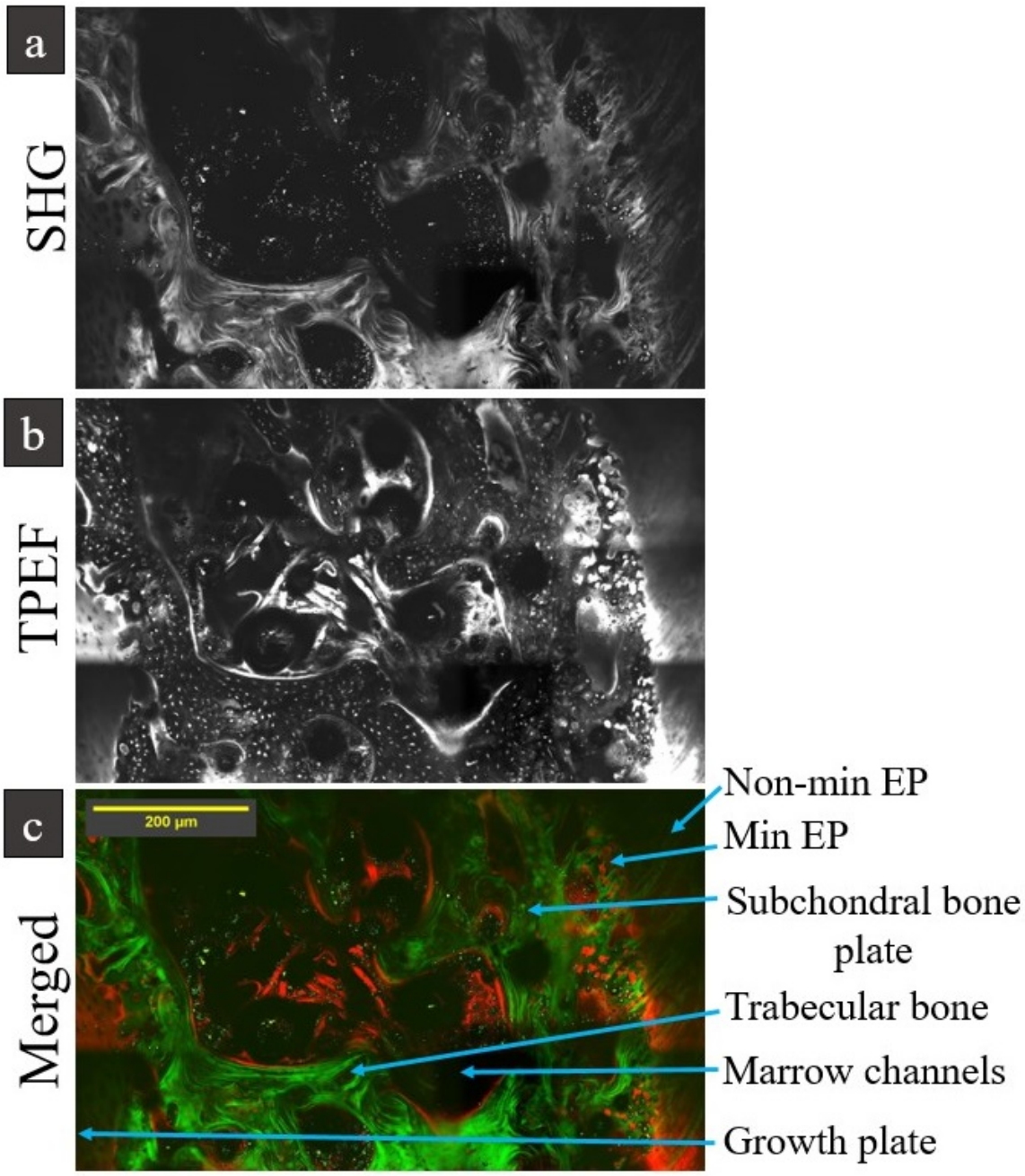

Figure 4.16: A stitched map of the peripheral region of the CEP, with the SHG being shown in (a), and as green in the merged image (c). The TPEF (rhodamine signal) is shown in (b), and is red on the merged image (c). The growth plate is present on this map, at the left side of these images, with the EP to the right. *N=1*

In Figure 4.17 there are a series of images of the VEP and CEP boundary with both the SHG (column 1) and TPEF (column 2) signal. These images have been merged (column 3) so that it can be more clearly seen where the signal is coming from, with SHG signal in green, and the TPEF (rhodamine dye) signal in red. Figure 4.17a is the centre of the EP in the coronal plane, and each row successively gets further away from the centre, until the last row (Figure 4.17d) is where the cartilage is more visibly fibrous, and indicates the AF. Regions captured in these images include the boney VEP (strong SHG signal, low TPEF), the mineralised CEP (low SHG, low TPEF), and the non-mineralised CEP (low SHG and high TPEF). Features that are identifiable include the cell lacunae in the mineralised regions, blood vessel insertion into mineralised CEP, and the change in collagen direction between the mineralised CEP and VEP.

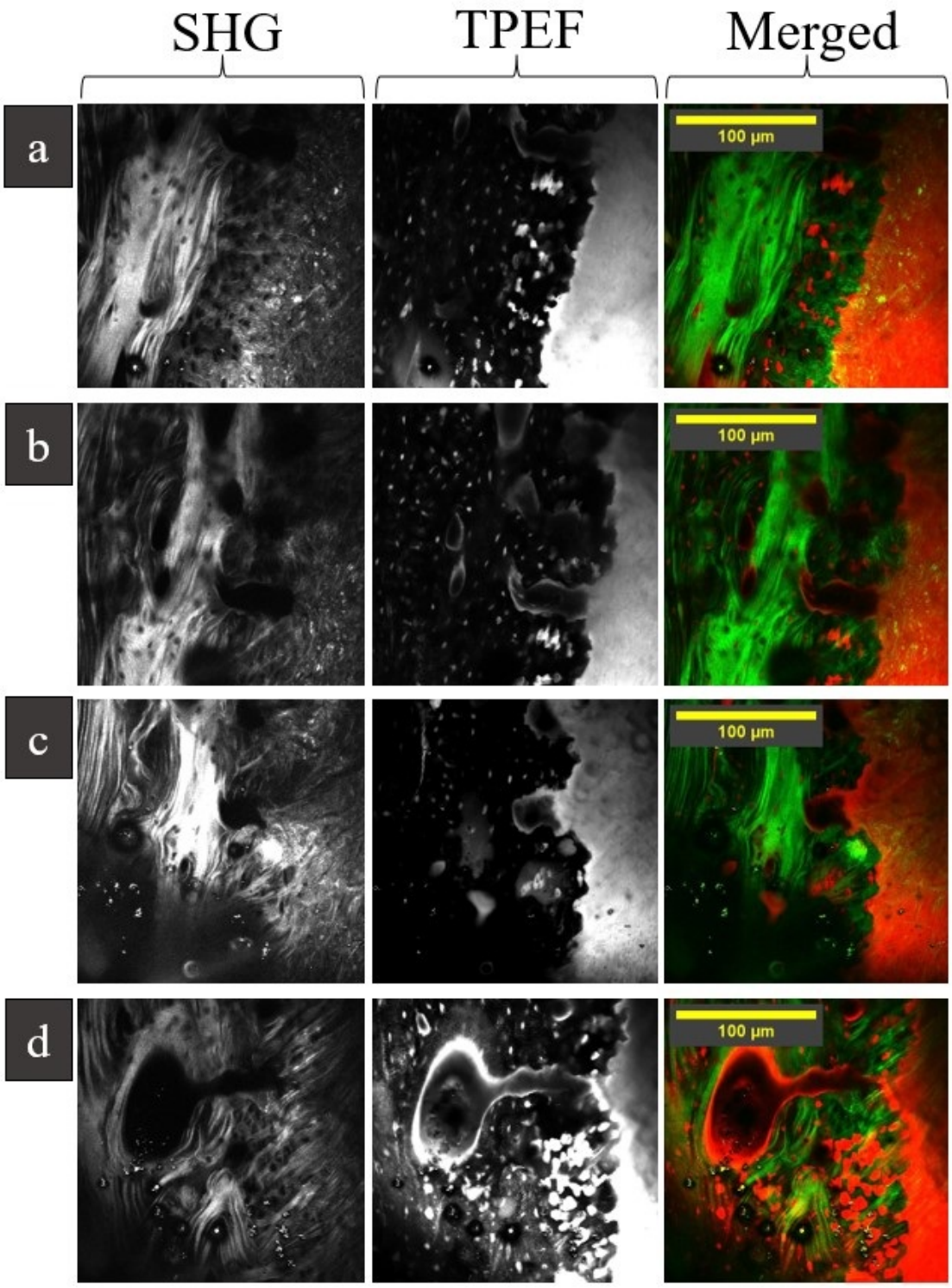

Figure 4.17: A selection of images showing the boundary between the VEP and CEP, with SHG (col. 1) showing the collagen, and TPEF (col. 2) showing the rhodamine staining. The merged images (col. 3) show both of these signals, with SHG in green, and TPEF in red. Each row is a different area, with (a) being at the centre of the coronal plane, and as the rows go down (b, c, and d), the images are showing increasingly more lateral regions, until the CEP becomes more fibrous adjacent to the AF in (d). *N=1*

4.3.3.2 Quantifying the 3D Collagen Organisation

Using pSHG the collagen orientation and dispersion can be quantified, and one set of results are shown in Figure 4.18. Figure 4.18a is the SHG signal which shows the boundary between the CEP and VEP by the change in intensity. In Figure 4.18b the I_2-$\Phi 2$ plot is shown overlayed with the same image in Figure 4.18a, where the colour is indicative of how ordered the collagen is (red being more ordered), and the direction of the overlayed lines indicate the principle orientation of the fibre. The histogram of I_2 values is shown on the bottom for both the CEP and VEP with each area masked separately. The VEP I_2 values are shown in blue and contain higher I_2 values over a broader peak, compared to the CEP which has a lower peak I_2 value and less variation. The peak I_2 values for the CEP and VEP are 0.08 and 0.15 respectively, and the FWHM values are 0.1266 for the CEP, and 0.3105 for the VEP. Within the CEP the collagen has a greater degree of dispersion near the non-mineralised region, but becomes more ordered closer to the VEP interface as the principle direction also changes. Across the interface, the bundles do not anchor directly between the two tissues, like in articular cartilage, but are instead orientated along the surface of the interface. Despite these two tissues having different collagen types, the collagen bundles have continuity in their orientation across this interface. The data of I_2 values shows marked differences between the two regions, as the CEP has consistently lower I_2 values, and therefore a higher degree of dispersion, which is expected in tissues consisting of the less fibrillar type II collagen. In the boney VEP, there are more ordered collagen bundles, but the range of dispersion levels is much greater than that of the CEP.

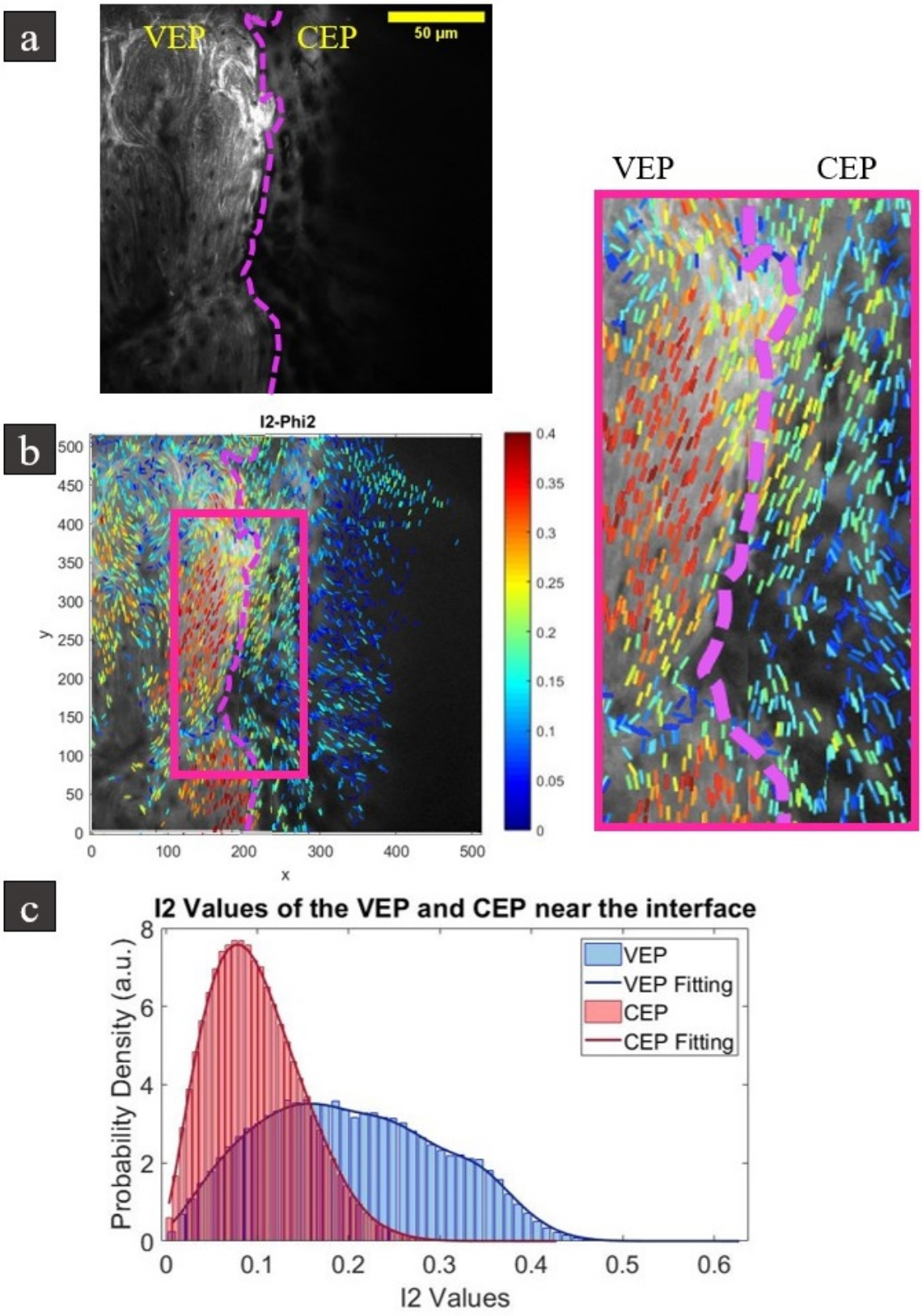

Figure 4.18: a) The averaged SHG image correlating to the results produced in (b) and (c), with a scalebar of 50 μm, and the boundary between VEP and CEP indicated by the purple dashed line. b) pSHG I2-Φ2 plot of the VEP and CEP interface, with the boundary shown by the purple dashed line. The plotted colour indicates the I2 value (degree of dispersion), and the direction of the lines represents the principle collagen direction. A closer view of the interface is shown in the pink box. c) The histogram plot of the two tissues shown in (a). The boney VEP is in blue, and the CEP is shown in red. *N=1*

4.4 Discussion of Results and Limitations

4.4.0.1 Confocal Laser Scanning Microscopy

The stained and embedded samples, when imaged with the confocal microscope, give information about the unmineralised regions in the tissue. Due to the small molecular size of rhodamine, this can enter the spaces as small as the canaliculi, as seen in the images in Figure 4.6.

The two soft tissues of the CEP and the growth plate are fully saturated with the dye, and so the boundaries are distinct in these images. The mineralised CEP adjacent to the saturated unmineralised CEP can be identified by the chondrocyte lacunae. These lacunae are more spherical in nature than the osteocyte lacunae, and do not have canaliculi attached. They are also larger than the osteocyte lacunae with an approximate width of 10-25 μm, compared to the osteocyte lacunae with dimensions ranging between 4-14 μm.

The large marrow channels characteristic of trabeculae bone can be seen in Figure 4.6 as an area with a high content of dye, but due to the porous nature of these structures it is not a continuous rhodamine signal. Blood vessels are smaller than marrow channels and can be followed throughout the stack. They are present in all osteon structures, as the central vessel in the Haversian canal, but are also present throughout non-osteon bone.

Limitations of this method result in features which are stained that are not part of the OLCN. These artefacts were due to dye leaking through a crack in the mineralised matrix, and were more common at the peripheries of the VEP, which is why there was a focus on the central region when imaging with the confocal microscope. These cracks are investigated by other methods and are discussed

in more detail later in this section.

4.4.0.2 Canaliculi Direction

When importing the 3D stacks into Synopsis SimpleWare, a 3D model can be viewed and rotated, to help visualise the continuity of the network direction, as seen in Figures 4.7. An observation seen in these irregular bones, is that the blood vessels and surrounding osteon-like structures change direction frequently, unlike in long bones where they are more consistent [319]. This means neighbouring mineralised regions of the VEP have different orientations of canaliculi, but within a small area, the canaliculi themselves have a high degree of order. This is seen in Figure 4.7, where a region of the bone has the majority of the canaliculi in the XY plane, and so appears as lines in the individual images, and less than 100 μm away, the canaliculi appear as dots, as their direction is primarily within the Z plane. In both of these cases, the canaliculi are aligned at approximately 90° to the nearest blood vessel, which is what is also observed in long bones. With this 3D data, the canaliculi can be seen to be ordered in both of these cases, with little observable variation in their dispersion, meaning that the principle direction is dominated by the blood vessel direction.

4.4.0.3 Canaliculi Density

To quantify features of interest in these samples from the confocal data, the signal in the images is needed to be grouped into particular features. The large blood vessels and cartilaginous tissue were segmented and masked using ScanIP and FIJI, leaving behind an image that only contains the lacunae and canaliculi, which could then be separated by the number of voxels in TINA. There were complica-

tions with this for quantifying the canalicular density, as the staining features that by eye do not appear like canaliculi, would be considered to be part of the canaliculi network by the code. For the final run through of TINA on the samples, the lines of dye were mostly masked out, but doing so meant masking out parts of the real network, and so the errors associated with the analysis in this part of the experiment are high. Each data set was plotted as a percentage of the distance from CEP to the growth plate for that sample, and the canaliculi density was plotted as a function of this in Figure 4.9. These values and large standard deviations are comparable to values of other studies using this method in human long bone [300], and so for these VEP samples the CaDn is comparable to the values in long bone. The standard deviation for this data is very large, with slightly greater deviations seen closer to the CEP. This data is from all data sets, which includes both intraosteon, and interosteon data.

The segmentation of osteons and interosteonal bone was carried out for tile scans which contained both, so that a comparison of the CaDn could be made between these two structures of bone. Figure 4.10 shows one of these data sets and shows that there is little variation between the two in terms of their CaDn (Figure 4.10c), even though the canaliculi orientation varies (Figure 4.10a and b). This particular data set indicates that the intraosteonal bone has a broader peak, and therefore has more variation, but with the errors incurred and the range of CaDn, this is not seen consistently in other data sets. From this, it can be concluded that the overall CaDn between the osteons and osteonal bone, is comparable.

Where the variation of CaDn does occur, it can be seen that the area of the lacunae domain also changes, as seen in Figure 4.8. With these plots, the visualisation of the cell lacunae as a Voronoi plot indicates the nearest neighbour, and

therefore the dark blue, the smaller the lacunae domain, and a higher lacuane density. The regions of higher lacunae density in Figure 4.8c coincide with the regions of higher CaDn in b.

4.4.1 Mineralisation

4.4.1.1 Backscattered Electron Imaging

The large scale map showing the BSE signal provides a visual depiction into how the mineral density varies throughout the sample. Since calcium is one of the highest atomic number atoms present in large quantities, the contrast of mineralised tissue is dependent on the amount of calcium present. From Figure 4.11a it can be seen that there are brighter regions of the EP, which do not span the entirety of the vertebral body, and is only located adjacent to the regions that would be the NP and inner AF. Given the hypermineralisation, and location of this feature, it correlates with how the mineralised EP has been observed in other studies [203, 290]. There is also extensive mineralisation at the growth plate, as well as a more unusual pattern of hypermineralised regions around the trabeculae. The growth plate having a high mineral density is expected, as it is a cartilaginous tissue that mineralises before remodelling of the tissue occurs, but the higher mineral density in the trabeculae region is going to be a product of remodelling on the bone and will either be points of higher stress, or recent trauma.

In Figures 4.11b and c, a closer view of the peripheral region and the central region is shown. In b, the marrow channels are smaller and the dominant structure of the bone is made up of osteons. These osteons are identifiable by their more densely mineralised cement line. There is no hypermineralised CEP, but the growthplate still exhibits a greater degree of mineralisation than the remodelled

bone. Figure 4.11c shows the central region, which was the focus of the samples in this chapter. In c the hypermineralisation of the CEP and its uneven mineral surface can be observed, along with the subchondral bone plate (SBP) made up of many osteons. In the trabecular bone, the marrow channels are larger than at the peripheries, and appear to have wider range of pixel intensities, and therefore calcium content.

By segmenting the areas in 4.11c into the mineralised CEP, SBP, and trabecular bone, their pixel intensities can be compared to quantify the difference. In Figure 4.12 the data shows that the mineralised CEP has both a higher peak value, as well as a broader peak, indicating a larger range of pixel values. Between the SBP and trabecular bone, there is little difference in the overall mineralisation except that the trabeculae has more heterogeneity in the mineralisation values, whereas the SBP is more consistent. Due to embedding issues, the fibres in the marrow channels in this sample are from the polishing disc, and since there were a few faults with embedding, it was thought that some of these bright regions in the bone might be artefacts, rather than high mineral deposits.

4.4.1.2 Energy Dispersive X-ray Spectroscopy

EDX data was taken to confirm the elemental composition in this region to assess whether the features in the BSE data are really minerals, contaminants, or image artefacts due to surface defects. The region analysed in Figure 4.13 contains four of the typically observed features, and whilst the pixel intensity does appear to correlate with the calcium content, as seen in Figure 4.14a, the change in the phosphorous content (Figure 4.14b) raises questions on the mineral crystal structure. Since the molecule on the crystal containing phosphorous is gradually

substituted out by carbonate molecules, the ratio of calcium and phosphorous (Figure 4.14c) is indicative of how recently the mineral was deposited. The purple region in this EDX data shows that these hypermineralised regions, thought to be artefacts, are actually regions of older mineral matrix. The biological significance of these are not hypothesised yet, and more work to study them would be complementary to the studies carried out in this chapter.

4.4.1.3 Limitations on Studying the Minerals

Limitations with BSE are sample preparation dependent. In some samples where the embedding material did not reach the marrow channels, there was a build up of fibres from the polishing cloth. Whilst this does not effect the data taken of the bone, the porous nature of these could be a source of contaminants and holding moisture, so extra care has to be taken to ensure the sample is fully dry before putting them into a vacuum for either the coating stage, or the imaging stage. When creating large maps with BSE it is important that the sample itself has the imaging side parallel to the attachment side, to minimise a change in intensity over large distances due to tilting of the sample. Whilst this can be corrected by the stigmator on the SEM, it is more efficient and reliable to make sure the polishing is done for longer. The EDX data is automatically quantified by the SEM, and is reliable within its own limitations. Since BSE relies on the atomic number of the elements, carbon was used as a conductive coating to ensure clearer BSE images. However, upon declaring the coating element and thickness, any carbon EDX data is omitted from the results to prevent skewed results from the coat. Since carbon is such a prominent element within biological tissues, this means that the wt % of all other elements are artificially high in the

EDX data, and therefore the raw data for wt % should not be used for precise quantification, but the ratios of minerals taken instead. The mineral to matrix ratio values by EDX would require a metal coating, which would compromise the BSE images.

4.4.2 Collagen

4.4.2.1 Macroscale Organisation and Channels

When looking at the collagen orientation, the images in this thesis support the wide literature on how the peripheries of the IVD are mostly type I bundles that anchor into the VEP directly, seen in Figure 4.16. It can also be seen how this collagen orientation changes towards the centre, where the bright SHG signal indicative of type I collagen in the VEP changes orientation by 90° at VEP region neighbouring the CEP, but with little observable integration of the fibres across this interface in Figure 4.15.

Single frames of the VEP and CEP boundary give more insight into how this change in anchoring gradually occurs. In Figure 4.17 the left column is the SHG, the middle is the TPEF, and the right column is the merge of these two signals. Figure 4.17a shows the centre of the sample, which is indicative of the VEP-CEP boundary adjacent to the NP of the IVD. In a, it can be seen that the type I bundles of the VEP run along this boundary, with minimal branching of these bundles and no observable insertions into the CEP. The CEP is the region which has a less intense SHG signal, but comprises of both the mineralised CEP (low SHG, low TPEF), and the unmineralised CEP (low SHG, high TPEF).

In Figure 4.17b, the VEP and CEP are stil distinguishable by their SHG signal, but the boundary is less clear as there appears to be some integration of the

fibres. What is also noticeable in this image, is a channel indicated by the channel wall being stained with rhodamine, and a lower SHG signal due to it being a cavity. This channel is interesting as the lack of an SHG signal stops at the tide mark, meaning the mineralised CEP has this vascularisation, but the unmineralised CEP is still avascular, like the IVD. This could be a supportive visualisation of other findings that have declared vessels that appear to terminate at the tide mark [290].

In Figure 4.17c, the boundary is further obscured by the entwined collagen fibres, with the CEP having a more prominent signal, even if the fibres themselves are less ordered than what is seen in the VEP. Figure 4.17c also contains a channel, with similar characteristics to the one in Figure 4.17b, where there appears to be a termination, or at the very least a sudden change in direction, at the tide mark between the mineralised CEP and the unmineralised CEP.

Figure 4.17d is where the CEP consists of larger collagen fibres that are strongly integrated into the VEP. Whilst the collagen boundary is more difficult to distinguish this far from the centre, the TPEF signal is useful in determining the cement line as the chondrocyte lacunae are much bigger than the lacunae of the osteocytes. This row also shows a channel that terminates at the tide mark, but also shows it crossing the boundary of the VEP and CEP, indicating that these are a continuation of a vessel in the bone.

Whether the vessel feature is a blood vessel or lymphatic is unknown. Previous work on lymphatics has shown that the lymphatics are not present in mineralised sections of boney tissue, due to the role of needing a fluid pressure in order to work efficiently, and they're not present in particular tissues, such as the IVD, in healthy cases [320, 321]. From other studies, it would appear more likely that

this is a vascular channel, stemming from the highly vascularised bone. If these are capillaries, the exchange of nutrients to the IVD would be more efficient and would support the work done by other research groups on the large scale porosity of the mineralsed CEP having an influence on IVD health. However, the morphological nature of the dead-end does not support the idea that this is a capillary, as the vascular system is a closed loop. This work, despite the apparent dead ends, is more supportive of the channels in the mineralised CEP being a vascular channel to the continuity from the VEP. Further work on precisely characterising these would be complementary to those researching this interface.

4.4.2.2 Dye leaking artefacts

With all samples, there appears to be some dye leakage into the mineral matrix, as mentioned in Section 4.3.1. These features were more prominent in the young, and at the peripheries of the sample, which is why the region above the NP was used. These features were difficult to mask out without removing significant amounts of the OLCN, and so older samples would be better to use for studies regarding how the OLCN changes across the VB in the transverse plane. A potential explanation for why these appear more in the young sample, is that they are undergoing rapid growth at that age, and so a lot of new bone is being laid down and would not have fully mineralised yet. Ayoubi's work shows that, due to how the mineral matrix grows (i.e. in small nucleation points), there would be gaps where this dye can leak into, and then stain the collagen in newly forming bone [70].

However, the BSE data does not correlate with this, as some areas imaged with these artefacts also have a higher degree of mineralisation. Whilst the spe-

cific plane might not be an exact match on the two images, due to the BSE being the surface of the sample, and confocal is just within, there are no obvious cracks visible on the BSE which would help explain why there is this leaking of dye.

With SHG and TPEF both the collagen and rhodamine signal can be seen, and the merged images of the regions of leaking can provide a more justifiable explanation. The leaking of dye shown in the TPEF signal in Figure 4.19b is in the same region as a collagen bundle beginning to branch in Figure 4.19a. There is a line of rhodamine signal that follows the direction of the collagen bundle, but corresponds to a lack of SHG signal in Figure 4.19c. This type of feature is likely to be microcracks in the mineral matrix, and so has no collagen (no SHG signal), and is filled with rhodamine (high TPEF signal). Whether these are due to sample preparation techniques, or naturally occur in the growing bone, is undetermined by these experiments.

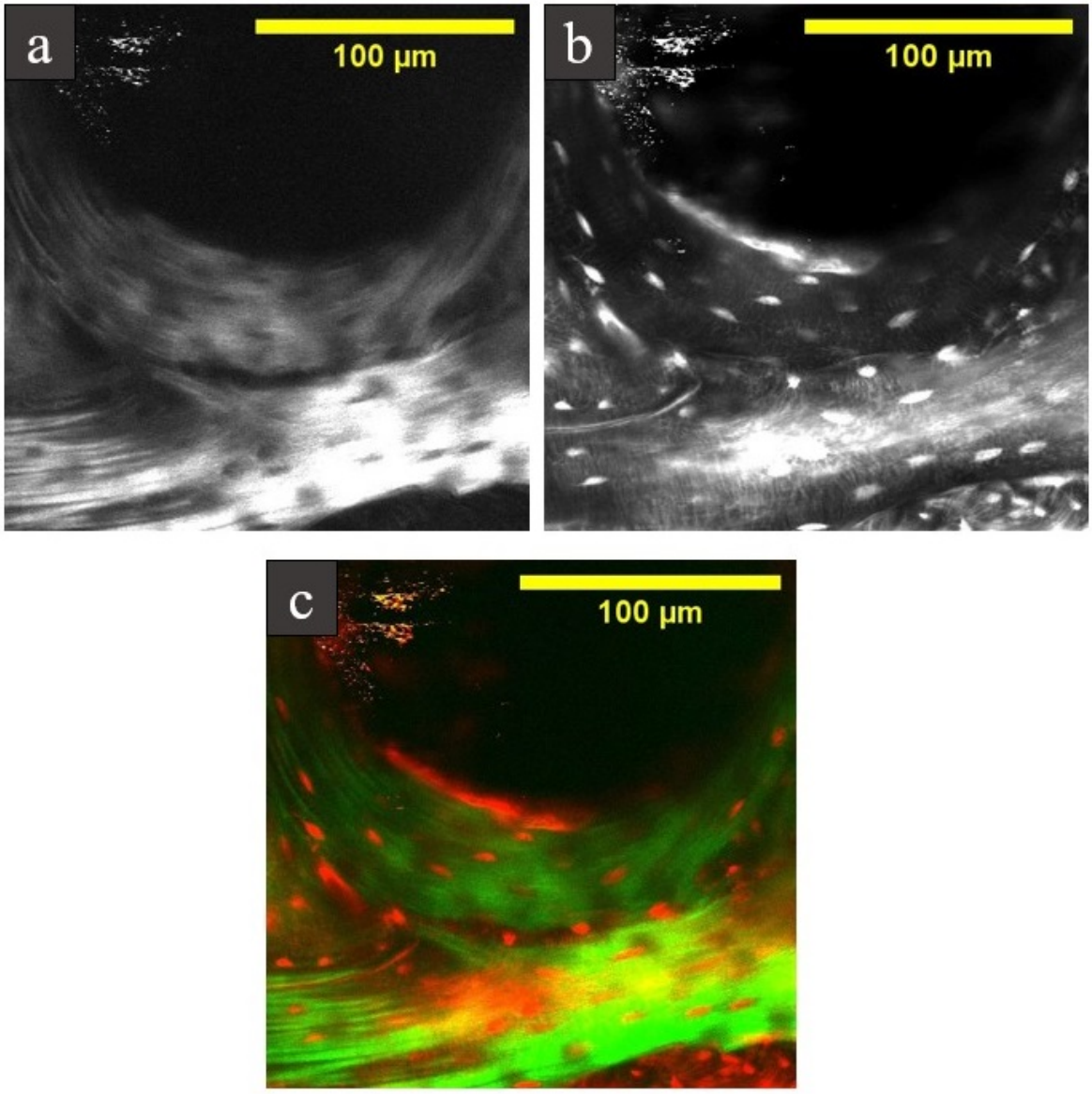

Figure 4.19: An image showing a collagen bundle + staining along bundle boundary. In (a) the SHG signal is shown, which represents the collagen fibres. b) The corresponding TPEF shows where the rhodamine dye is present. c) The merged image shows the spatial correlation between these two signals, and is yellow where the signal overlaps. The branching of collagen corresponds to where a dye artefact is present. *N=1*

4.4.2.3 Quantification of the collagen

The pSHG data shows how the collagen is organised at the CEP and VEP interface, which has previously not been explored by such methods. The data shows that across the interface, the collagen type changes, but the orientation of these bundles is consistent. Whilst there is a change in dispersion of collagen from the CEP to VEP, the local area around the interface does not exhibit a sharp change,

meaning that despite the collagen not anchoring between the two tissues, there is still continuity in the collagen arrangement. The spread of dispersion values for the VEP is much higher compared to the CEP, as evidenced by the histograms in Figure 4.18. The low I_2 values in the VEP can be seen in the very top left corner of the SHG images, where the collagen is changing direction in a circular pattern but from the SHG values it is unclear whether this surrounds a blood vessel or not. At the bottom left corner there is change in the collagen arrangement which also results in low I_2 levels. An increase in the collagen degree of dispersion in regions with changing direction would minimise the effective fault lines within the VEP and is likely a feature which aids in distributing loads throughout the tissue. Computational modelling on the effects of the dispersion of the collagen at these features in the VEP would quantify how this changes the tissues mechanical properties.

On this data set there are small areas where the orientation of the collagen bundles from the CEP look like they could be inserting at a low angles. Mechanically, collagen insertions have been beneficial for cartilage and bone interfaces, such as articular joints and calvarial sutures. If the load is dissipated in this region only by the rigid mineral matrix, it would explain why there is an increased fracture risk in this area.

Biochemically type I and II collagen can bond together [322], and so it would be interesting further work to assess how the fibrils at this interface interact at small scales. Whilst such small features are beyond the resolution of the MPM, other methods, such as small angle x-ray scattering (SAXS), could be viable to answer such questions.

4.5 Summaries and Future Work

This chapter has investigated the mineralised tissue of the CEP and VEP via three different imaging modalities. The research question addressing how the OLCN in irregular bones compares to that of long bones is answered by the following conlusions: The CLSM data shows that the VEP has the same structure as other bones in the body, and the values for the canalicular density are comparable to studies of long bones in other large mammals, indicating that this technique is valuable to answer outstanding questions on human bone structure. The VEP appears to vary from long bone by the heterogeneity in the canaliculi and collagen directions, which could be down to the multiaxial loading environment of the spine. The CaDn values between the osteon and interosteon bone do not vary significantly.

To answer the question of how the minerals are distributed between the two soft hard interfaces of the EP and growth plate BSE imaging was used and shows that there are variations of mineralisation within the VEP with higher concentrations in the central region and around the marrow channels. The mineralised CEP and boney regions around the growth plate have a higher degree of mineralisation than that of the VEP. Upon remodelling within the VEP, the mineral density is higher at the edges of the marrow channels. Relative rates of remodelling are compared by the ratio of phosphorous to calcium, and there is evidence that small hypermineralised regions are present which exhibit slower remodelling times than the other areas of the VEP.

For the collagen, these experiments answered how the change from type II to type I occurs across the EP, and how the direction and dispersion of these collagen fibres vary across this interface. Maps of the VEP have shown the large

scale differences in the type I collagen bundle orientation from the peripheries and the central location using multiphoton microscopy. The appearance of the porous mineralised CEP can be visualised by this method with the stained and embedded samples, and it can be seen that these channels stop abruptly at the CEP tide mark interface, between the mineralised CEP and the non-mineralised CEP. The pSHG used a fresh spine sample due to limitations of the scanning time, and analysis was carried out to quantify the level of disperion in the collagen at the CEP-VEP interface. The pSHG data shows that the collagen bundles, both type I and II, are aligned along the interface, with the only feasible insertions being at low degrees. Dispersion of collagen bundles within the VEP increases as the large bundles visible by SHG change direction, and branching of these collagen bundles coincides with a gap in the mineral matrix.

4.5.1 Further Studies

The studies in this chapter could be expanded by all three modalities, and a quantified correlation between the modalities can be achieved on the basis of what has been covered in this chapter.

- The spatial correlation between the imaging modes is seen in Figure 4.20, where the same region of trabecular bone in the VEP is shown by its OLCN and soft tissue (Figure 4.20a), the collagen (Figure 4.20b) and mineral (Figure 4.20c). The qualitative changes assessed by all three methods (CaDn, collagen dispersion, and degree of mineralisation), explained within this chapter can be applied to the same location. The samples prepared in this way can then have a quantified spatial correlation between the OLCN, collagen direction and dispersion, and degree of mineralisation.

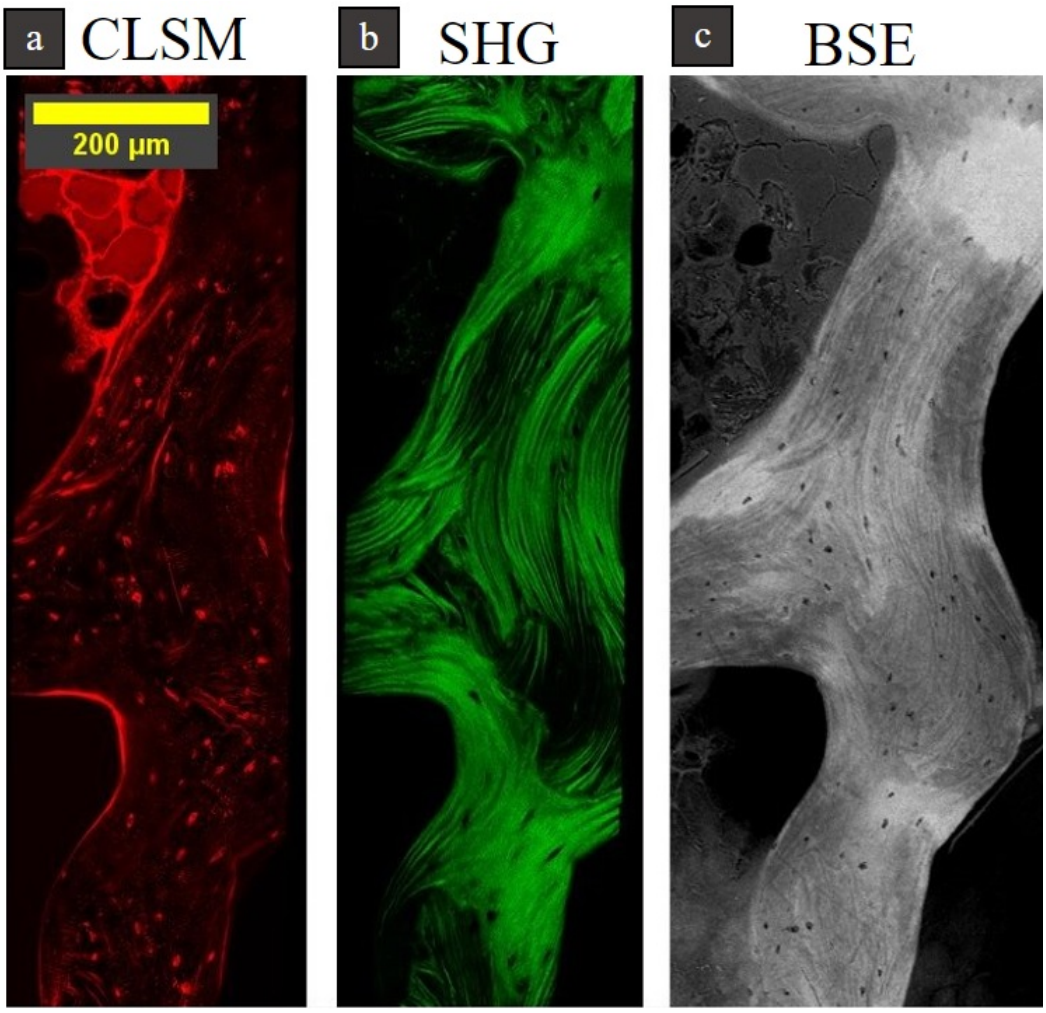

Figure 4.20: Example of combining the three imaging modalities. a) CLSM image for trabeculae in the VEP, showing the lacunae, marrow and canaliculi. b) SHG signal for the same region showing the collagen bundles. c) BSE image showing the mineralisation for the trabeculae. *N=1*

- Studies of the OLCN could use different spine segments to assess how the canaliculi density and the heterogeneity of the network varies across different VEPs of the spine, and whether there is a difference between the cranial or caudal VEP.

- For work on the mineralisation, accurate quantification of the calcium weight % can be obtained via Quantitative Backscattered Electron Imaging with the use of reference materials and it would be interesting to study these values across both healthy spines like the ones imaged in this chapter, and compare them to spine segments that have degenerated due to age or disease.

- The collagen orientation and dispersion can further be expanded by similar extensions outlined for the OLCN and mineralisation, by assessing if these quantified values change with age and disease, and if these changes increase the risk to the tissue.

Chapter 5

Spatial Gradients of Collagen Organisation and Mineralisation in Flat Bones at Calvarial Sutures

5.1 Introduction

The cranial sutures are the fibrous soft tissue between the ossified cranial plates which make up the the calvarial region of the skull, and these interfaces between the mineralised and non-mineralised tissue are the primary site of where cranial growth occurs [323–325]. As the skull grows, it is important that there is both the ability to expand with growth, and protect the intracranial cavity. The role of the sutures is to both allow growth of the cranial plates by providing the osteogenic front, and to dissipate stresses under various loading environments with the viscoelastic properties of fibrous soft tissue, which is not exhibited to the same extent in mineralised tissues [326]. As the brain grows, there is pressure on the cranial plates to move outwards to accommodate this growth. The stresses experienced

by both internal and external forces stimulate growth, and the interdigitation of the suture which aids in distribution of the loads [326]. Starting from two years old, the sutures begin to ossify, and are considered fused when the suture is completely mineralised. This fusing occurs after skeletal maturity and can still be occurring up to 60 years old in some people [327–329]. In patients where one or more of these sutures fuse prematurely there is abnormal skull growth arising from the inability of the cranial plates to grow from the fused suture. This causes a flat shape at the affected suture, and bulging at the other regions of the skull due to uneven stress distribution and can lead to health complications, described in Chapter 2 [264, 323]. The health implications of abnormal mineralisation at this interface are well documented, as well as the genetic mutations that are a common cause, as summarised in Chapter 2 [264, 330].

However, despite the role that the sutures have in skeletal development, the mineral density organisation and collagen arrangement across this soft-hard interface has yet to be quantified in a way which would provide insight into a clinical solution to repair abnormalities and enhancing surgical outcomes.

The four regions of interest within the skull are the sagittal, squamous, interfrontal, and coronal sutures and their surrounding mineralised tissue. The newly laid down bone surrounding the sutures is known as sutural bone, whereas within the centre of the cranial plates it is non-sutural. On a smaller length scale, there is both woven and lamellar bone present, differentiated by the macroscale collagen organisation visible with the SEM [100]. Understanding the spatial gradients of the minerals across these differently formed interfaces of mechanically dissimilar tissues, and how they compare to other mineralising interfaces explored in this thesis is a key consideration for developing future therapies or preventative treat-

ments for such ailments. It is known that the calvaria contains densely woven bone at the site of growth, but how this bone mineral density changes at both mm and μm length scales, and whether these patterns are changed during disease would provide valuable insight into how more specialised treatments can be developed. The collagens of both the suture and the calvaria have been qualitatively described [331, 332], but how the degree of dispersion of the collagen bundles changes at the interfaces between the non-mineralised suture, woven bone, and lamellar bone are yet to be investigated.

Imaging the minerals and collagen require different methods due to the differences in their chemical and physical nature. Collagen can be imaged by a variety of methods including histology staining, scanning electron microscopy (SEM), and polarised second harmonic generation (pSHG) [87, 126, 221, 268, 274–276, 303, 333, 334]. In histology the use of trichome staining on thin sections is an established method for imaging collagen, and in SEM the secondary emission signal can be used to image the collagen fibres at the surface [333]. PSHG can be used on thick samples, both fresh and processed for SEM, and can use different polarisation angles to get the degree of alignment and dispersion of collagen bundles.

Minerals can be investigated by computerised tomography (CT), SEM, small angle x-ray scattering (SAXS) and wide angle x-ray diffraction (WAXD) [67, 262, 331, 335–340]. CT scans provide a 3D scan of the structure with the porosity of the tissue being visualised, whereas SEM in the back scattered mode captures the bone mineral density (BMD) in a 2D image, and SAXS and WAXD can assess size, shape, and orientation of the nanoscale crystals.

The quantification of the collagen dispersion and distribution of bone mineral

density at the flat bone neighbouring the suture require multiple modalities which can achieve μm resolution across mm length scales, which is why the two modalities chosen are scanning electron microscopy and multiphoton microscopy.

The specific research questions addressed in this chapter are:

- How are the minerals in the cranial plates spatially distributed, and is there a dependency of the degree of mineralisation on the distance from a growth site?
- How does the collagen type, principle direction, and dispersion change across the calvarial suture, and do these changes correspond to a change in the degree of mineralisation?
- Does the degree of mineralisation between the two bone types of lamellar and woven change in these mouse skull models?

The following experiments look into the mineral density of mouse skulls by using QBEI (quantitative back scattered electron imaging) to assess the spatial distribution of the degree of mineralisation around the sutures where intramembranous bone growth occurs. With the use of pSHG the collagen dispersion and principle direction have been quantified for the significant regions around this interface, with the interface itself being identified by the TPEF signal showing the boundary between unmineralised sutures, and the mineralised cranial plates.

5.2 Methods

5.2.1 Sample Preparation

Following a similar protocol as described in Chapter 4, three mouse skulls (C57BL 6J at 28 weeks old) were dissected, dehydrated, stained, and embedded with the cold PMMA method, but with adjusted time scales to accommodate the smaller sample size compared to Chapter 4. A brief outline is in table 5.1.

Table 5.1: Table of Cold PMMA method for mice skulls

Step	Conditions	Time
Dehydration 1	70% Ethanol, 4°C, 10min under vacuum	2 days
Dehydration 2	80% Ethanol, 4°C, 10min under vacuum	2 days
Dehydration 3	96% Ethanol, 4°C, 10min under vacuum	2 days
Dehydration 4	100% Ethanol, 4°C, 10min under vacuum	3 days
Staining 1	$8.7\text{x}10^{-3}$M rhodamine, 4°C, 10min under vacuum	1.5 days
Staining 2	$8.7\text{x}10^{-3}$M rhodamine, 4°C, 10min under vacuum	1.5 days
Xylene rinse 1	Xylene, RT, 10min under vacuum	3 hours
Xylene rinse 2	Xylene, RT, 10min under vacuum	3 hours
Preinfiltration	Pre-infiltration solution, 10min under vacuum	3 days
Preinfiltration	Infiltration solution, 10min under vacuum	3 days
Infiltration	Infiltration, 10min under vacuum	4 days
Embedding	Embedding PMMA mixture, -20°C, 10min under vacuum	3-4 days

These samples were cut by the diamond saw in the coronal plane to expose the interfrontal suture and coronal sutures on one skull, and the sagittal suture and squamous on the other two skulls.

After exposing the imaging plane the samples were re-embedded in Struers epoxy, with a ratio of 15:1 resin:hardener in the Struers $31.75\ mm$ diameter silicone molds, with reference materials such as Carbon (C), Magnesium Flouride (MgF_2), and Aluminium (Al), as seen in Figure 5.1a. After curing at room temperature in the fume hood for 4 days, they were repolished with the conditions in Table 5.2, to give a flat sample with the reference materials in the same plane [336], that is seen in Figure 5.2, and is seen in step b in Figure 5.1

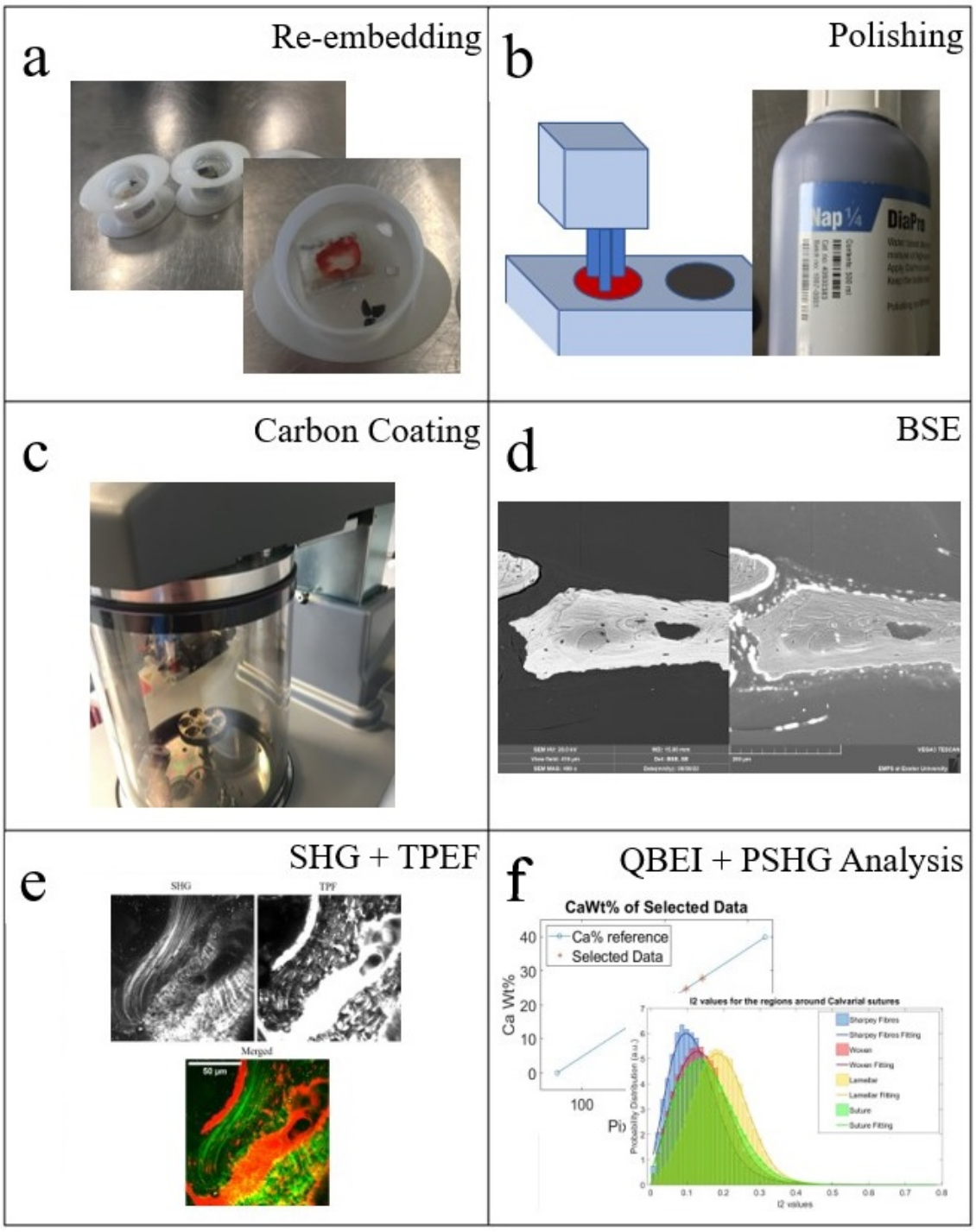

Figure 5.1: Sample preparation steps covered in this chapter. a) Re-embedding procedure to include the reference materials. b) Polishing to ensure a smooth surface. c) Sputtercoating of the samples with carbon. d) BSE image acquisition. e) SHG and TPEF acquisition. f) Analysing the images using the QBEI and pSHG codes.

Table 5.2: Grinding and polishing conditions for the embedded skulls

Step	Name	Mat used	Lubricant	Approx. Time
1	Grinding 1	#800	Water	20 minutes
2	Grinding 2	#1200	Water	2 hours
3	Grinding 3	#2400	Water	3 hours
4	Polishing 1	MD Sat	DiaPro 6 μm	4 hours
5	Polishing 2	MD Dac	DiaPro 3 μm	4 hours
4	Polishing 3	MD Nap	DiaPro 1 μm	4 hours
5	Polishing 4	MD Nap	DiaPro 0.25 μm	4 hours

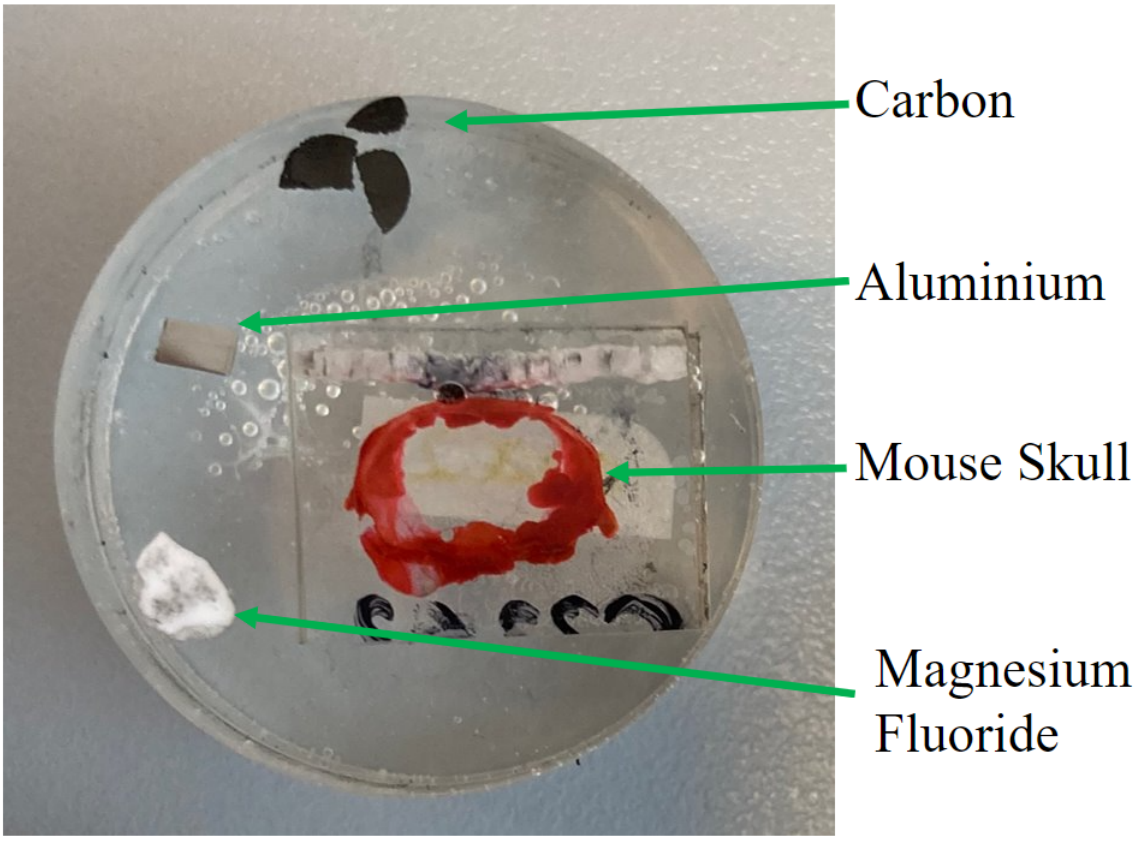

Figure 5.2: The re-embedded mouse skull with reference materials.

The samples were then coated with carbon using the Quorum Q150T ES Plus in Figure 5.1c, with the setting, 'pulsed rod evaporation' with a final thickness

between 30 and 50 nm, with the precise value given at the end of the sputtering process.

5.2.2 BSE and QBEI Analysis

The embedded, polished, and coated skulls were imaged using the back scattered mode of the Tescan VEGA3 SEM at the sutures neighbouring woven and lamellar bone with the imaging conditions outlined in table 5.3.

The BSE tiles are stitched together using the FIJI Plugin Stith function [341, 342] to get a global assessment of how the pixel intensity, and therefore the atomic density, of the sample varies on the length scales of mm. The BSE acquisition is step d in Figure 5.1.

Table 5.3: Table of imaging conditions when acquiring BSE data.

Condition	Value
HV	2 kV
Mag	499x
FOV	416 μm
Speed	8 (320 μs/pxl)
WD	15 mm
Contrast	$\simeq$55%
Brightness	$\simeq$90%
Beam intensity	10 (a.u.)
Absorption current	$\simeq$80 pA
Spot size	180 nm

Analysis via QBEI relies on the linear relationship between the pixel intensity, and the average atomic nuclear charge of the material being imaged [336, 343–345]. For this, standard materials were embedded alongside the mouse skulls and were Carbon (C), Magnesium Flouride (MgF_2), and Aluminium (Al). After focusing on the bone and getting the optimal contrast for seeing the different intensities on the same section of bone (Figure 5.3a), images were taken in the same session, with the same settings of the standard materials (Figure 5.3b). For the magnification used in this study, the references materials were not within the same field of view as the bone.

After converting the images into 8-bit, the maximum intensity of the pixels is 255, and minimum 0. With the average atomic number of the standard materials known, an average pixel intensity was obtained by selecting a multiple regions in the images (Figure 5.3c), and plotting mean atomic mass (Z_{mean}) as a function of the average intensities (Figure 5.3d).

Using the polyfit function with an order of 1, the linear equation linking the average atomic mass and the pixel intensity can be obtained for that sample [346]. The Z_{mean} for hydroxyapatite is calculated from its chemical structure by the equation 5.1,

$$Z_{mean} = \frac{\sum(N_i * A_i * Z_i)}{\sum(N_i *_A i)} \tag{5.1}$$

to give an average atomic number of 14.06, and with the linear equation derived from the reference materials, the theoretical pixel intensity value for pure hydroxyapatite is obtained (Figure 5.3e).

Since pure hydroxyapatite is known to have a Calcium weight % (CaWt%) of 39.68% [336, 347], the theoretical value of the hydroxyapatite pixel intensity, and

this CaWt% can be plotted with the second point being the 0% value of CaWt% and the intensity of the neighbouring osteoid material, to produce a new linear graph and equation which links the CaWt% to the pixel intensity for that sample (Figure 5.3f).

This analysis was done in Matlab and was used for both specific points in an image, as well as larger areas of analysis from masked BSE slices. A script was developed which imports a specific image, where the user can select multiple points on the image, and then plots the pixel intensity and CaWt% for that sample. This script was used for quickly comparing individual pixels from different areas, but using the FIJI function 'Plot Profile' from a line, the data is then exported, which the QBEI code imports and can plot in the same method as depicted in Figure 5.3. For larger areas of bone, and for comparing woven and lamellar bone, masks have been created for the BSE image and the same quantification of pixel intensity to CaWt% has been used by taking the average of the area.

When plotting the histograms of CaWt% in Matlab, the peaks were found by the Matlab spline interpolation and findpeaks functions [346].

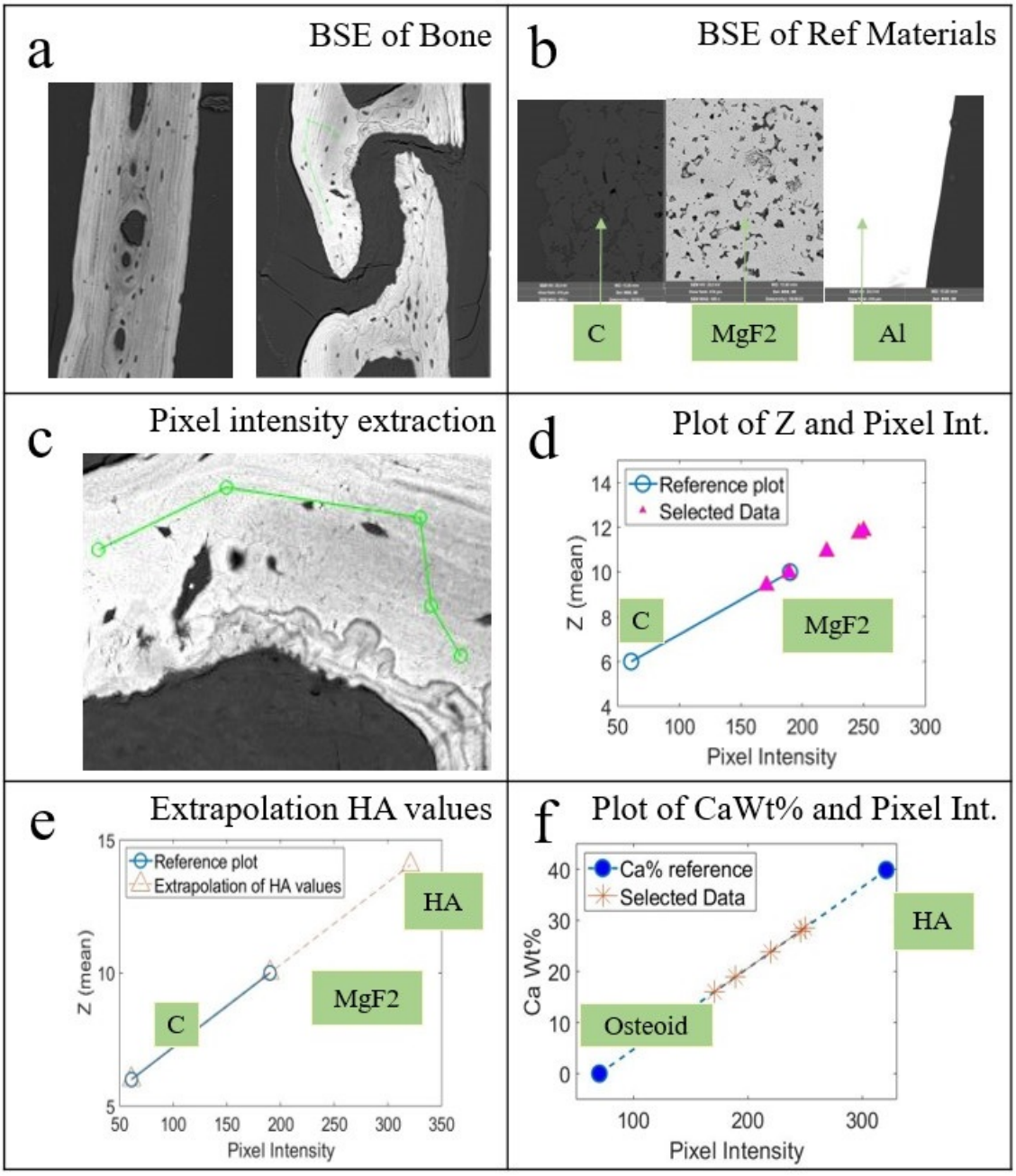

Figure 5.3: a) BSE acquisition of the sections of bone which are of interest. b) With the same scan, the reference materials of Carbon (C), Magnesium Flouride (M_gF_2), and Aluminium (Al) are obtained. c) Importing the images into matlab to extract the pixel intensities, with an example of a selected few points in green for the bone (right) and the C and M_gF_2 reference materials on the right. d) Plot of the average atomic number as a function of pixel intensity, with the two reference points in blue (C and M_gF_2), and the 5 selected points from (c) in pink. e) The linear plot of C and M_gF_2 (blue) extrapolated to get the pixel intensity of pure hydroxyapatite (HA) (orange triangle). f) Using the pixel values of HA and the osteoid and the CaWt% of 39.68% and 0% respectively, a new plot and linear equation is generated (blue), with the 5 selected points from (c) in orange asterisks.

5.2.3 Multiphoton Microscopy

Images of a sample were taken with the multiphoton microscope to obtain SHG + TPEF images, and scanned through the polarisation angles to obtain pSHG data that can help identify the collagen arrangement, with the theory outlined in Chapter 3. Briefly, the polarisation sensitivity of the SHG signal produces a series of images which has each pixel varying in intensity to fit a cosine function, and properties of this fitting are used to obtain the degree of dispersion (I_2) of the collagen fibres at that point, as well as the principle direction (ϕ_2) with the equations described in Chapter 3.

The TPEF signal shows where the rhodamine staining has occurred, and therefore shows where the soft tissue is present. This allows for the interface of the mineralised tissue and the unmineralised sutures to be located on the multiphoton images. The settings for acquiring these images with the multiphoton microscope is outlined in table 5.4.

Table 5.4: Conditions for the multiphoton microscope when imaging the skulls, under the conditions for single image acquisition and pSHG.

Condition	Single Images	pSHG
Lens	25x water	25x water
NA	1.05	1.05
Zoom	2	3
Frame size	512x512	512x512
Pixel bin factor	40	20
Frame average	3	1
Angle of waveplate	13-18 °	13-18 °
Gain	700	700
Input voltage	-10:10	-10:10

5.2.4 Distinguishing the Regions of Interest to Image

This combined method allows for comparison at different length scales, with a mapping of one sample being carried out to compare how the bone mineral density changes from one suture, through the cranial plate, the other suture. On a smaller scale, the mineral distribution from the interior to exterior surface of the cranial plate is assessed, as well as how it changes with distance from the nearest growth site in the 4 sutures of interest: Sagittal, Squamous, Interfrontal, and Coronal. At the microscale a focus on the recently ossified tissue is carried out, with a bone mineral density comparison between the woven bone structure and lamellae structure around each of the 4 sutures. The use of multiphoton microscopy has been carried out for one sample and one suture (Sagittal), and compares the

collagen dispersion and organisation in the mineralised regions of the woven and lamellar bone, as well as the Sharpey's fibres and the fibrous suture.

The regions for analysis are differentiated by the features seen in both imaging techniques. The non sutural bone has channels for a blood vessel, and the sutural bone is closer to the non-mineralised suture. In the BSE images the distinction between the mineralised and non-mineralised tissue is indicated by the pixel intensity, with mineralised showing a brighter pixel. For the mineralised tissues making up lamellar and woven bone, the lamellar bone is identifiable from macroscale collagen bundles which are visible as a change in surface texture in the secondary emission images, as well as BSE, whereas the woven bone collagen structure lack these characteristic bundles and so appear smoother in both image modes on the SEM.

The non-mineralised regions are stained by the rhodamine and will therefore have a high intensity signal in the TPEF image when using the multiphoton microscope. Meanwhile, the channel detecting SHG provides an image to distinguish the woven and lamellar bone, as the organised bundling in lamellar bone is a feature with a strong SHG intensity, whereas the woven bone and sutures produces less overall signal. The distinction between the woven bone, lamellar bone, and sutural tissue can therefore be seen by superimposing the two signals from the multiphoton microscope.

5.3 Results

5.3.1 Mineralisation Distributions

The raw BSE map of the parietal bone is shown in Figure 5.4a. The sutures are the sagittal (top) and squamous (left) in Figure 5.4a and b. The conversion of the raw pixel intensities into bone mineral density (BMD) values produces the heat map data of Figure 5.4b, where yellow indicates a higher bone mineral density and blue is lower. The range of bone mineral density spans from 5.2% to 30.5%, with the low values being attributed to the osteocyte lacunae and cement lines, and 87% of values for the parietal bone being above 15% bone mineral density, and higher values at the sutures where the percentages of data points above 15% CaWt are 95% and 93% for the sagittal and squamous sutural bones respectively. Figure 5.4c and d show the heat map of the sutures in higher detail than in b, where the lower values can be seen to correspond with the lacunae and cracks. Figure 5.4e shows the spread of bone mineral density for the regions in c, and d, as well as the interfrontal and coronal sutures. The squamous sutural bone has a peak at and 18.54%, and the sagittal sutural bone has a bimodal distribution with peaks at 22.56% and 25.31%. The sagittal sutural bone has a broader range of values than the squamous, indicated by the bimodal nature and a FWHM value of 9.08, compared to 6.09 of the squamous. For the other sample, the interfrontal and coronal sutural bone have peaks of 19.68% and 17.72% respectively. The interfrontal and coronal sutural bone has a narrower spread of values compared to the sagittal and squamous in the parietal bone, with FWHM of 4.14 for the interfrontal, and 3.48 for the coronal.

At this scale both the sutural bone (regions neighbouring the sutures in top

right and bottom left corners of Figure 5.4a and b) and non-sutural bone (top left corner of Figure 5.4a and b) can be seen. On this map there is no obvious visual pattern of there being a large change in the degree of mineralisation from the suture to the centre of the flat bone, but there does appear to be higher mineral density at the interior and exterior surface of the bone, which is seen throughout all samples. The sagittal sutural bone has a higher degree of mineralisation (22.66%) than that of the other three sutures, but also contains a wider spread of values and is, therefore, less homogenous in its mineralisation. The interfrontal sutural bone with a peak at 20.16% has the next highest degree of mineralisation, followed by the squamous and coronal sutural bones with similar peak values.

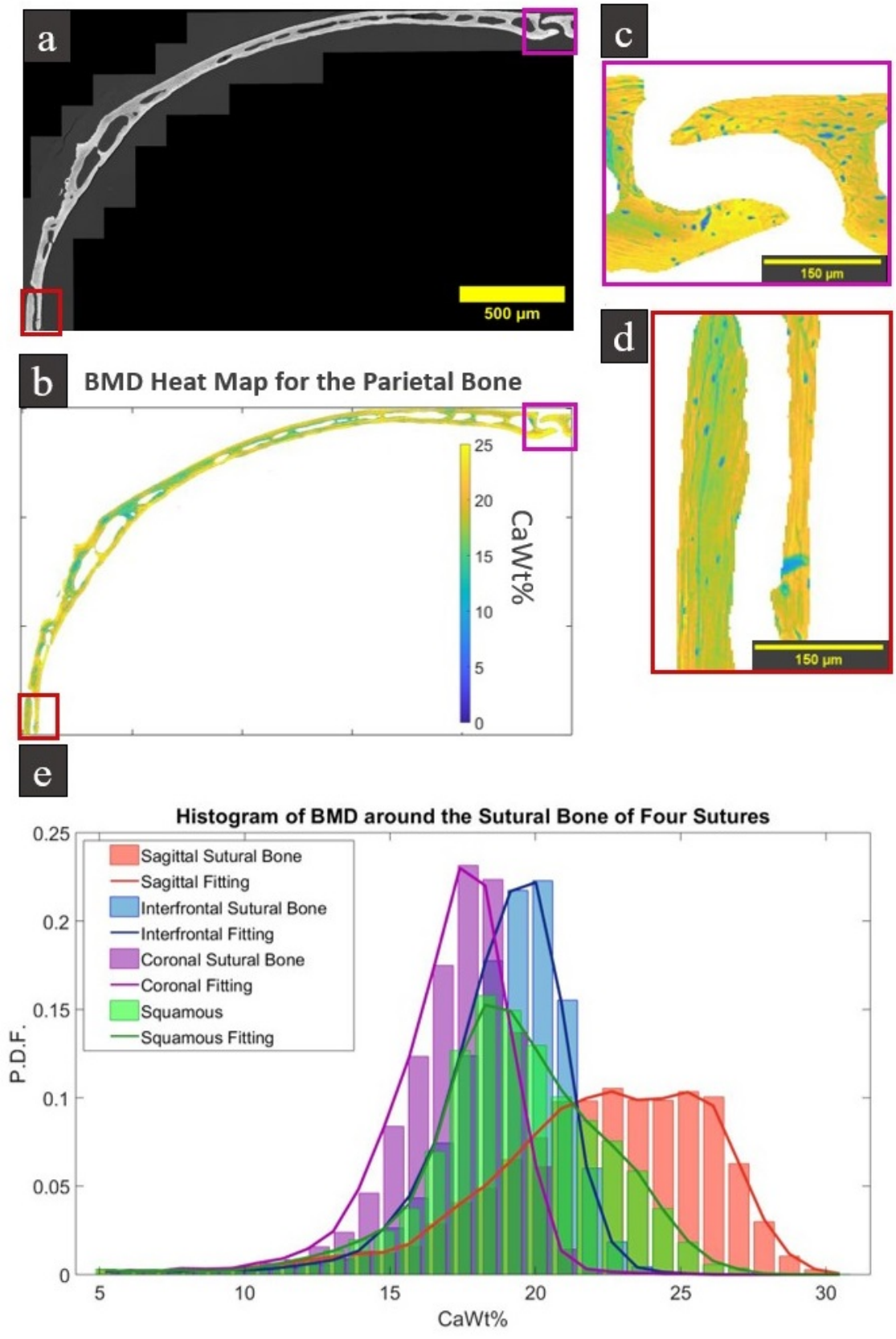

Figure 5.4: a) The BSE map of the parietal cranial plate from the sagital suture (top) to the squamous (left). b) A heat map of the BMD for the BSE map in (a). c) and d) show the heat map results of the sutural bone around the sagittal and squamous suture respectively. e) Histograms of the BMD for the sutural bone around the four different types of suture. *N=2*

5.3.1.1 CaWt% as a function of distance from sites of growth

The CaWt% has been plotted as a function of distance from a growth site for the parietal cranial plate, and the frontal plate, in Figures 5.5 and 5.7 respectively. Figure 5.5 shows the scatter plot of the CaWt% values, with the fitting showing a decrease in the CaWt% value the further away from a growth site. The gradients of the fittings are -0.05, -0.08, and -0.12 for the non-sutural bone, sagittal surrounding bone, and squamous surrounding bone respectively. From this data, the range of average CaWt% values changes for each location, with the non-sutural bone having the lowest degrees of mineralisation (13.23% to 15.55%), followed by the squamous data (16.5% to 20.72%) and the sagittal suture having the highest (19.61% to 23.16%). Figure 5.6a shows the masked BSE images used for the quantification in Figure 5.5, with scale bars of 150 μm. Figure 5.6b is a heat map of the pixel intensities of the raw BSE data, to visually show the spatial distribution of the range of CaWt% values. Blue represents lower pixel intensities, and therefore lower CaWt%, and yellow indicates higher.

Sample 2 is used to compare the interfrontal and coronal sutures, and the scatter plot of CaWt% values around these sutures is shown in Figure 5.7. Similar to sample 1, there is a decrease in bone mineral density further from the growth sites indicated by the negative gradients, but the gradients are not as steep, with values of -0.0046 and -0.019 for the interfrontal and the coronal data sets respectively. The fitted values of CaWt% range from 18.03% to 18.3% for the interfrontal data, and from 16.27% to 16.68% for the coronal. Figure 5.8a shows the BSE data used for Figure 5.7 with the applied mask, and Figure 5.8b is the heat map to show the spatial distribution of the high and low pixel intensities.

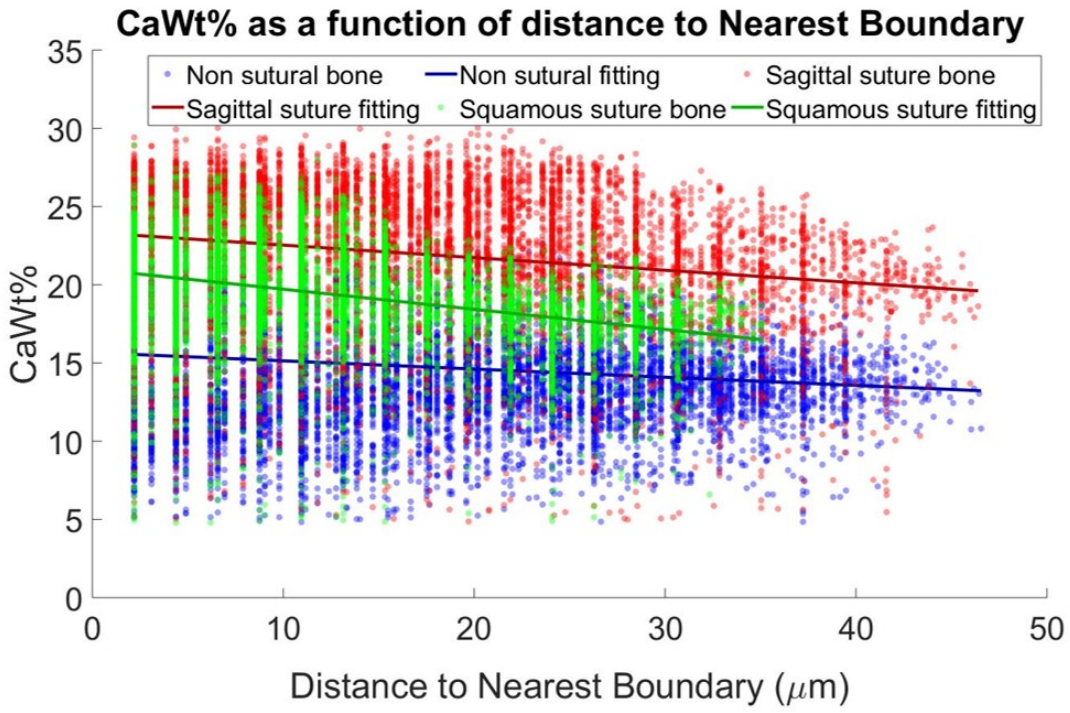

Figure 5.5: Results from sample one with the CaWt% as a function of distance from the nearest growth site. The blue data is taken from the centre of the parietal bone. The bone from around the sagittal suture is shown in red, and the bone around the squamous suture is in green. *N=1*

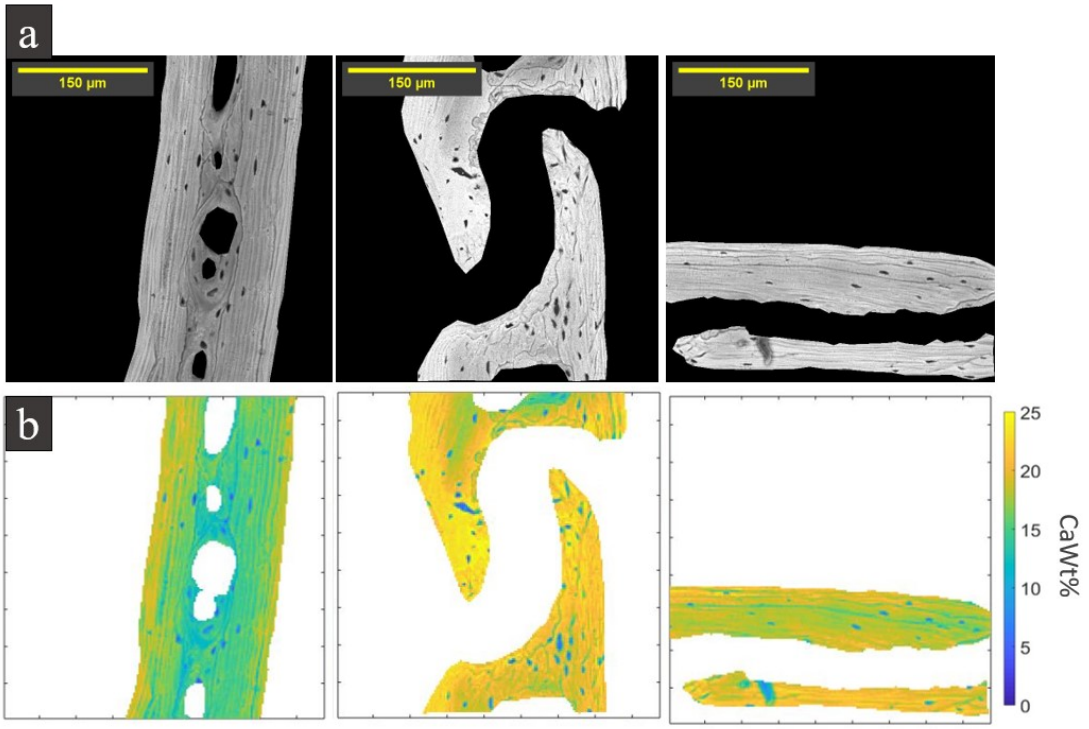

Figure 5.6: a) The masked BSE images for the nearest neighbour data seen in Figure 5.5. b) The heat map of BMD in the analysed regions in (a), where yellow indicates higher BMD, and darker blue is less mineralised. *N=1*

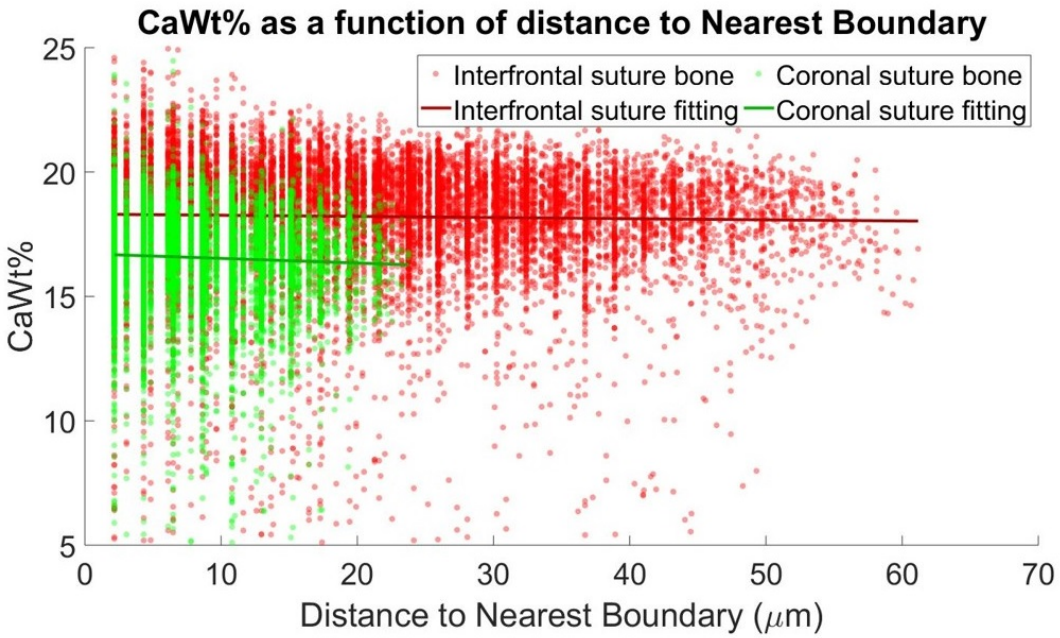

Figure 5.7: Results from sample two showing the CaWt% as a function of distance from the nearest boundary with a growh site. The data from the bone around the interfrontal suture and the coronal suture are shown in red and green respectively. *N=1*

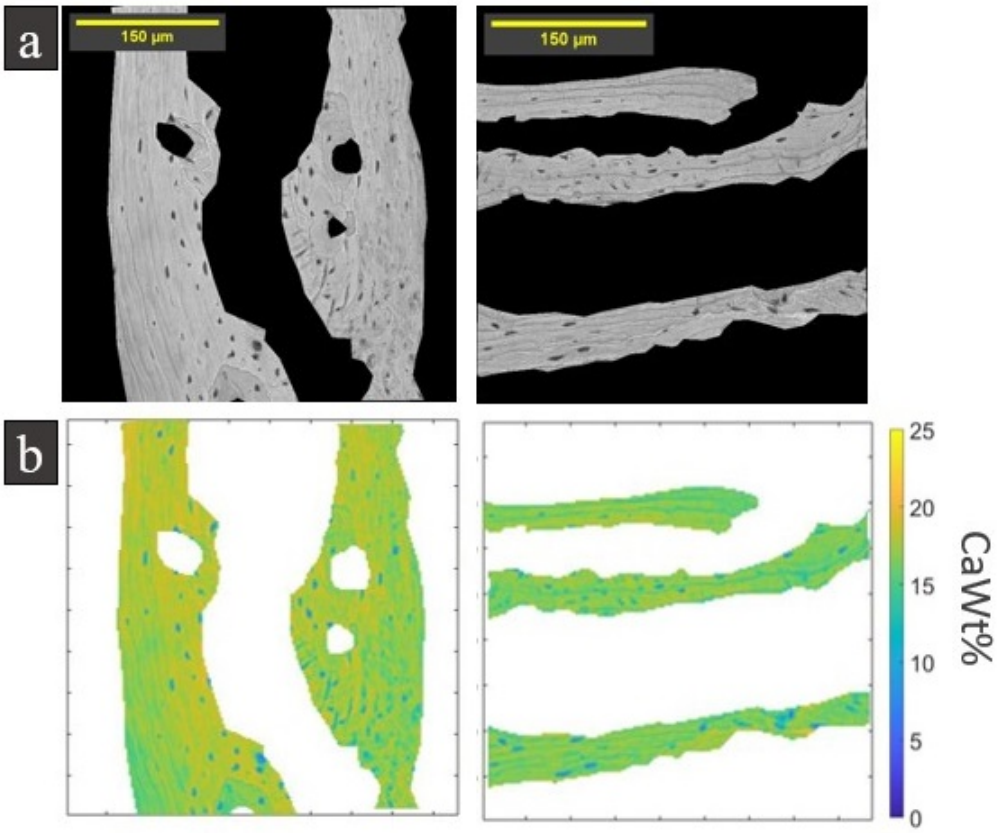

Figure 5.8: a) The masked BSE images for the nearest neighbour data seen in Figure 5.7. b) The heat map of BMD in the analysed regions in (a), where yellow indicates higher BMD, and the darker blue is less mineralised. *N=1*

5.3.1.2 Mineralisation from Dura Mater to Periosteum

Slices of the nonsutural bone were taken from sample one, and Figure 5.9a shows the stitched row of slices with a scale bar, as well as the specific slices for analysis. The results showing CaWt% as a function of distance from the interior surface of the cranial plate to the exterior surface on the slices can be seen in Figure 5.9b, where the five slices from Figure 5.9a have been analysed and plotted with the distance starting at the dura mater interface. All data sets show a decrease in CaWt% towards the centre, with the areas of highest mineral density being the surfaces of the cranial plate. The bone surfaces have CaWt% values ranging between 17% and 22%, whereas the central region with a lower mineral density ranges from 7% to 13%, with troughs in all slices being caused by lacunae.

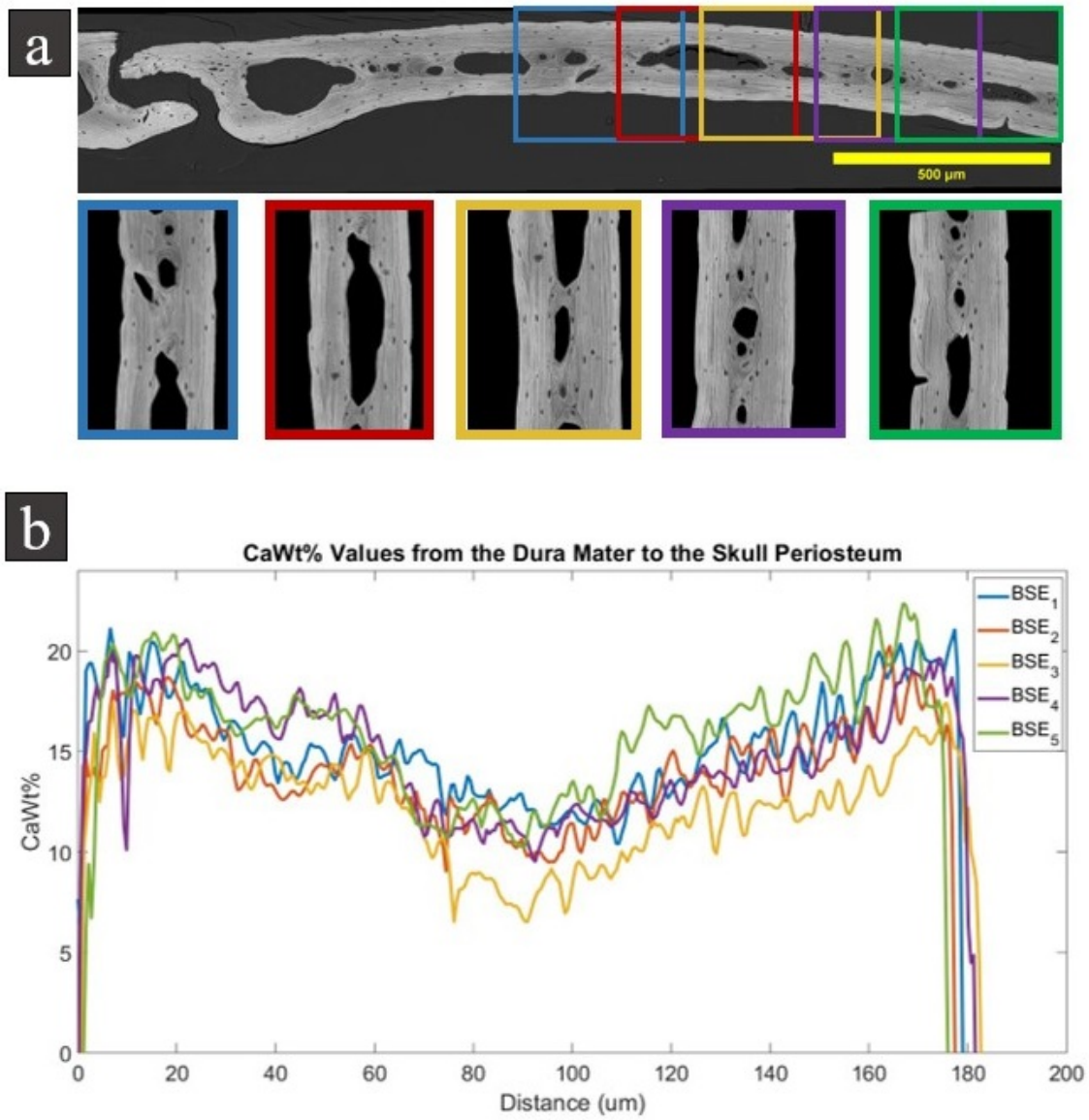

Figure 5.9: a) The raw BSE row from the sagittal suture to the non sutural bone, where the five slices from the non sutural bone have been masked in the bottom row. b) The results of CaWt% for slices of the non-sutural bone, where the CaWt% is a function of distance from the duramater to the persiosteum. *N=1*

5.3.1.3 Woven vs Lamellar Bone

The sutures imaged with BSE were the sagittal, squamous, interfrontal, and coronal, and so a comparison between the degree of mineralisation between the woven and lamellar bone structures is made near the growth sites. Figure 5.10 shows a bar graph of the average CaWt% values for the bone around each suture, with the woven bone data in purple, and the lamellar in green. The error bars are the standard deviation in the data set. Figure 5.11 shows the raw BSE images that were used to obtain the data in Figure 5.10. For each suture there is a higher CaWt% for the woven than the lamellar bone, with woven bone having CaWt% values ranging between 24.62% to 17.72%, and the lamellar ranging between 21.60% to 14.01%. Between the samples, sample one has mostly higher values than sample two.

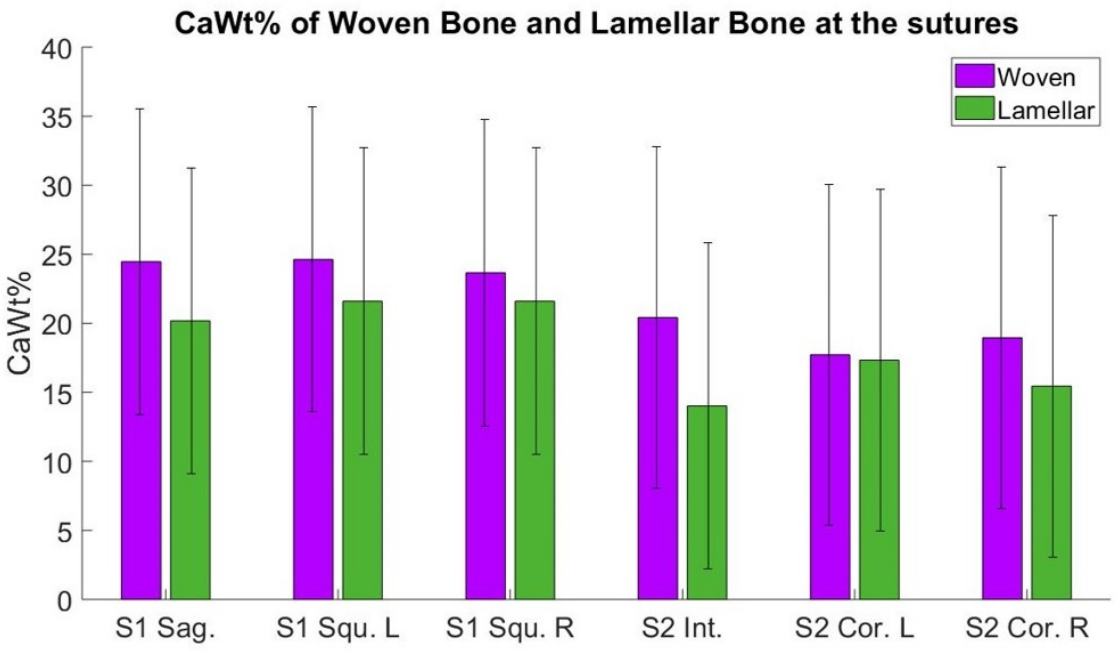

Figure 5.10: Bar graph of average CaWt% values for each suture, comparing the mean values of woven (purple) and lamellar (green) structures. The error bars indicate the standard deviation. *N=2*

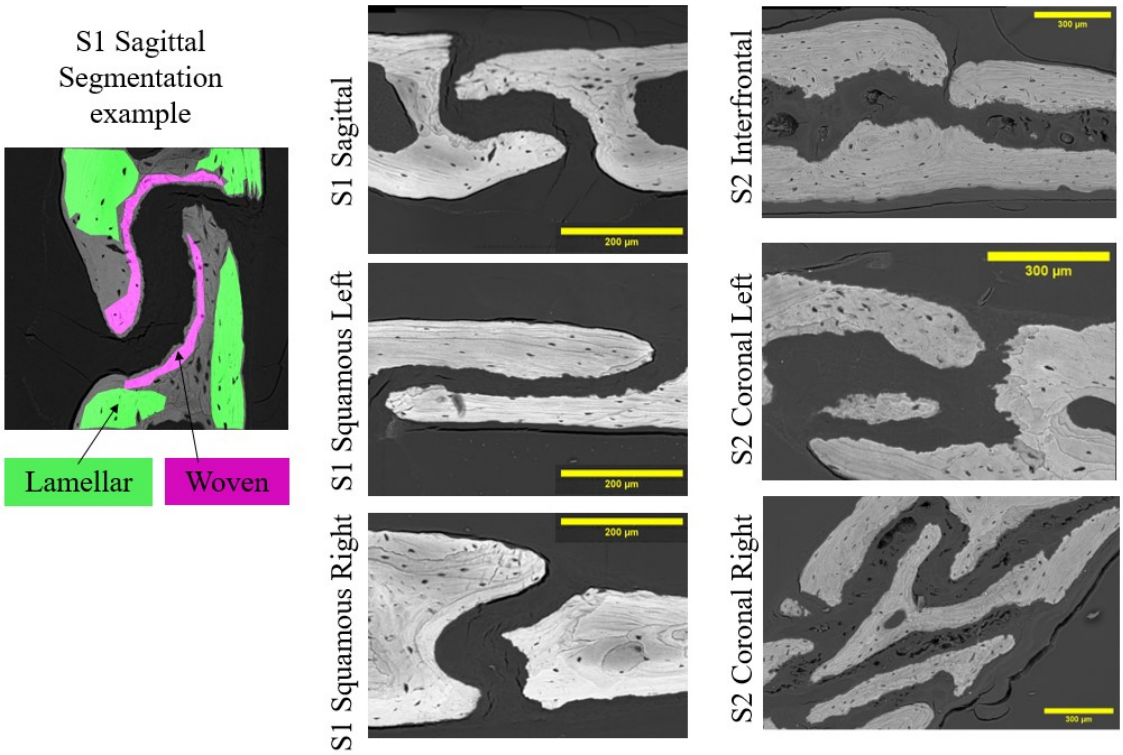

Figure 5.11: The images used for the woven vs lamellar data from Figure 5.10, with an example of a segmentation for the S1 sagittal sutural bone. *N=2*

5.3.2 Collagen Orientation

Figure 5.12 shows the sagittal suture of sample 3. Figure 5.12a is the SHG signal from collagen, and simultaneously the TPEF image (Figure 5.12b) was captured with the rhodamine staining in the tissue providing the spatial guidance on where the soft and hard tissues are. These two simultaneous modalities can be superimposed in a pixel-to-pixel manner as shown in Figure 5.12c

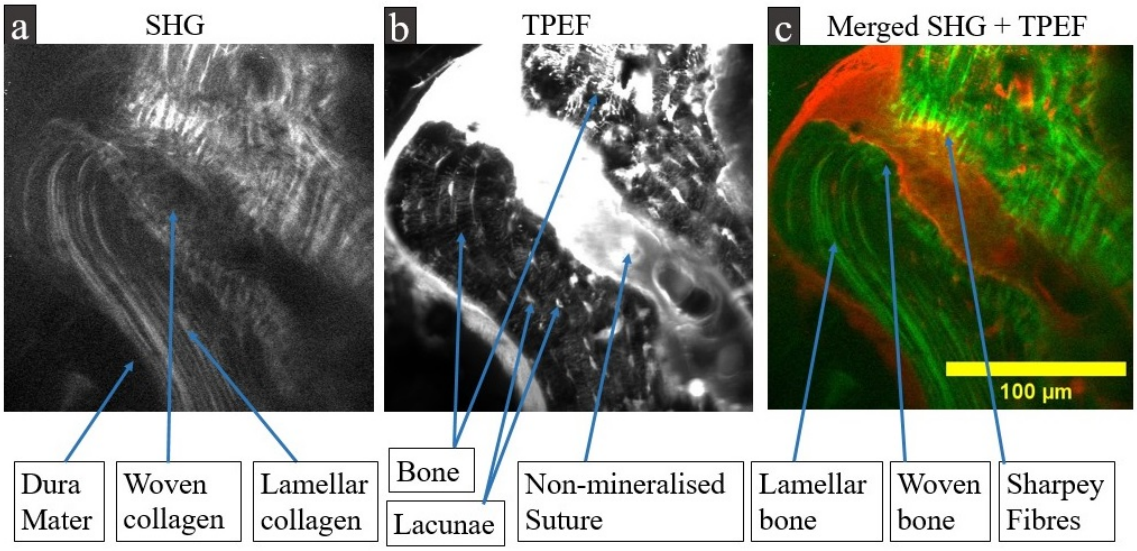

Figure 5.12: The SHG (a), TPEF (b), and Merged image (c) of the sagittal suture in a mouse skull, with the key features annotated. Collagen changes occur within the mineralised region on the bottom left located cranial plate, with evidence of woven bone shown by the different collagen arrangment. Sharpey's fibres are present in the top right located plate where the collagen fibres anchor between the mineralised plate, and the unmineralised region between them. *N=1*

5.3.2.1 PSHG Results

The pSHG images were acquired from the same region, with the cosine fitting curve of a point of the Sharpey's fibres shown in Figure 5.13a, with the two slices corresponding to the lowest and highest intensity shown in Figure 5.13b.

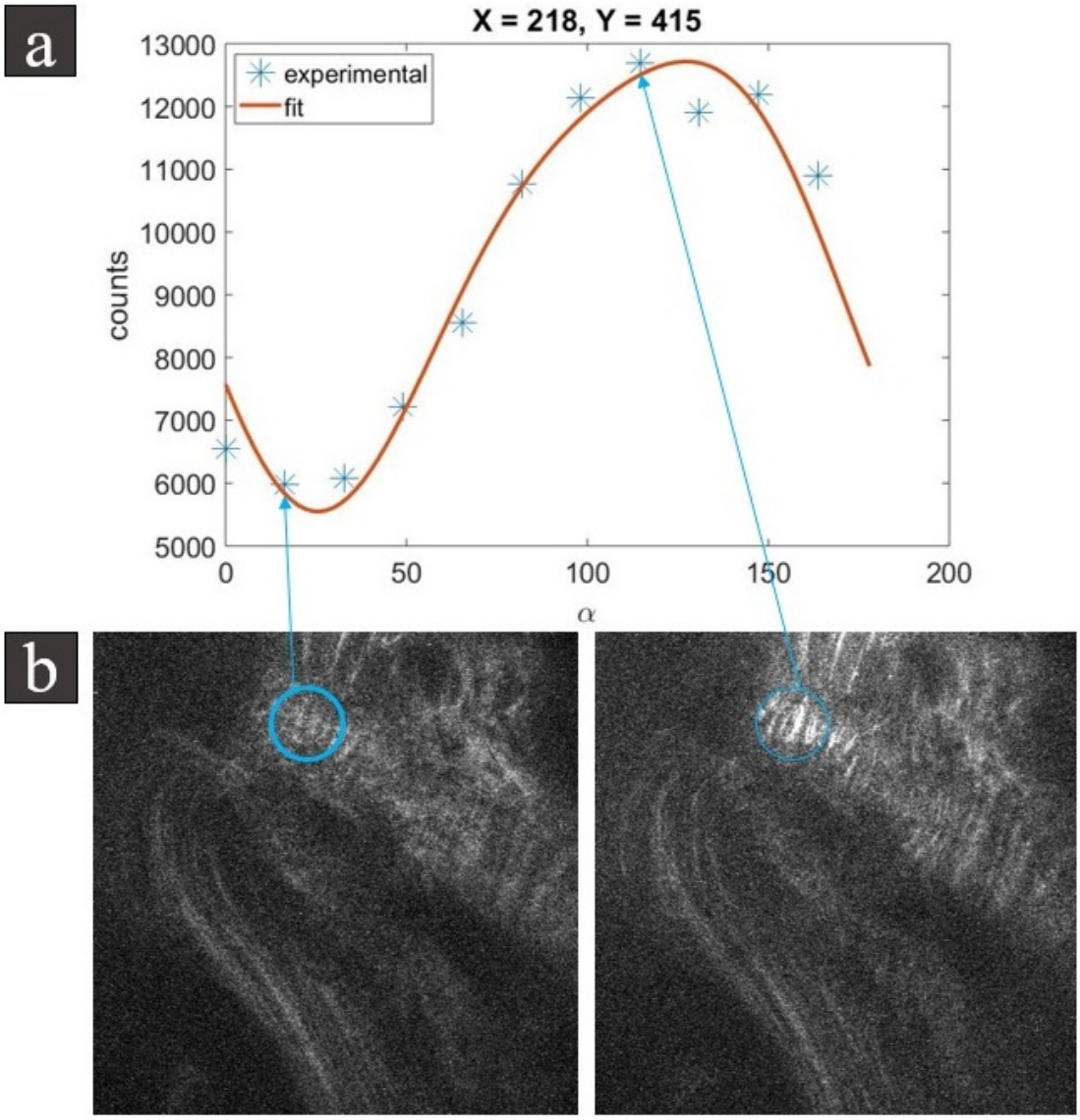

Figure 5.13: a) The fitting curve for a point at the Sharpey's fibres in the pSHG stack, where the blue asterisks are the raw experimental data, and the orange curve is the fitting. b) An example of two slices from the stack which show the lowest and highest intensities for the corresponding data plotted in (a), and can be visually seen by the change in intensity in the raw data. *N=1*

The I_2-$\Phi 2$ plot for this slice shows both the principle direction of the fibres, by the direction of the lines on the plot, as well as the degree of dispersion indicated by the colour of the respective lines, and is seen in 5.14a.

In Figure 5.14b the SHG analysed in (a) is shown with the distinct regions coloured, the lamellar bone in yellow, the woven bone in red, the suture in green, and the Sharpey's fibres in blue. The I_2 values from Figure 5.14a are plotted in Figure 5.14c as a series of histograms with the regions separated by the regions in 5.14b for direct comparison of the peak I_2 values.

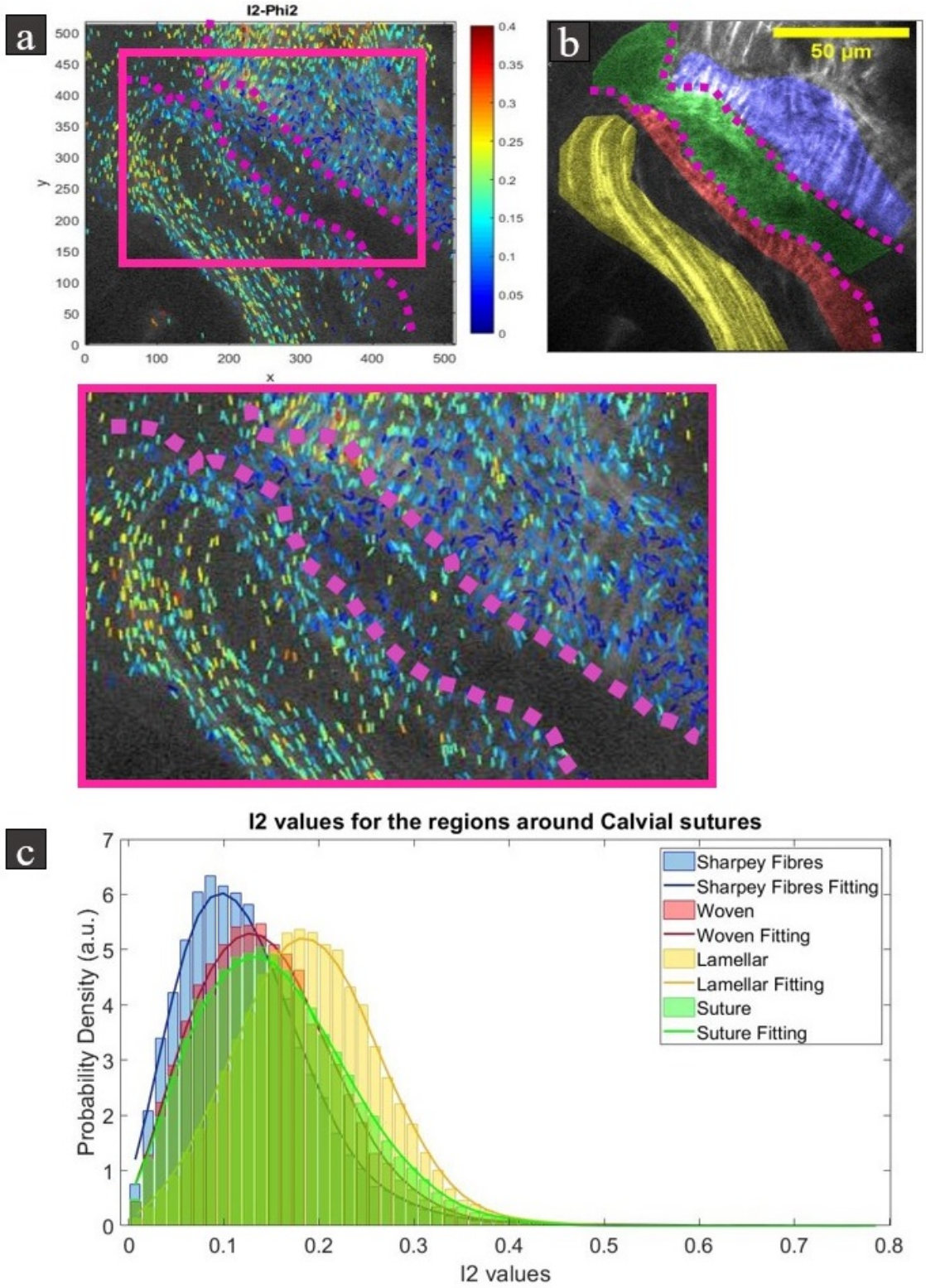

Figure 5.14: a) Plot showing the principle direction of the fibres (line direction) and the degree of dispersion (colour of line) in the sagittal suture and surrounding cranial plates in sample 2, on the tile shown in (b). The mineralisation interface on either side of the suture is given by the purple dashed line, and a closer view of the interfaces are seen in the pink box. b) The raw SHG frame with areas highlighted in colours to distinguish the lamellar bone (yellow), woven bone (red), suture (green) and Sharpey's fibres (blue), to correlate with the data in c. c) Histograms of the I_2 values for each region of interest around the cranial suture. The lamellar bone (yellow) is the most ordered with the highest peak I_2 value, followed by woven bone (red) and the unmineralised suture (green), and the greatest degree of dispersion is seen in the Sharpey's fibres (blue). *N=1*

5.4 Discussion

In sample one, the CaWt% values are a similar range, albeit at the lower end, to what is found in other papers that have studied other types of bone using QBEI, which have mean BMD values spanning from 17% to 27% depending on location and the health of the bone [265, 336, 343, 348]. Other techniques to assess BMD include dual x-ray absorptiometry (DXA) and μCT, which report in either area BMD, or volumetric BMD [87, 89, 349]. Whilst an exact conversion between area BMD and CaWt% cannot be made, a study on rodents which also carried out these measurements alongside QBEI show a range of CaWt% between 23% and 27% in the cortical bone of the tibia which is higher on average than what is reported by the results in this chapter (17% to 24% with higher and lower values being detected but anomalous) [350]. Reasons for this discrepancy could be due to the different bone types, as other studies have shown that the bone mineral density in different bones (skulls, clavicle, femoral diaphysis, etc.) have different mineral densities, which are individually dependent on factors such as age and loading environment [351].

More substantial contrast can be seen in local regions over a field of view approximately $200\ \mu m$ in size. In the non-sutural bone (Figure 5.9), the internal and external surfaces of the cranial plate have higher BMD than the centre regions, also reflected in other studies [352, 353]. Additionally, when taking into consideration that growth can occur at the blood vessel sites within the bone as well as the sutures, the distances from each site of growth has been explored to show that there is a decrease in BMD as the distance from the growth site increases. This structure of a mineral dense periosteum and endosteum is seen throughout other types of bones [53, 351, 354]. This is believed as a compromise between

strength of the minerals to resist load-induced deformation, and being lightweight and porous enough to ensure more energy-efficient movement and nutrition delivery [15].

On a smaller length scale, the CaWt% has been compared between the woven and lamellar structures of the bone, with overall values falling within the ranges in the larger field of view data sets. However, this data shows that in each suture imaged, the woven bone has a higher mineral density than that of the neighbouring lamellar bone. Whether this is in line with other reports depends on the specific study. Woven bone has been reported to have a higher mineralisation in experiments comparing the mechanical strains in the two bone types, and high resolution imaging techniques [100–104]. However, reports of woven bone having a low mineral density have also been published [105], but due to the definition of woven bone being based on the collagen arrangement, variables that could explain the different observation, such as whether it is newly growing bone or if it is a fracture healing response would need further studies to assess the consistency of woven bone mineralisation across the body.

Sample two contains one interfrontal suture and two coronal sutures, and visibly has more interdigitation compared to the others that can be seen in Figure 5.11. The highly interdigitated pattern of the coronal sutures is indicative of higher stresses being experienced [239,240]. This difference in interdigitation can be explained by the location of the respective sutures, with the coronal and squamous sutures being closer to the lower jaw, and therefore experience unique stresses during mastication that the interfrontal and sagittal do not.

On the other hand, the soft constituent of this interface, collagen, exhibits distinct patterns across the mineralised and unmineralised regions. The results of this chapter reinforce the evidence that the collagen bundles within the cranial plate form lamellar sheets parallel to the bone surface for mechanical stability [355].

In both of the mineralisation interfaces imaged, the collagen across the interface takes on either the form of Sharpey's fibres, or woven collagen, and both can be seen to be continuous between the mineralised and non-mineralised tissue. This is a verification of what has been seen by other imaging methods, such as histology, of the suture-bone interface and mathematical models of how mechanotransduction occurs across the mechanically different tissues [228, 233, 249, 250, 356].

The difference in information from the 2D image from SHG + TPEF, and the 3D organisational data from pSHG is exhibited by the comparison between the Sharpey's fibres and the lamellar bone. In the 2D SHG + TPEF images they appear to have a similar structure on the length scale imaged, arising from the similar macroscale fibrillar structure, but the pSHG data, which analyses the smaller scale organisation, shows a difference in the degree of dispersion, with the lamellar bone having more highly ordered collagen than the Sharpey's Fibres.

The pSHG data confirms that the change in collagen dispersion occurs at the boundary between the lamellar and woven bone, rather than at the mineralisation boundary, as the difference in collagen dispersion between the unmineralised suture and the woven bone does not exhibit a peak change, but there is a shift to more ordered collagen in the lamellar bone. These findings correlate with current understanding that woven bone has more disordered collagen [357, 358], and

demonstrate the collagen continuity across the suture and woven bone interface. This data for the lamellar bone in comparison to the suture and woven is as expected from the images, and from theory [98, 102, 104, 359, 360]. However, whilst Sharpey's fibres have been well documented as being predominantly type I collagen in cranial suture-bone interfaces and in other locations of the body [103, 361], it is interesting that despite resembling more closely the lamellar bone on the single SHG images, the collagens in this region have a greater degree of dispersion than within either the lamellar, woven bone, or unmineralised suture.

The collagen of the sutures has been reported to absorb more energy during mechanical stress than the neighbouring cranial plates [323, 326]. The continuity of collagen organisation across mechanically dissimilar tissues shown in these experiments could be an aid in distributing loads and resisting fractures at the interface between mineralised tissue and soft tissue.

Limitations within this experiment are largely down to having few samples to image, and therefore this work so far does not have the repeatability needed to yield any statistical significance. Specific limitations on the methods used include requirement of a parallel imaging surface for the QBEI, which any deviation from can cause the pixel intensity to vary across the sample [362]. This means that samples which have any tilt are unusable for this method without extensive recalibration of equipment for each sample. For the multiphoton imaging, the rhodamine dye which penetrates the non-mineralised regions of the tissue is sensitive to photobleaching [363], and the high intensity laser required for multiphoton imaging means there is a compromise on the scanning time to ensure preservation of the sample. This has been minimised in this experiment by using a lower laser power with a fast scan, but with averaging the frames.

5.5 Conclusions and Future Work

In this project, the mineral distribution around the calvarial sutures has been imaged and quantified with BSE and QBEI. These experiments aimed to investigate how the mineral distribution is spatially organised in cranial bones, and whether the factors of distance from a soft tissue growth site, and bone type (lamellar or woven) correlate to any differences in the degree of mineralisation. The results indicate there is a higher mineral density in the newly laid down woven bone, as well as the interior and exterior surfaces of the lamellar bone.

The use of QBEI has previously been established to verify the CaWt% in long bones [336, 348], and areas containing woven bone have been shown to have a higher mineral density with this method. This study is the first to use QBEI for assessing the mineralisation around the calvarial sutures where the mineralisation process is intramembranous ossification. These results show a range of bone mineral density values (15%-22%) slightly lower than that of long bone (22%-25%) [336], but with the same pattern of woven bone having a higher mineral density than that of the neighbouring lamellae.

The research question of how the collagen type, direction, and dispersion changes across the soft hard interfaces of the skull has led to the use of SHG imaging and pSHG to quantify these features in this region of interest. In the woven bone and in the unmineralised region of the suture, the principle fibre direction appears to bridge the two mineralised plates, with the majority creating a gradual transition from the principle lamellar direction, and into the Sharpey's fibres of the opposite boney plate.

The Sharpey's fibres themselves have low I2 values, which indicate a high degree of dispersion and continue between the mineralised cranial plate and the

unmineralised suture. On the opposite side of the suture the dispersion of collagen and principle direction is also continuous across the interface, despite the fibrillar macrostructure arrangement of these collagens being different to the opposite interface. These features could be beneficial for dissipating stress at the site of ossification, whilst maintaining a cohesive structure to prevent cleaving at the soft-hard tissue interface.

To make this work statistically significant, more samples will need to be used in future work which will give more confidence to the findings on the spatial gradients of the minerals and collagen organisation at the soft-hard interfaces in the skull. In future experiments the pSHG arrangement between the different sutures would be interesting to continue, to assess whether there is a change in the peak I2 values from different sutures, and whether the Sharpey's fibres in each suture and other locations of the body have similar degrees of dispersion. This would provide valuable insight into their anchoring mechanisms.

This is a preliminary study into how the mineralisation and collagen are organised around the calvarial sutures. Additional work is planned to image the same samples using a confocal laser scanning microscope. This will enable us to compare the OLCN in woven and lamellar bone, and to investigate how these parameters relate to changes in mineralisation and the corresponding arrangement of collagen fibres.

Chapter 6

Summaries and Future Work

The experiments carried out in this thesis look at two different mineralising interfaces and have used a variety of imaging modalities to characterise the neighbouring tissues in terms of their mineral heterogeneity, collagen organisation, and for the VEP, the cell network density distribution to answer the specific questions of:

- How does the microscale distribution of minerals in mineralised tissue vary as a function of distance from the interface of hard and soft tissue?
- Are the quantifiable features of the OLCN in the irregular bone of the vertebrae comparable to the values already established in long bones?
- How does the collagen type, orientation, and degree of dispersion change across the two mechanically different tissues, and is there a spatial correlation between collagen changes, and mineralisation changes?

The experiments characterising EP have resulted in the following key findings:

- The mineral distribution is heterogenous, with higher degrees of mineralisation and heterogeneity seen in the mineralised CEP, with the SBP and

trabecular sharing the same peak values, but more variation of mineral densities in the trabecular bone.

- The canaliculi density has been assessed in the central VEP, between the CEP and growth plate, with average values ranging from 0.05-0.14 $\mu m/\mu m^3$, but with high standard deviations.

- The collagen arrangement across the multiple interfaces within the endplate structure has demonstrated a higher degree of dispersion within the CEP than the VEP, but at the interface the collagen bundles are aligned, with the same principle direction.

For the studies into the mineralising interfaces within the cranium the main points are summarised below:

- The CaWt % was quantified across the cranial plate, with findings showing that the degree of mineralisation decreases with distances from a growth site, and that the newly laid woven bone has a higher degree of mineralisation than the neighbouring lamellar bone. Towards the centre of the cranial plates, there is more highly mineralised bone neighbouring the dura mater and periosteum, at the interior and exterior surfaces of the skull.

- The collagen across this interface has continuity across the soft-hard boundary, with changes in direction and dispersion of the collagen occurring within the mineralised tissue.

Both of these regions of interest show that the changes in collagen type, direction, and dispersion are spatially distinguishable from the interface of soft and hard tissues, evidencing that multiple unique interfaces exist within these tissues.

6.1 Future studies

There are many routes that can follow on from the research carried out here and from gaps in current literature, some of which have been mentioned in the relevant chapters. A few project ideas which would be complementary to the work carried out in this thesis are summarised below.

- The lacunae distribution in the spine could be repeated for either older animal models, or different motion segments. There are multiple regions that can be compared, such as cranial vs caudal, peripheral vs central, and anterior vs posterior. All sections from 1 lumbar spine (<1yr) have been embedded already with Technovit 9100 which can be used for such a project. The same series of Python scripts, TINA, used to look at the lacunae distribution and canaliculi density, should be carried out on more samples within these variable parameters to assess how irregular bones compare to long bones which have been studied in more depth.

- A pSHG study on how the collagen dispersion might change between aged samples for these interfaces, which could provide greater insight into whether collagen attachments change and therefore increase fracture risk with ageing.

- A plan for this thesis which there was not enough time for was to use the inVia Raman microscope set up to create a map of the phosphate and carbonate peaks across the VEP and mineralised CEP. This could create a map of both the degree of mineralisation, by comparing the sum of the mineral peak intensities, to the total matrix peak intensities, as well as comparing the type of mineral, by assessing the ratio of phosphate to carbonate content

over the mineralised CEP and VEP. This would help determine the relative rates of remodelling between the regions, and would be interesting to carry out on both young spine samples, and aged.

- A theory still to be tested is the extent of how the mineralisation of the CEP aids in anchoring the two mechanical different tissues of the non mineralised CEP and the VEP. This can be investigated by comparing the mechanical response, via pulling tests, on fresh healthy samples that are hydrated, to the response of a decalcified sample. SHG and pSHG images could help assess the degree of collagen distortion in both scenarios, and if testing until fracture, the stress-strain graphs along with the SHG images of the fracture location, can be compared to help assess the role of the mineralised CEP.

6.2 Conclusions

This thesis has detailed the relevant literature, experimental protocols, results, and scientific significance of the projects carried out throughout this PhD. The aims and objectives when starting this project were to better understand the relationship between the mineral distribution and collagen organisation at mineralising interfaces, by quantifying these features and assessing the values in their spatial arrangement. This has required the use of extensive sample preparation and image analysis to achieve these aims.

Whilst the two chapters on the experiments focus on different soft-hard interfaces, the characterisation of these interfaces and where similarities and differences may occur is important for better understanding the mechanics, role, and vulnerabilities of each interface.

Bibliography

[1] Jennifer Stewart Williams, Nawi Ng, Karl Peltzer, Alfred Yawson, Richard Biritwum, Tamara Maximova, Fan Wu, Perianayagam Arokiasamy, Paul Kowal, and Somnath Chatterji. Risk factors and disability associated with low back pain in older adults in low- and middle-income countries. Results from the WHO study on global AGEing and adult health (SAGE). *PLoS ONE*, 10(6):1–21, 2015.

[2] N. Maniadakis and A. Gray. The economic burden of low back pain in the United Kingdom. *Pain*, 84(1):95–103, 2000.

[3] Ceri J Phillips. The cost and burden of chronic pain. *Reviews in Pain*, 3(1):2–5, 2009.

[4] Rui Martins, Nikos Kotsopoulos, Melodi Kosaner Kließ, Craig Beck, Lucy Abraham, Samuel Large, Patricia Schepman, and Mark P. Connolly. Comparing the fiscal consequences of controlled and uncontrolled osteoarthritis pain applying a uk public economic perspective. *Journal of Health Economics and Outcomes Research*, 8(1):127–136, 2021.

[5] Greg Coates, Peter Clewes, Christoph Lohan, Hannah Stevenson, Robert Wood, Theo Tritton, Roger Knaggs, Alastair J. Dickson, and David Walsh. Health economic impact of moderate-to-severe chronic pain associated

with osteoarthritis in england: A retrospective analysis of linked primary and secondary care data. *BMJ Open*, 13(7), 2023.

[6] W. T. Crow and D. R. Willis. Estimating cost of care for patients with acute low back pain: a retrospective review of patient records. . *J Am Osteopath Assoc*, 109(4):229–233, 2009.

[7] A. Chen, C. Gupte, K. Akhtar, P. Smith, and J. Cobb. The Global Economic Cost of Osteoarthritis: How the UK Compares. *Arthritis*, 2012:1–6, 2012.

[8] Matthew R. Mccann and Cheryle A. Séguin. Notochord Cells in Intervertebral Disc Development and Degeneration. *Journal of Developmental Biology*, 4(3), 2016.

[9] Robert J. Moore. The vertebral endplate: Disc degeneration, disc regeneration. *European Spine Journal*, 15(SUPPL. 3):333–337, 2006.

[10] Masaki Yanagishita. Function of proteoglycans in the extracellular matrix. *Pathology International*, 43(6):283–293, 1993.

[11] Olga Leonova, Evgenii Baykov, Abdugafur Sanginov, and Aleksandr Krutko. Cervical Disc Degeneration and Vertebral Endplate Defects After the Fused Operation. *Spine (Phila Pa 1976)*, 46(18), 2021.

[12] S. Aydin, B. Kucukyuruk, and G. Z. Sanus. Cranioplasty: Review of materials and techniques. *J Neurosci Rural Pract.*, 2(2):162–167, 2011.

[13] A. Szathmari, A. Morgado, P. A. Beuriat, P. Petrescu, F. Di Rocco, and C. Mottolese. Cranioplasty for bone defects after craniosynostosis surgery. Case series with literature review. *Neurochirurgie*, 66(2):97–101, 2020.

[14] John P. Bilezikian, Lawrence G. Raisz, and Gideon A. Rodan. *Principles of Bone Biology: Second Edition, Volume 1*. 2002.

[15] Y. Fung. *Biomechanics: Mechanical Properties of Living Tissues 2nd edition*. Springer, 1993.

[16] R. A. Stockwell. *Biology of Cartilage Cells: Biological Structure and Function*. Cambridge University Press, 1979.

[17] Keke Wang, Xiangguang Meng, and Zhikun Guo. Elastin Structure, Synthesis, Regulatory Mechanism and Relationship With Cardiovascular Diseases. *Frontiers in Cell and Developmental Biology*, 9(November):1–10, 2021.

[18] Renato de Moraes, Ana Maria de Guzzi Plepis, Virginia da Conceição Amaro Martins, Marco Antonio Hungaro Duarte, Murilo Priori Alcalde, Rogerio Leone Buchaim, Karina Torres Pomini, Eduardo Gomes Machado, Marcelo de Azevedo e Sousa Munhoz, Fernando Bento Cunha, Amanda Regina Alves Calegari, Amilton Iatecola, Samantha Ketelyn Silva, and Marcelo Rodrigues da Cunha. Suitability of the use of an elastin matrix combined with bone morphogenetic protein for the repair of cranial defects. *American Journal of Translational Research*, 11(8):5261–5271, 2019.

[19] Leslie Baumann, Eric F. Bernstein, Anthony S. Weiss, Damien Bates, Shannon Humphrey, Michael Silberberg, and Robert Daniels. Clinical Relevance of Elastin in the Structure and Function of Skin. *Aesthetic Surgery Journal Open Forum*, 3(3):1–8, 2021.

[20] Matthew D. Shoulders and Ronald T. Raines. Collagen structure and stability. *Annual Review of Biochemistry*, 78:929–958, 2009.

[21] W. T. Astbury and F. O. Bell. Molecular Structure of the Collagen Fibres. *Nature*, 145(3672):421–422, 1940.

[22] L. Pauling and Corey R. The Structure of Fibrous Proteins of the Collagen-Gelatin Group. *Proceedings of the National Academy of Sciences of the United States of America*, 37(5):272–281, 1951.

[23] P. M. Cowan, S. McGavin, and A. C. T. North. The Polypeptide Chain Configuration of Collagen. *Nature*, 176:1062–1064, 1955.

[24] R. B. Rucker and J. Murray. Cross-linking amino acids in collagen and elastin. *American Journal of Clinical Nutrition*, 31(7):1221–1236, 1978.

[25] R. C. Siegel. Collagen cross linking. Synthesis of collagen cross links in vitro with highly purified lysyl oxidase. *Journal of Biological Chemistry*, 251(18):5786–5792, 1976.

[26] Andreas Herchenhan, Franziska Uhlenbrock, Pernilla Eliasson, Maryann Weis, David Eyre, Karl E. Kadler, S. Peter Magnusson, and Michael Kjaer. Lysyl oxidase activity is required for ordered collagen fibrillogenesis by tendon cells. *Journal of Biological Chemistry*, 290(26):16440–16450, 2015.

[27] Olga Antipova and Joseph P. R. O. Orgel. In situ D-periodic molecular structure of type II collagen. *Journal of Biological Chemistry*, 285(10):7087–7096, 2010.

[28] S. A. Paul Chubb. Measurement of C-terminal telopeptide of type I collagen (CTX) in serum. *Clinical Biochemistry*, 45(12):928–935, 2012.

[29] Róisín Holmes, Steve Kirk, Giuseppe Tronci, Xuebin Yang, and David Wood. Influence of telopeptides on the structural and physical properties of

polymeric and monomeric acid-soluble type I collagen. *Materials Science and Engineering C*, 77:823–827, 2017.

[30] Fabio Nudelman, Koen Pieterse, Anne George, Paul H. H. Bomans, Heiner Friedrich, Laura J. Brylka, Peter A. J. Hilbers, Gijsbertus de With, and Nico A. J. M. Sommerdijk. The role of collagen in bone apatite formation in the presence of hydroxyapatite nucleation inhibitors. *Nat Mater.*, 9(112):1004–1009, 2010.

[31] Elizabeth G. Canty, Yinhui Lu, Roger S. Meadows, Michael K. Shaw, David F. Holmes, and Karl E. Kadler. Coalignment of plasma membrane channels and protrusions (fibropositors) specifies the parallelism of tendon. *Journal of Cell Biology*, 165:553–563, 5 2004.

[32] Philip C. Trackman. Diverse biological functions of extracellular collagen processing enzymes. *Journal of Cell Biochemistry*, 96:927–937, 2005.

[33] M. Wu, K. Cronin, and J. S. Crane. *Biochemistry, Collagen Synthesis.* StatPearls Publishing, Treasure Island (FL), 2022.

[34] Harry C. Blair, Quitterie C. Larrouture, Yanan Li, Hang Lin, Donna Beer-Stoltz, Li Liu, Rocky S. Tuan, Lisa J. Robinson, Paul H. Schlesinger, and Deborah J. Nelson. Osteoblast differentiation and bone matrix formation in vivo and in vitro. *Tissue Engineering - Part B: Reviews*, 23(3):268–280, 2017.

[35] Morten A. Karsdal. *Biochemistry of Collagens, Laminins and Elastin: Structure, Function and Biomarkers*. Elsevier, 2016.

[36] Masahiko Terajima, Irina Perdivara, Marnisa Sricholpech, Yoshizumi Deguchi, Nancy Pleshko, Kenneth B. Tomer, and Mitsuo Yamauchi. Glycosylation and cross-linking in bone type I collagen. *Journal of Biological Chemistry*, 289(33):22636–22647, 2014.

[37] Marc D. Grynpas, David R. Eyre, and Daniel A. Kirschner. Collagen type II differs from type I in native molecular packing. *BBA - Protein Structure*, 626(2):346–355, 1980.

[38] Sameer Varma, Joseph P. R. O. Orgel, and Jay D. Schieber. Nanomechanics of Type I Collagen. *Biophysical Journal*, 111(1):50–56, 2016.

[39] Karin A. Jansen, Albert J. Licup, Abhinav Sharma, Robbie Rens, Fred C. MacKintosh, and Gijsje H. Koenderink. The Role of Network Architecture in Collagen Mechanics. *Biophysical Journal*, 114(11):2665–2678, 2018.

[40] Janna K. Mouw, Guanqing Ou, and Valerie M. Weaver. Extracellular matrix assembly: a multiscale deconstruction. *Nat Rev Mol Cell Biol.*, 15(12):771–785, 2014.

[41] Emilie Gachon and Patrick Mesquida. Stretching Single Collagen Fibrils Reveals Nonlinear Mechanical Behavior. *Biophysical Journal*, 118(6):1401–1408, 2020.

[42] Markus J. Buehler. Nature designs tough collagen: Explaining the nanostructure of collagen fibrils. *Proceedings of the National Academy of Sciences of the United States of America*, 103(33):12285–12290, 2006.

[43] Maria P. McGee, Michael Morykwas, Julie Shelton, and Louis Argenta. Collagen unfolding accelerates water influx, determining hydration in the interstitial matrix. *Biophysical Journal*, 103(10):2157–2166, 2012.

[44] Florenzo Iannone and Giovanni Lapadula. The pathophysiology of osteoarthritis. *Aging Clinical and Experimental Research*, 15(5):364–372, 2003.

[45] N. Arden, F. J. Blanco, O. Bruyere, C. Cooper, A. Guermazi, D. Hayashi, D. Hunter, M. K. Javaid, F. Rannou, J. Reginster, and F. W. Roemer. *Atlas of Osteoarthritis*, volume 60. Springer Healthcare Ltd., London, second edition, 2018.

[46] Abby E. Peters, Riaz Akhtar, Eithne J. Comerford, and Karl T. Bates. The effect of ageing and osteoarthritis on the mechanical properties of cartilage and bone in the human knee joint. *Scientific Reports*, 8(1):1–13, 2018.

[47] Daniel L. Bader, Geoffrey E. Kempson, John Egan, Wendy Gilbey, and Alan J. Barrett. The effects of selective matrix degradation on the short-term compressive properties of adult human articular cartilage. *BBA - General Subjects*, 1116(2):147–154, 1992.

[48] Hattie C. Cutcliffe and Louis E. DeFrate. Comparison of Cartilage Mechanical Properties Measured During Creep and Recovery. *Scientific Reports*, 10(1):1–8, 2020.

[49] Farshid Guilak. Biomechanical factors in osteoarthritis. *Best Practice and Research: Clinical Rheumatology*, 25(6):815–823, 2011.

[50] Adam Aron Mieloch, Magdalena Richter, Tomasz Trzeciak, Michael Giersig, and Jakub Dalibor Rybka. Osteoarthritis severely decreases the elasticity and hardness of knee joint cartilage: A nanoindentation study. *Journal of Clinical Medicine*, 8(11):1–11, 2019.

[51] Federica Boschetti and Giuseppe M. Peretti. Tensile and compressive properties of healthy and osteoarthritic human articular cartilage. *Biorheology*, 45(3):337–344, 2008.

[52] Orestis G. Andriotis, Kareem Elsayad, David E. Smart, Mathis Nalbach, Donna E. Davies, and Philipp J. Thurner. Hydration and nanomechanical changes in collagen fibrils bearing advanced glycation end-products. *Biomedical Optics Express*, 10(4):1841, 2019.

[53] X. Su, K. Sun, F. Z. Cui, and W. J. Landis. Organization of apatite crystals in human woven bone. *Bone*, 32(2):150–162, 2003.

[54] Xu Feng. Chemical and Biochemical Basis of Cell-Bone Matrix Interaction in Health and Disease. *Current Chemical Biology*, 3(2):189–196, 2009.

[55] D. S. Bocciarelli. Morphology of crystallites in bone. *Calcified Tissue Research*, 5(1):261–269, 1970.

[56] Selvaraj Vimalraj. Alkaline phosphatase: Structure, expression and its function in bone mineralization. *Gene*, 754, 2020.

[57] Hideo Orimo. The Mechanism of Mineralization and the Role of Alkaline Phosphatase in Health and Disease. *Journal of Nippon Medical School*, 77(1):4–12, 2010.

[58] H. Clarke Anderson. Matrix vesicles and calcification. *Current rheumatology reports*, 5(3):222–226, 2003.

[59] Ellis E. Golub. Role of Matrix Vesicles in Biomineralization Ellis. *Biochim Biophys Acta.*, 1790(12):1592–1598, 2009.

[60] Sana Ansari, Bregje W. M. de Wildt, Michelle A. M. Vis, Carolina E. de Korte, Keita Ito, Sandra Hofmann, and Yuana Yuana. Matrix vesicles: Role in bone mineralization and potential use as therapeutics. *Pharmaceuticals*, 14(4):1–27, 2021.

[61] C. Rey, C. Combes, C. Drouet, and M. J. Glimcher. Bone mineral: update on chemical composition and structure. *Osteoporosis International*, 20(6):1013–1021, 2009.

[62] M. Egerbacher, M. Helmreich, E. Mayrhofer, and P. Böck. Mineralisation of the hyaline cartilage in the small-spotted dogfish Scyliorhinus Canicula L. *Scripta Medica (BRNO)*, 79(4):199–212, 2006.

[63] Natacha A. Agabalyan, Darrell J. R. Evans, and Rachael L. Stanley. Investigating tendon mineralisation in the avian hindlimb: A model for tendon ageing, injury and disease. *Journal of Anatomy*, 223(3):262–277, 2013.

[64] Ozan Akkus, Fran Adar, and Mitchell B. Schaffler. Age-related changes in physicochemical properties of mineral crystals are related to impaired mechanical function of cortical bone. *Bone*, 34(3):443–453, 2004.

[65] Roland Krug, Andrew J. Burghardt, Sharmila Majumdar, and Thomas M. Link. High-resolution Imaging Techniques for the Assessment of Osteoporosis. *Radiol Clin North Am.*, 248(3):601–621, 2010.

[66] Marie T. O'Toole. *Mosby's Dictionary of Medicine, Nursing and Health Professions Tenth Edition*. Elsevier, 2017.

[67] Silvia Pabisch, Wolfgang Wagermaier, Thomas Zander, Chenghao Li, and Peter Fratzl. *Imaging the nanostructure of bone and dentin through small- and wide-angle X-ray scattering*, volume 532. Elsevier Inc., 1st edition, 2013.

[68] Sidney Omelon, John Georgiou, Zachary J. Henneman, Lisa M. Wise, Balram Sukhu, Tanya Hunt, Chrystia Wynnyckyj, Douglas Holmyard, Ryszard Bielecki, and Marc D. Grynpas. Control of vertebrate skeletal mineralization by polyphosphates. *PLoS ONE*, 4(5), 2009.

[69] A. Roschger, P. Roschger, W. Wagermaier, J. Chen, A. F. van Tol, F. Repp, S. Blouin, A. Berzlanovich, G. M. Gruber, K. Klaushofer, P. Fratzl, and R. Weinkamer. The contribution of the pericanalicular matrix to mineral content in human osteonal bone. *Bone*, 123:76–85, 2019.

[70] Mahdi Ayoubi, Alexander F. van Tol, Richard Weinkamer, Paul Roschger, Peter C. Brugger, Andrea Berzlanovich, Luca Bertinetti, Andreas Roschger, and Peter Fratzl. 3D Interrelationship between Osteocyte Network and Forming Mineral during Human Bone Remodeling. *Advanced Healthcare Materials*, 10(12):1–11, 2021.

[71] Wolfie Traub, Talmon Arad, and Stephen Weiner. Origin of Mineral Crystal Growth in Collagen Fibrils. *Matrix*, 12:251–255, 1992.

[72] Zhaoyong Zou, Tengteng Tang, Elena MacÍas-Sánchez, Sanja Sviben, William J. Landis, Luca Bertinetti, and Peter Fratzl. Three-dimensional structural interrelations between cells, extracellular matrix, and mineral

in normally mineralizing avian leg tendon. *Proceedings of the National Academy of Sciences of the United States of America*, 117(25):14102–14109, 2020.

[73] Dimitrios J. Hadjidakis and Ioannis I. Androulakis. Bone remodeling. *Annals of the New York Academy of Sciences*, 1092:385–396, 2006.

[74] Rinaldo Florencio-Silva, Gisela Rodrigues Da Silva Sasso, Estela Sasso-Cerri, Manuel Jesus Simões, and Paulo Sérgio Cerri. Biology of Bone Tissue: Structure, Function, and Factors That Influence Bone Cells. *BioMed Research International*, 2015, 2015.

[75] Vivekanand Sabanna Kattimani, Sudheer Kondaka, and Krishna Prasad Lingamaneni. Hydroxyapatite — Past , Present , and Future in Bone Regeneration. *Bone and Tissue Regeneration Insights*, 7:9–19, 2016.

[76] Christof Land and Eckhard Schoenau. Fetal and postnatal bone development: reviewing the role of mechanical stimuli and nutrition. *Best Practice and Research in Clinical Endocrinology and Metabolism*, 22(1):107–118, 2008.

[77] Eve Donnelly, Dan X. Chen, Adele L. Boskey, Shefford P. Baker, and Marjolein C. H. van der Meulen. Contribution of mineral to bone structural behavior and tissue mechanical properties. *Calcif Tissue Int.*, 87(5):450–460, 2010.

[78] Himadri S. Gupta, Jong Seto, Wolfgang Wagermaier, Paul Zaslansky, Peter Boesecke, and Peter Fratzl. Cooperative deformation of mineral and collagen in bone at the nanoscale. *Proceedings of the National Academy of Sciences of the United States of America*, 103(47):17741–17746, 2006.

[79] Yue Sa, Yaru Guo, Xiaowei Feng, Man Wang, Ping Li, Yixue Gao, Xu Yang, and Tao Jiang. Are different crystallinity-index-calculating methods of hydroxyapatite efficient and consistent? *New Journal of Chemistry*, 41(13):5723–5731, 2017.

[80] H. Madupalli, B. Pavan, and M. M. J. Tecklenburg. Carbonate substitution in the mineral component of bone: Discriminating the structural changes, simultaneously imposed by carbonate in A and B sites of apatite Honey. *J Solid State Chem.*, 255:27–35, 2017.

[81] Humair A. Siddiqui, Kim L. Pickering, and Michael R. Mucalo. A review on the use of hydroxyapatite- carbonaceous structure composites in bone replacement materials for strengthening purposes. *Materials*, 11(10):1–32, 2018.

[82] Hanna Isaksson, Mikael J. Turunen, Lassi Rieppo, Simo Saarakkala, Inari S. Tamminen, Jarno Rieppo, Heikki Kröger, and Jukka S. Jurvelin. Infrared spectroscopy indicates altered bone turnover and remodeling activity in renal osteodystrophy. *Journal of Bone and Mineral Research*, 25(6):1360–1366, 2010.

[83] Fay Crawford-Manning, Martha Z. Vardaki, Ellen Green, Judith R. Meakin, Claudio Vergari, Nick Stone, and C. Peter Winlove. Multiphoton imaging and Raman spectroscopy of the bovine vertebral endplate. *The Analyst*, 146:4242–4253, 2021.

[84] Janardhan S. Yerramshetty, Cora Lind, and Ozan Akkus. The compositional and physicochemical homogeneity of male femoral cortex increases after the sixth decade. *Bone*, 39(6):1236–1243, 2006.

[85] Catherine P. Tarnowski, Michael A. Ignelzi, and Michael D. Morris. Mineralization of developing mouse calvaria as revealed by raman microspectroscopy. *Journal of Bone and Mineral Research*, 17(6):1118–1126, 2002.

[86] H. Rico, M. Revilla, L. F. Villa, and M. Alvarez de Buergo. Age-related differences in total and regional bone mass: A cross-sectional study with DXA in 429 normal women. *Osteoporosis International*, 3(3):154–159, 1993.

[87] Jongseok Lee, Sungwha Lee, Sungok Jang, and Ohk Hyun Ryu. Age-Related Changes in the Prevalence of Osteoporosis according to Gender and Skeletal Site: The Korea National Health and Nutrition Examination Survey 2008-2010. *Endocrinology and Metabolism*, 28(3):180, 2013.

[88] Glen M. Blake and Ignac Fogelman. The role of DXA bone density scans in the diagnosis and treatment of osteoporosis. *Postgraduate Medical Journal*, 83(982):509–517, 2007.

[89] R. Karunanithi, S. Ganesan, T. M. R. Panicker, M. Paul Korath, and K. Jagadeesan. Assessment of bone mineral density by DXA and the trabecular microarchitecture of the calcaneum by texture analysis in pre- and postmenopausal women in the evaluation of osteoporosis. *Journal of Medical Physics*, 32(4):161–168, 2007.

[90] A. Tang and Varacello M. *Anatomy, Shoulder and Upper Limb, Hand Carpal Bones*. StatPearls Publishing, Treasure Island (FL), 2022.

[91] A. A. Altalib, K. H. Miao, and R. G. Menezes. *Anatomy, Thorax, Sternum*. StatPearls Publishing, Treasure Island (FL), 2022.

[92] B. W. Anderson, Kortz M. W., and K. A. Kharazi. *Anatomy, Head and Neck, Skull*. StatPearls Publishing, Treasure Island (FL), 2022.

[93] Bart Clarke. Normal bone anatomy and physiology. *Clinical journal of the American Society of Nephrology*, 3(Suppl 3):131–139, 2008.

[94] S. Bakbak, R. Kayacan, and O. Akkus. Effect of collagen fiber orientation on mechanical properties of cortical bone. *Journal of Biomechanics*, 44(Suppl. 1), 2011.

[95] Susan M. Ott. Cortical or Trabecular Bone: What's the Difference? *American Journal of Nephrology*, 47(6):373–375, 2018.

[96] Ramin Oftadeh, Miguel Perez-Viloria, Juan C. Villa-Camacho, Ashkan Vaziri, and Ara Nazarian. Biomechanics and Mechanobiology of Trabecular Bone: A Review. *Journal of Biomechanical Engineering*, 137(1):1–15, 2015.

[97] Natalie Reznikov, Ron Shahar, and Steve Weiner. Three-dimensional structure of human lamellar bone: The presence of two different materials and new insights into the hierarchical organization. *Bone*, 59:93–104, 2014.

[98] J. D. Currey. *Bones: Structure and Mechanics*. Princeton University Press, 2002.

[99] Frederic Shapiro and J. Y. Wu. Woven bone overview: Structural classification based on its integral role in developmental, repair and pathological bone formation throughout vertebrate groups. *European Cells and Materials*, 38:137–167, 2019.

[100] Riaz Akhtar, M. R. Daymond, J. D. Almer, and P. M. Mummery. Load transfer in bovine plexiform bone determined by synchrotron x-ray diffraction. *Journal of Materials Research*, 23(2):543–550, 2008.

[101] A. Ascenzi, E. Bonucci, and D. S. Bocciarelli. An electron microscope study on primary periosteal bone. *Journal of Ultrasructure Research*, 18(5-6):605–618, 1967.

[102] J. D. Currey. The many adaptations of bone. *Journal of Biomechanics*, 36(10):1487–1495, 2003.

[103] Alan Boyde. The Bone Cartilage Interface and Osteoarthritis. *Calcified Tissue International*, 109(3):303–328, 2021.

[104] Rebecca M. Hoerth, Michael Kerschnitzki, Marta Aido, Ingo Schmidt, Manfred Burghammer, Georg N. Duda, Peter Fratzl, Bettina M. Willie, and Wolfgang Wagermaier. Correlations between nanostructure and micromechanical properties of healing bone. *Journal of the Mechanical Behavior of Biomedical Materials*, 77:258–266, 2018.

[105] Jennifer A. McKenzie and Matthew J. Silva. Comparing histological, vascular and molecular responses associated with woven and lamellar bone formation induced by mechanical loading in the rat ulna. *Bone*, 48(2):250–258, 2011.

[106] Hayley M. Britz, C. David L Thomas, John G. Clement, and David M. L. Cooper. The relation of femoral osteon geometry to age, sex, height and weight. *Bone*, 45(1):77–83, 2009.

[107] Marco Zedda and Ramona Babosova. Does the osteon morphology depend on the body mass? A scaling study on macroscopic and histomorphometric differences between cow (Bos taurus) and sheep (Ovis aries). *Zoomorphology*, 140(1):169–181, 2021.

[108] Desiré Brits, Maryna Steyn, and Ericka Noelle L'Abbé. A histomorphological analysis of human and non-human femora. *International Journal of Legal Medicine*, 128(2):369–377, 2014.

[109] A. A. Felder, C. Phillips, H. Cornish, M. Cooke, J. R. Hutchinson, and M. Doube. Secondary osteons scale allometrically in mammalian humerus and femur. *Royal Society Open Science*, 4(11), 2017.

[110] Susan Pfiffer, Christian Crowder, Lesley Harrington, and Michael Brown. Secondary Osteon and Haversian Canal Dimensionsas Behavioral Indicators. *American Journal of Physical Anthropology*, 131(4):460–468, 2006.

[111] Suzanna Michener, Lynne S. Bell, Nadine C. Schuurman, and David Swanlund. A Method to Interpolate Osteon Volume Designed for Histological Age Estimation Research. *Journal of Forensic Sciences*, 65(4):1247–1259, 2020.

[112] Paola Castrogiovanni, Rosa Imbesi, Marco Fisichella, and Venera Mazzone. Osteonic organization of limb bones in mammals, including humans, and birds: a preliminary study Paola. *Italian Journal of Anatomy and Embryology*, 116(1):30–37, 2010.

[113] David M. L. Cooper, C. David L. Thomas, John G. Clement, and Benedikt Hallgrímsson. Three-dimensional microcomputed tomography imaging of basic multicellular unit-related resorption spaces in human cortical bone.

Anatomical Record - Part A Discoveries in Molecular, Cellular, and Evolutionary Biology, 288(7):806–816, 2006.

[114] Harold M. Frost and Webster S. S. Jee. Perspectives: A vital biomechanical model of the endochondral ossification mechanism. *The Anatomical Record*, 240(4):435–446, 1994.

[115] Donna J. Cech and Suzanne “Tink” Martin. Chapter 6 - skeletal system changes. In *Functional Movement Development Across the Life Span*, pages 105–128. W.B. Saunders, Saint Louis, third edition, 2012.

[116] Ola Nilsson, Rose Marino, Francesco De Luca, Moshe Phillip, and Jeffrey Baron. Endocrine regulation of the growth plate. *Hormone Research*, 64(4):157–165, 2005.

[117] B. C. J. Van Der Eerden, M. Karperien, and J. M. Wit. Systemic and Local Regulation of the Growth Plate. *Endocrine Reviews*, 24(6):782–801, 2003.

[118] Kye Shik Shim. Pubertal growth and epiphyseal fusion. *Annals of Pediatric Endocrinology Metabolism*, 20(1):8, 2015.

[119] G. Breeland, M. A. Sinkler, and Menezes R. G. *Embryology, Bone Ossification*. StatPearls Publishing, Treasure Island (FL), 2022.

[120] Arkady Rutkovskiy, Kåre-Olav Stensløkken, and Ingvar Jarle Vaage. Osteoblast Differentiation at a Glance. *Medical Science Monitor Basic Research*, 22:95–106, 2016.

[121] Sarah L. Dallas and Lynda F. Bonewald. Dynamics of the Transition from Osteoblast to Osteocyte Sarah. *Ann N Y Acad Sci.*, 1192(1):437–443, 2010.

[122] Margit Pavelka and Jürgen Roth. *Articular Cartilage*, pages 294–295. Springer Vienna, Vienna, 2010.

[123] E. Çiçek and A. Arikanoğlu. Morphological variations of chondrocytes in bovine articular cartilage using confocal laser scanning microscopy. *Acta Physica Polonica A*, 125(4):898–901, 2014.

[124] B. McKibbin and F. W. Holdsworth. The nutrition of immature joint cartilage in the lamb. *The Journal of bone and joint surgery. British volume*, 48(4):793–803, 1966.

[125] Alice J. Sophia Fox, Asheesh Bedi, and Scott A. Rodeo. The basic science of articular cartilage: Structure, composition, and function. *Sports Health*, 1(6):461–468, 2009.

[126] Jessica Mansfield. *Multi-photon microscopy of cartilage*. PhD thesis, University of Exeter, 2008.

[127] Rebecca Lewis, Claire H. Feetham, and Richard Barrett-Jolley. Biochemistry Cell Volume Regulation in Chondrocytes. *Cellular Physiology and Biochemistry*, 28:1111–1122, 2011.

[128] Yuze Wang, Lei Wei, Lingyuan Zeng, Dongdong He, and Xiaochun Wei. Nutrition and degeneration of articular cartilage. *Knee Surgery, Sports Traumatology, Arthroscopy*, 21(8):1751–1762, 2013.

[129] C. Anthony Poole, Michael H. Flint, and Brent W. Beaumont. Chondrons in cartilage: Ultrastructural analysis of the pericellular microenvironment in adult human articular cartilages. *Journal of Orthopaedic Research*, 5(4):509–522, 1987.

[130] C. Anthony Poole. Articular cartilage chondrons: Form, function and failure. *Journal of Anatomy*, 191(1):1–13, 1997.

[131] G. M. Lee, C. A. Poole, S. S. Kelley, J. Chang, and B. Caterson. Isolated chondrons: A viable alternative for studies of chondrocyte metabolism in vitro. *Osteoarthritis and Cartilage*, 5(4):261–274, 1997.

[132] Zhenxing Zhao, Yifei Li, Mengjiao Wang, Sen Zhao, Zhihe Zhao, and Jie Fang. Mechanotransduction pathways in the regulation of cartilage chondrocyte homoeostasis. *Journal of Cellular and Molecular Medicine*, 24(10):5408–5419, 2020.

[133] Alfred Benninghoff. Form und Bau der Gelenkknorpel in ihren Beziehungen zur Funktion. *Zeitschrift für Anatomie und Entwicklungsgeschichte*, 76(1-3):43–63, 1925.

[134] Farshid Guilak. The deformation behavior and viscoelastic properties of chondrocytes in articular cartilage. *Biorheology*, 37(1-2):27–44, 2000.

[135] Bac V. Nguyen, Qiguang Wang, Nicola J. Kuiper, Alicia J. El Haj, Colin R. Thomas, and Zhibing Zhang. Strain-dependent viscoelastic behaviour and rupture force of single chondrocytes and chondrons under compression. *Biotechnology Letters*, 31(6):803–809, 2009.

[136] Bac V. Nguyen, Qi Guang Wang, Nicola J. Kuiper, Alicia J. El Haj, Colin R. Thomas, and Zhibing Zhang. Biomechanical properties of single chondrocytes and chondrons determined by micromanipulation and finite-element modelling. *Journal of the Royal Society Interface*, 7(53):1723–1733, 2010.

[137] Farshid Guilak, Leonidas G. Alexopoulos, Maureen L. Upton, Inchan Youn, Jae Bong Choi, Li Cao, Lori A. Setton, and Mansoor A. Haider. The pericellular matrix as a transducer of biomechanical and biochemical signals in articular cartilage. *Annals of the New York Academy of Sciences*, 1068(1):498–512, 2006.

[138] Hemanth Akkiraju and Anja Nohe. Role of chondrocytes in cartilage formation, progression of osteoarthritis and cartilage regeneration. *Journal of Developmental Biology*, 3(4):177–192, 2015.

[139] Massimo Bottini, Saida Mebarek, Karen L. Anderson, Agnieszka Strzelecka-Kiliszek, Lukasz Bozycki, Ana Maria Sper Simão, Maytê Bolean, Pietro Ciancaglini, Joanna B. Pikula, Slawomir Pikula, David Magne, Niels Volkmann, Dorit Hanein, José Luis Millán, and Rene Buchet. Matrix vesicles from chondrocytes and osteoblasts: their biogenesis, properties, functions and biomimetic models. *Biochim Biophys Acta.*, 1862(3):532–546, 2018.

[140] Aviral Vatsa, Roel G. Breuls, Cornelis M. Semeins, Philip L. Salmon, Theo H. Smit, and Jenneke Klein-Nulend. Osteocyte morphology in fibula and calvaria - Is there a role for mechanosensing? *Bone*, 43(3):452–458, 2008.

[141] Gastone Marotti. Osteocyte orientation in human lamellar bone and its relevance to the morphometry of periosteocytic lacunae. *Metabolic Bone Disease and Related Research*, 1(4):325–333, 1979.

[142] Jun Qiu, Andrew D. Baik, X. Lucas Lu, Elizabeth M.C. Hillman, Zhuo Zhuang, Cheng Dong, and X. Edward Guo. A noninvasive approach to

determine viscoelastic properties of an individual adherent cell under fluid flow. *Journal of Biomechanics*, 47(6):1537–1541, 2014.

[143] Rommel G. Bacabac, Daisuke Mizuno, Christoph F. Schmidt, Fred C. MacKintosh, Jack J.W.A. Van Loon, Jenneke Klein-Nulend, and Theo H. Smit. Round versus flat: Bone cell morphology, elasticity, and mechanosensing. *Journal of Biomechanics*, 41(7):1590–1598, 2008.

[144] René F. M. van Oers, Hong Wang, and Rommel G. Bacabac. Osteocyte Shape and Mechanical Loading. *Current Osteoporosis Reports*, 13(2):61–66, 2015.

[145] Ruud P. van Hove, Peter A. Nolte, Aviral Vatsa, Cornelis M. Semeins, Philip L. Salmon, Theo H. Smit, and Jenneke Klein-Nulend. Osteocyte morphology in human tibiae of different bone pathologies with different bone mineral density - Is there a role for mechanosensing? *Bone*, 45(2):321–329, 2009.

[146] Pascal R. Buenzli and Natalie A. Sims. Quantifying the osteocyte network in the human skeleton. *Bone*, 75:144–150, 2015.

[147] E. Owen. Bone as a Mineral Reserve. *British Journal of Nutrition*, 6(1):415–423, 1952.

[148] Harold D. Copp and S. Shim. The Homeostatic Function of Bone as a Mineral Reservoir. *Oral Surgery, Oral Medicine, Oral Pathology*, 16(6):738–744, 1963.

[149] Vittorio Sansalone, Joanna Kaiser, Salah Naili, and Thibault Lemaire. Interstitial fluid flow within bone canaliculi and electro-chemo-mechanical

features of the canalicular milieu: A multi-parametric sensitivity analysis. *Biomechanics and Modeling in Mechanobiology*, 12(3):533–553, 2013.

[150] K. Piekarski and M. Munro. Transport Mechanism Operating Between Blood Supply and Osteocytes in Long Bones. *Nature*, 269:80–82, 1977.

[151] Susannah P. Fritton and Sheldon Weinbaum. Fluid and Solute Transport in Bone Flow Induced. *Annu Rev Fluid Mech*, 1(41):347–374, 2009.

[152] Liyun Wang. Solute Transport in the Bone Lacunar-Canalicular System (LCS). *Curr Osteoporos Rep*, 16(1):32–41, 2018.

[153] S. C. Cowin. Mechanosensation and fluid transport in living bone. *Journal of Musculoskeletal Neuronal Interactions*, 2(3):256–260, 2002.

[154] Toshihisa Komori. Functions of the osteocyte network in the regulation of bone mass. *Cell Tissue Res*, 352:191–198, 2013.

[155] Haniyeh Hemmatian, Astrid D. Bakker, Jenneke Klein-Nulend, and G. Harry van Lenthe. Aging, Osteocytes, and Mechanotransduction. *Current Osteoporosis Reports*, 15(5):401–411, 2017.

[156] S. Sanchez, P. Tafforeau, F. Di Rocco, J. Olivier, D. Bresch, V. Calvez, P. Vigneaux, A. Ohazama, P. Corre, P. E. Ahlberg, R. H. Khonsari, and P. T. Sharpe. A mathematical model for mechanotransduction at the early steps of suture formation. *Proceedings of the Royal Society B: Biological Sciences*, 280(1759):20122670–20122670, 2013.

[157] P. J. Prendergast and R. Huiskes. Microdamage and osteocyte-lacuna strain in bone: A microstructural finite element analysis. *Journal of Biomechanical Engineering*, 118(2):240–246, 1996.

[158] Barbara R. McCreadie, Scott J. Hollister, Mitchell B. Schaffler, and Steven A. Goldstein. Osteocyte lacuna size and shape in women with and without osteoporotic fracture. *Journal of Biomechanics*, 37(4):563–572, 2004.

[159] Thibault Lemaire, Salah Naili, and Vittorio Sansalone. Multiphysical modelling of fluid transport through osteo-articular media. *Anais da Academia Brasileira de Ciencias*, 82(1):127–144, 2010.

[160] G. Marotti. The osteocyte as a wiring transmission system. *J Musculoskel Neuron Interact*, 1:133–136, 2000.

[161] Carla Palumbo and Marzia Ferretti. The osteocyte: From “prisoner” to “orchestrator”. *Journal of Functional Morphology and Kinesiology*, 6(28), 2021.

[162] Sy Giin Chong, Seidai Sato, Martin Kolb, and Jack Gauldie. Fibrocytes and fibroblasts—Where are we now. *International Journal of Biochemistry and Cell Biology*, 116, 2019.

[163] John L. Rinn, Chanda Bondre, Hayes B. Gladstone, Patrick O. Brown, and Howard Y. Chang. Anatomic demarcation by positional variation in fibroblast gene expression programs. *PLoS Genetics*, 2(7):1084–1096, 2006.

[164] Howard Y. Chang, Jen Tsan Chi, Sandrine Dudoit, Chanda Bondre, Matt Van De Rijn, David Botstein, and Patrick O. Brown. Diversity, topographic differentiation, and positional memory in human fibroblasts. *Proceedings of the National Academy of Sciences of the United States of America*, 99(20):12877–12882, 2002.

[165] Han Liu, Mian Wu, Yuanbo Jia, Lele Niu, Guoyou Huang, and Feng Xu. Control of fibroblast shape in sequentially formed 3D hybrid hydrogels regulates cellular responses to microenvironmental cues. *NPG Asia Materials*, 12(1), 2020.

[166] Victor J. Thannickal, Yong Zhou, Amit Gaggar, and Steven R. Duncan. Fibrosis: Ultimate and proximate causes. *Journal of Clinical Investigation*, 124(11):4673–4677, 2014.

[167] M. Zeisberg and R. Kalluri. Cellular mechanisms of tissue fibrosis.1.Common and organ-specific mechanisms associated with tissue fibrosis. *Am. J. Physiol. Cell Physio.*, 303(3), 2013.

[168] Mirko D'Urso and Nicholas A. Kurniawan. Mechanical and Physical Regulation of Fibroblast–Myofibroblast Transition: From Cellular Mechanoresponse to Tissue Pathology. *Frontiers in Bioengineering and Biotechnology*, 8:1–15, 2020.

[169] Geer Tian and Tanchen Ren. Mechanical stress regulates the mechanotransduction and metabolism of cardiac fibroblasts in fibrotic cardiac diseases. *European Journal of Cell Biology*, 102(2), 2023.

[170] David Bassen, Mingkun Wang, Duc Pham, Shuofei Sun, Rashmi Rao, Rishabh Singh, and Jonathan Butcher. Hydrostatic mechanical stress regulates growth and maturation of the atrioventricular valve. *The Company of Biologists*, 148, 2021.

[171] Guan Li, Wei Liang, Pengbing Ding, and Zhenmin Zhao. Sutural fibroblasts exhibit the function of vascular endothelial cells upon mechanical strain. *Archives of Biochemistry and Biophysics*, 712, 2021.

[172] Diana Corallo, Valeria Trapani, and Paolo Bonaldo. The notochord: Structure and functions. *Cellular and Molecular Life Sciences*, 72(16):2989–3008, 2015.

[173] Irving M. Shapiro and Makarand V. Risbud. *The intervertebral disc*. 2019.

[174] Wilson C. W. Chan, Tiffany Y. K. Au, Vivian Tam, Kathryn S. E. Cheah, and Danny Chan. Coming together is a beginning: The making of an intervertebral disc. *Birth Defects Research Part C - Embryo Today: Reviews*, 102(1):83–100, 2014.

[175] Worawat Limthongkul, Eldin E. Karaikovic, Jason W. Savage, and Alexander Markovic. Volumetric analysis of thoracic and lumbar vertebral bodies. *Spine Journal*, 10(2):153–158, 2010.

[176] N. G. Hendry. The hydration of the nucleus pulposus and its relation to intervertebral disc derangement. *The Journal of bone and joint surgery. British volume*, 40 B(1):132–144, 1958.

[177] Darwesh M. K. Aladin, Kenneth M. C. Cheung, Alfonso H. W. Ngan, Danny Chan, Victor Y. L. Leung, Chwee Teck Lim, Keith D. K. Luk, and William W. Lu. Nanostructure of collagen fibrils in human nucleus pulposus and its correlation with macroscale tissue mechanics. *Journal of Orthopaedic Research*, 28(4):497–502, 2010.

[178] Sara Molladavoodi, John McMorran, and Diane Gregory. Mechanobiology of annulus fibrosus and nucleus pulposus cells in intervertebral discs. *Cell and Tissue Research*, 379(3):429–444, 2020.

[179] Adam H. Hsieh and Julianne D. Twomey. Cellular mechanobiology of the intervertebral disc: New directions and approaches. *Journal of Biomechanics*, 43(1):137–145, 2010.

[180] G. A. Holzapfel, C. A. J. Schulze-Bauer, G. Feigl, and P. Regitnig. Single lamellar mechanics of the human lumbar anulus fibrosus. *Biomechanics and Modeling in Mechanobiology*, 3(3):125–140, 2005.

[181] David R. Eyre and Helen Muir. Collagen polymorphism: two molecular species in pig intervertebral disc. *FEBS Lett.*, 42(2):192–196, 1974.

[182] David R. Eyre and Helen Muir. Quantitative analysis of types I and II collagens in human intervertebral discs at various ages. *BBA - Protein Structure*, 492(1):29–42, 1977.

[183] Claudio Vergari, Jessica Mansfield, Judith R. Meakin, and Peter C. Winlove. Lamellar and fibre bundle mechanics of the annulus fibrosus in bovine intervertebral disc. *Acta Biomaterialia*, 37:14–20, 2016.

[184] Andrea Malandrino, Josep A. Planell, and Damien Lacroix. Statistical factorial analysis on the poroelastic material properties sensitivity of the lumbar intervertebral disc under compression, flexion and axial rotation. *Journal of Biomechanics*, 42(16):2780–2788, 2009.

[185] Clayton Adam, Philippe Rouch, and Wafa Skalli. Inter-lamellar shear resistance confers compressive stiffness in the intervertebral disc: An image-based modelling study on the bovine caudal disc. *Journal of Biomechanics*, 48(16):4303–4308, 2015.

[186] N. Newell, J. P. Little, A. Christou, M. A. Adams, C. J. Adam, and S. D. Masouros. Biomechanics of the human intervertebral disc: A review of testing techniques and results. *Journal of the Mechanical Behavior of Biomedical Materials*, 69:420–434, 2017.

[187] K. B. Broberg. On the Mechanical Behaviour of Intervertebral Discs. *Spine*, 8(2):151–165, 1983.

[188] Beth G. Ashinsky, Edward D. Bonnevie, Sai A. Mandalapu, Stephen Pickup, Chao Wang, Lin Han, Robert L. Mauck, Harvey E. Smith, and Sarah E. Gullbrand. Intervertebral Disc Degeneration Is Associated With Aberrant Endplate Remodeling and Reduced Small Molecule Transport. *Journal of Bone and Mineral Research*, 35(8):1572–1581, 2020.

[189] Samantha A. Rodrigues, Kelly R. Wade, Ashvin Thambyah, and Neil D. Broom. Micromechanics of annulus-end plate integration in the intervertebral disc. *Spine Journal*, 12(2):143–150, 2012.

[190] Sharon Brown, Samantha Rodrigues, Christopher Sharp, Kelly Wade, Neil Broom, Iain W. McCall, and Sally Roberts. Staying connected: structural integration at the intervertebral disc–vertebra interface of human lumbar spines. *European Spine Journal*, 26(1):248–258, 2017.

[191] Helen E. Gruber, Nomaan Ashraf, Jeremy Kilburn, Cliff Williams, H. James Norton, Brian E. Gordon, and Edward N. Hanley. Vertebral endplate architecture and vascularization: Application of micro-computerized tomography, a vascular tracer, and immunocytochemistry in analyses of disc degeneration in the aging sand rat. *Spine*, 30(23):2593–2600, 2005.

[192] Yuanqiao Wu, Johnfredy Loaiza, Rohin Banerji, Olivia Blouin, and Elise Morgan. Structure-function relationships of the human vertebral endplate. *JOR Spine*, 4(3):1–13, 2021.

[193] Sara L. Sampson, Meghan Sylvia, and Aaron J. Fields. Effects of Dynamic Loading on Solute Transport Through the Human Cartilage Endplate. *J Biomech*, 83:273–279, 2019.

[194] Uruj Zehra, Kate Robson-Brown, Michael A. Adams, and Patricia Dolan. Porosity and thickness of the vertebral endplate depend on local mechanical loading. *Spine*, 40(15):1173–1180, 2015.

[195] Azucena G. Rodriquez, Chloe K. Slichter, Frank L. Acosta, Ana E. Rodriguez-Soto, Andrew J. Burghardt, Sharmila Majumdar, and Jeffrey C. Lotz. Human Disc Nucleus Properties and Vertebral Endplate Permeability. *Spine*, 36(7):512–520, 2011.

[196] J. P. G. Urban, S. Holm, and A. Maroudas. Diffusion of Small Solutes into the Intervertebral Disc: As In Vivo Study. *Bior*, 15(3):203–223, 1978.

[197] Norbert Boos, Ake Wallin, Thomas Schmucker, Max Aebi, and Chris Boesch. Quantitative MR imaging of lumbar intervertebral discs and vertebral bodies: Methodology, reproducibility, and preliminary results. *Magnetic Resonance Imaging*, 12(4):577–587, 1994.

[198] Lorin M. Benneker, Paul F. Heini, Mauro Alini, Suzanne E. Anderson, and Keita Ito. 2004 Young investigator award winner: Vertebral endplate marrow contact channel occlusions and intervertebral disc degeneration. *Spine*, 30(2):167–173, 2005.

[199] Lorraine S. Symington. Human Cartilage Endplate Permeability Varies with Degeneration and Intervertebral Disc Site. *J. Biomech*, 49(4):550–557, 2016.

[200] Ruth S. Ochia, Allan F. Tencer, and Randal P. Ching. Effect of loading rate on endplate and vertebral body strength in human lumbar vertebrae. *Journal of Biomechanics*, 36(12):1875–1881, 2003.

[201] Patricia Dolan, Jin Luo, Phillip Pollintine, Priyan R. Landham, Manos Stefanakis, and Michael A. Adams. Intervertebral Disc Decompression Following Endplate Damage. *Spine*, 38(17):1473–1481, 2013.

[202] Britta Berg-Johansen, Aaron J. Fields, Ellen C. Liebenberg, Alfred Li, and Jeffrey C. Lotz. Structure-function relationships at the human spinal disc-vertebra interface. *Journal of Orthopaedic Research*, 36(1):192–201, 2018.

[203] Fay Manning. *The vertebral endplate: its structure and function*. PhD thesis, University of Exeter, 2019.

[204] Irving M. Shapiro, Edward J. Vresilovic, and Makarand V. Risbud. Is the spinal motion segment a diarthrodial polyaxial joint: What a nice nucleus like you doing in a joint like this? *Bone*, 50(3):771–776, 2012.

[205] Christian Balkovec, Michael A. Adams, Patricia Dolan, and Stuart M. Mcgill. Annulus Fibrosus Can Strip Hyaline Cartilage End Plate from Subchondral Bone : A Study of the Intervertebral Disk in Tension. *Global Spine Journal*, 5:360–365, 2015.

[206] Samantha A. Rodrigues, Ashvin Thambyah, and Neil D. Broom. A multiscale structural investigation of the annulus-endplate anchorage system and its mechanisms of failure. *Spine Journal*, 15(3):405–416, 2015.

[207] T. P. Green, M. A. Adams, and P. Dolan. Tensile properties of the annulus fibrosus - II. Ultimate tensile strength and fatigue life. *European Spine Journal*, 2(4):209–214, 1993.

[208] H. S. Gupta, S. Schratter, W. Tesch, P. Roschger, A. Berzlanovich, T. Schoeberl, K. Klaushofer, and P. Fratzl. Two different correlations between nanoindentation modulus and mineral content in the bone-cartilage interface. *Journal of Structural Biology*, 149:138–148, 2005.

[209] Magdalena Wojtków, Maciej Głowacki, and Celina Pezowicz. Multiscale structural characterization of the vertebral endplate in animal models. *Journal of Anatomy*, 239(1):70–80, 2021.

[210] Hila May, Nili Steinberg, Bahaa Medlej, Gali Dar, Youssef Masharawi, Israel Hershkovitz, Nathan Peled, and Smadar Peleg. The Epiphyseal Ring. *Spine*, 36(11):850–856, 2011.

[211] Munetaka Iwata, Wataru Yamamoto, Takasumi Shimomoto, Yuki Okada, Satomi Oosawa, Daishiro Miura, and Yasushi Hara. Persistence of vertebral growth plate cartilage in aged cynomolgus monkeys. *Journal of Toxicologic Pathology*, 31(2):151–154, 2018.

[212] Ian A. F. Stokes and Luke Windisch. Vertebral height growth predominates over intervertebral disc height growth in adolescents with scoliosis. *Spine (Phila Pa 1976)*, 31(14):1600–1604, 2006.

[213] J. R. Taylor. Growth of human intervertebral discs and vertebral bodies. *Journal of anatomy*, 120(Pt 1):49–68, 1975.

[214] Yejia Zhang, Brett A. Lenart, Joseph K. Lee, Ding Chen, Peng Shi, Jing Ren, Carol Muehleman, and Howard S. An. Histological features of endplates of the mammalian spine: From mice to men. *Spine*, 39(5):1–14, 2014.

[215] Yue Wang, Michele C. Battié, Steven K. Boyd, and Tapio Videman. The osseous endplates in lumbar vertebrae: Thickness, bone mineral density and their associations with age and disk degeneration. *Bone*, 48(4):804–809, 2011.

[216] S. Roberts, I. W. McCall, J. Menage, M. J. Haddaway, and S. M. Eisenstein. Does the thickness of the vertebral subchondral bone reflect the composition of the intervertebral disc? *European Spine Journal*, 6(6):385–389, 1997.

[217] F. D. Zhao, P. Pollintine, B. D. Hole, M. A. Adams, and P. Dolan. Vertebral fractures usually affect the cranial endplate because it is thinner and supported by less-dense trabecular bone. *Bone*, 44(2):372–379, 2009.

[218] Li Yang Dai, Xiang Yang Wang, Chen Guang Wang, Lei Sheng Jiang, and Hua Zi Xu. Bone mineral density of the thoracolumbar spine in relation to burst fractures: A quantitative computed tomography study. *European Spine Journal*, 15(12):1817–1822, 2006.

[219] F. Magerl, M. Aebi, S. D. Gertzbein, J. Harms, and S. Nazarian. A comprehensive classification of thoracic and lumbar injuries. *European Spine Journal*, 3(4):184–201, 1994.

[220] A. Nachemson, T. Lewin, A. Maroudas, and Freeman M. A. In vitro diffusion of dye through the end-plates and the annulus fibrosus of human lumbar inter-vertebral discs. *Acta Orthop Scand.*, 41(6):589–607, 1970.

[221] Rachel C. Paietta, Evalina L. Burger, and Virginia L. Ferguson. Mineralization and collagen orientation throughout aging at the vertebral endplate in the human lumbar spine. *Journal of Structural Biology*, 184(2):310–320, 2013.

[222] E. Ellis and C. H. Bachman. Fluorescence of Bone. *Nature*, 206:1328–1331, 1965.

[223] Mohamed A. H. Swaraldahab and Angi M. Christensen. The Effect of Time on Bone Fluorescence: Implications for Using Alternate Light Sources to Search for Skeletal Remains. *Journal of Forensic Sciences*, 61(2):442–444, 2016.

[224] E. F. Johnson, K. Chetty, I. M. Moore, A. Stewart, and W. Jones. The distribution and arrangement of elastic fibres in the intervertebral disc of the adult human. *Journal of anatomy*, 135(Pt 2):301–9, 1982.

[225] S. Yu, V. M. Haughton, K. L. Lynch, K. C. Ho, and L. A. Sether. Fibrous structure in the intervertebral disk: Correlation of MR appearance with anatomic sections. *American Journal of Neuroradiology*, 10(5):1105–1110, 1989.

[226] Magdalena Müller-Gerbl, Stefan Weißer, and Ulrich Linsenmeier. The distribution of mineral density in the cervical vertebral endplates. *European Spine Journal*, 17(3):432–438, 2008.

[227] I. Zizak, P. Roschger, O. Paris, B. M. Misof, A. Berzlanovich, S. Bernstorff, H. Amenitsch, K. Klaushofer, and P. Fratzl. Characteristics of mineral particles in the human bone/cartilage interface. *Journal of Structural Biology*, 141(3):208–217, 2003.

[228] Sung Won Jin, Ki Bum Sim, and Sang Dae Kim. Development and growth of the normal cranial vault: An embryologic review. *Journal of Korean Neurosurgical Society*, 59(3):192–196, 2016.

[229] Jeremy J. Mao, Xin Wang, Mark P. Mooney, Ross A. Kopher, and James A. Nudera. Strain Induced Osteogenesis of the Craniofacial Suture Upon Controlled Delivery of Low-Frequency Cyclic Forces. *Frontiers in Bioscience*, 8:10–17, 2003.

[230] Claudia Corega, Ligia Vaida, Ioana Tiberia Iliaş, D. Bertossi, and Ionela Teodora Dascălu. Cranial sutures and diploae morphology. *Romanian Journal of Morphology and Embryology*, 54(4):1157–1160, 2013.

[231] Heather E. White, Anjali Goswami, and Abigail S. Tucker. The Intertwined Evolution and Development of Sutures and Cranial Morphology. *Frontiers in Cell and Developmental Biology*, 9:1–20, 2021.

[232] Susan W. Herring. Sutures - a tool in functional cranial analysis. *Acta Anat.*, 83:222–247, 1972.

[233] M. Turgut, R. S. Tubbs, A. T. Turgut, and A. S. Dumont. *The Sutures of the Skull*. Springer, 2021.

[234] Richard J. Huggins, Mark E. Freeman, Jeffrey B. Kerr, and Bryan C. Mendelson. Histologic and ultrastructural evaluation of sutures used for

surgical fixation of the SMAS. *Aesthetic Plastic Surgery*, 31(6):719–724, 2007.

[235] Z. Q. Zhang and J. L. Yang. Biomechanical dynamics of cranial sutures during simulated impulsive loading. *Applied Bionics and Biomechanics*, 2015, 2015.

[236] Rosanna C. Sabini and David E. Elkowitz. Significance of differences in patency among cranial sutures. *Journal of the American Osteopathic Association*, 106(10):600–604, 2006.

[237] Vincent G. Kokich. Age changes in the human frontozygomatic suture from 20 to 95 years. *American Journal of Orthodontics*, 69(4):411–430, 1976.

[238] Melvin L. Moss. Experimental Alteration Of Sutural Area Morphology. *The Anatomical Record*, 127(3):497–633, 1957.

[239] Kelly Nicole Adamski, Andre Matthew Loyd, Albert Samost, Barry Myers, Roger Nightingale, Kathleen Smith, and Cameron R. Dale' Bass. Pediatric Coronal Suture Fiber Alignment and the Effect of Interdigitation on Coronal Suture Mechanical Properties. *Annals of Biomedical Engineering*, 43(9):2101–2111, 2015.

[240] Takashi Miura, Chad A. Perlyn, Masato Kinboshi, Naomichi Ogihara, Mikiko Kobayashi-Miura, Gillian M. Morriss-Kay, and Kohei Shiota. Mechanism of skull suture maintenance and interdigitation. *Journal of Anatomy*, 215(6):642–655, 2009.

[241] Lex A. Mitchell, C. A. Kitley, T. L. Armitage, M. V. Krasnokutsky, and V. J. Rooks. Normal sagittal and coronal suture widths by using CT imaging. *American Journal of Neuroradiology*, 32(10):1801–1805, 2011.

[242] Giap H. Vu, Wen Xu, Beatrice C. Go, Laura S. Humphries, Christopher L. Kalmar, Jesse A. Taylor, Scott P. Bartlett, Arastoo Vossough, Hyun-Duck Nah-Cederquist, and Jordan W. Swanson. Physiologic Timeline of Cranial-Base Suture and Synchondrosis Closure. *Plastic and Reconstructive Surgery*, 128(6):973–982, 2021.

[243] C. Corbett Wilkinson, Nicholas V. Stence, Cesar A. Serrano, Sarah J. Graber, Lígia Batista-Silverman, Emily Schmidt-Beuchat, and Brooke M. French. Fusion patterns of major calvarial sutures on volume-rendered CT reconstructions. *Journal of Neurosurgery: Pediatrics*, 25(5):519–528, 2020.

[244] S. V. Khandare, S. S. Bhise, and A. B. Shinde. Age estimation from cranial sutures: CT scan study. *Indian Journal of Basic and Applied Medical Research*, 3(4):203–211, 2014.

[245] S. V. Khandare, S. S. Bhise, and A. B. Shinde. Age estimation from cranial sutures – a Postmortem study Original article : Age estimation from cranial sutures – a Postmortem study. *International J. of Healthcare and Biomedical Research*, 3(3):192–202, 2015.

[246] Gagandeep Kalsi, Amandeep Singh, and Dasari Harish. Macroscopic Study of Temporoparietal Suture Closure at Autopsy for Estimation of Age. *Journal of Clinical and Diagnostic Research*, 16(1):1–4, 2022.

[247] Jacques Van Der Meulen. Metopic synostosis. *Child's Nervous System*, 28(9):1359–1367, 2012.

[248] Hugh L. Vu, Jayesh Panchel, Ellen E. PArker, Norman S. Levine, and Paul Francel. The Timing of Physiologic Closure of the Metopic Suture: A Review of 159 Patients Using Reconstructed 3D CT Scans of the Craniofacial Region. *Journal of Craniofacial Surgery*, 12(6):527–532, 2001.

[249] R. H. Khonsari, J. Olivier, P. Vigneaux, S. Sanchez, P. Tafforeau, P. E. Ahlberg, F. Di Rocco, D. Bresch, P. Corre, A. Ohazama, P. T. Sharpe, and V. Calvez. A mathematical model for mechanotransduction at the early steps of suture formation. *Proceedings of the Royal Society B: Biological Sciences*, 280(1759), 2013.

[250] Alida M. Bailleul and John R. Horner. Comparative histology of some craniofacial sutures and skull-base synchondroses in non-avian dinosaurs and their extant phylogenetic bracket. *Journal of Anatomy*, 229(2):252–285, 2016.

[251] Maria A. Katsianou, Christos Adamopoulos, Heleni Vastardis, and Efthimia K. Basdra. Signaling mechanisms implicated in cranial sutures pathophysiology: Craniosynostosis. *BBA Clinical*, 6:165–176, 2016.

[252] M. C. Meikle, Joan K. Heath, Rosalind M. Hembry, and J. J. Reynolds. Rabbit cranial suture fibroblasts under tension express a different collagen phenotype. *Archives of Oral Biology*, 27(7):609–613, 1982.

[253] A. S. Turner, J. M. Maillet, C. Mallinckrodt, and L. Cordain. Bone mineral density of the skull in premenopausal women. *Calcified Tissue International*, 61(2):110–113, 1997.

[254] Anna Paschall and Ann H. Ross. Biological sex variation in bone mineral density in the cranium and femur. *Science and Justice*, 58(4):287–291, 2018.

[255] Hans Peter Wiesmann, Lifeng Chi, Udo Stratmann, Ulrich Plate, Harald Fuchs, Ulrich Joos, and Hans J. Höhling. Sutural mineralization of rat calvaria characterized by atomic-force microscopy and transmission electron microscopy. *Cell and Tissue Research*, 294(1):93–97, 1998.

[256] Robert L. Jilka. The relevance of mouse models for investigating age-related bone loss in humans. *Journals of Gerontology - Series A Biological Sciences and Medical Sciences*, 68(10):1209–1217, 2013.

[257] Jiawen Wang, Donghua Zou, Zhengdong Li, Ping Huang, Dongri Li, Y. Shao, Huijun Wang, and Yijiu Chen. Mechanical properties of cranial bones and sutures in 1–2-year-old infants. *Medical Science Monitor*, 20:1808–1813, 2014.

[258] Mehran Moazen, Emma Peskett, Christian Babbs, Erwin Pauws, and Michael J. Fagan. Mechanical properties of calvarial bones in a mouse model for craniosynostosis. *PLoS ONE*, 10(5):1–13, 2015.

[259] P. Radhakrishnan and J. J. Mao. Nanomechanical Properties of Facial Sutures and Sutural Mineralization Front. *Journal of Dental Research*, 83(6), 2004.

[260] J. A. Buckwalter. Aging and degeneration of the human intervertebral disc. *Spine*, 20(11), 1995.

[261] John Antoniou, Thomas Steffen, Fred Nelson, Neil Winterbottom, Anthony P Hollander, Robin A Poole, Max Aebi, and Mauro Alini. The human lumbar intervertebral disc: Evidence for changes in the biosynthesis and denaturation of the extracellular matrix with growth, maturation, ageing, and degeneration. *Journal of Clinical Investigation*, 98(4):996–1003, 1996.

[262] J. P. H. J. Rutges, O. P. Jagt Van der, F. C. Oner, A. J. Verbout, R. J. M. Castelein, J. A. Kummer, H. Weinans, L. B. Creemers, and W. J. A. Dhert. Micro-CT quantification of subchondral endplate changes in intervertebral disc degeneration. *Osteoarthritis and Cartilage*, 19(1):89–95, 2011.

[263] Kwaku A. Kyere, Khoi D. Than, Anthony C. Wang, Shayan U. Rahman, Juan M. Valdivia-Valdivia, Frank La Marca, and Paul Park. Schmorl's nodes. *European Spine Journal*, 21(11):2115–2121, 2012.

[264] David Johnson and Andrew O. M. Wilkie. Craniosynostosis. *European Journal of Human Genetics*, 19(4):369–376, 2011.

[265] J. Regelsberger, P. Milovanovic, T. Schmidt, M. Hahn, E. A. Zimmermann, M. Tsokos, J. Zustin, R. O. Ritchie, M. Amling, and B. Busse. Changes to the cell, tissue and architecture levels in cranial suture synostosis reveal a problem of timing in bone development. *European Cells and Materials*, 24:441–458, 2012.

[266] Jacqueline A. C. Goos and Irene M. J. Mathijssen. Genetic causes of craniosynostosis: An update. *Molecular Syndromology*, 10(1-2):6–23, 2019.

[267] Edward P. Buchanan, Yunfeng Xue, Amy S. Xue, Asaf Olshinka, and Sandi Lam. Multidisciplinary care of craniosynostosis. *Journal of Multidisciplinary Healthcare*, 10:263–270, 2017.

[268] Peter Török and Fu-Jen Kao. *Optical Imaging and Microscopy: Techniques and Advanced Systems 2nd edition*. Springer, 2007.

[269] Amicia D. Elliott. Confocal Microscopy: Principles and Modern Practices. *Current Protocols in Cytometry*, 92(1):1–18, 2020.

[270] Florian M. Zehentbauer, Claudia Moretto, Ryan Stephen, Thangavel Thevar, John R. Gilchrist, Dubravka Pokrajac, Katherine L. Richard, and Johannes Kiefer. Fluorescence spectroscopy of Rhodamine 6G: Concentration and solvent effects. *Spectrochimica Acta - Part A: Molecular and Biomolecular Spectroscopy*, 121:147–151, 2014.

[271] E. Hecht, A. Zając, and K. Guardino. *Optics*. Addison-Wesley world student series. Addison-Wesley, 1998.

[272] R. B. Leighton and M. Sands. *Feynman Lectures on Physics Volume 2*. Addison-Wesley, 1964.

[273] Anton Ficai, Ecaterina Andronescu, Georgeta Voicu, and Denisa Ficai. Advances in collagen/hydroxyapatite composite materials. In Brahim Attaf, editor, *Advances in Composite Materials for Medicine and Nanotechnology*, chapter 1. IntechOpen, Rijeka, 2011.

[274] Philippe Réfrégier, Muriel Roche, and Sophie Brasselet. Precision analysis in polarization-resolved second harmonic generation microscopy. *Optics Letters*, 36(11):2149, 2011.

[275] Sophie Brasselet. Polarization-resolved nonlinear microscopy: application to structural molecular and biological imaging. *Advances in Optics and Photonics*, 3(3), 2011.

[276] Jessica C. Mansfield, Vipul Mandalia, Andrew Toms, C. Peter Winlove, and Sophie Brasselet. Collagen reorganization in cartilage under strain probed by polarization sensitive second harmonic generation microscopy. *Journal of the Royal Society Interface*, 16(150), 2019.

[277] Julien Duboisset, Dora Aït-Belkacem, Muriel Roche, Hervé Rigneault, and Sophie Brasselet. Generic model of the molecular orientational distribution probed by polarization-resolved second-harmonic generation. *Physical Review A - Atomic, Molecular, and Optical Physics*, 85(4):1–9, 2012.

[278] Henning Madry, C. Niek van Dijk, and Magdalena Mueller-Gerbl. The basic science of the subchondral bone. *Knee Surgery, Sports Traumatology, Arthroscopy*, 18(4):419–433, 2010.

[279] Xiaorong Wang, Feirong Xu, Yuan Fu, Huanhuan Chen, Xiang Gao, and Qiuli Huang. Traumatic vertebral fractures involve the anterior end plate more than the posterior end plate: A retrospective study. *Medicine*, 99(34), 2020.

[280] J. C. Lotz, A. J. Fields, and E. C. Liebenberg. The Role of the Vertebral End Plate in Low Back Pain. *Global Spine Journal*, 3(3):153–163, 2013.

[281] Polly Lama, Uruj Zehra, Christian Balkovec, Henry A. Claireaux, Luke Flower, Ian J. Harding, Patricia Dolan, and Michael A. Adams. Significance of cartilage endplate within herniated disc tissue. *European spine journal :*

official publication of the European Spine Society, the European Spinal Deformity Society, and the European Section of the Cervical Spine Research Society, 23(9):1869–1877, 2014.

[282] Haisheng Yang, Shashank Nawathe, Aaron J. Fields, and Tony M. Keaveny. Micromechanics of the human vertebral body for forward flexion. *Journal of Biomechanics*, 45(12):2142–2148, 2012.

[283] Haisheng Yang, Michael G Jekir, Maxwell W Davis, and Tony M Keaveny. Effective Modulus of the Human Intervertebral Disc abd its Effect on Vertebral Bone Stress. *J. Biomech.*, 49(7):1134–1140, 2017.

[284] R. J. Moore. The vertebral end-plate: What do we know? *European Spine Journal*, 9(2):92–96, 2000.

[285] Y. S. Nosikova, J. P. Santerre, M. Grynpas, G. Gibson, and R. A. Kandel. Characterization of the annulus fibrosus-vertebral body interface: Identification of new structural features. *Journal of Anatomy*, 221(6):577–589, 2012.

[286] A. Maroudas, R. A. Stockwell, A. Nachemson, and J. Urban. Factors involved in the nutrition of the human lumbar intervertebral disc: cellularity and diffusion of glucose in vitro. *Journal of Anatomy*, 120(1):113–130, 1975.

[287] Bin Fu, Huaye Jiang, Yanjun Che, Huilin Yang, and Zongping Luo. Microanatomy of the lumbar vertebral bony endplate of rats using scanning electron microscopy. *Orthopaedics and Traumatology: Surgery and Research*, 106(4):731–734, 2020.

[288] J. Wong, S. L. Sampson, H. Bell-Briones, A. Ouyang, A. A. Lazar, J. C. Lotz, and A. J. Fields. Nutrient supply and nucleus pulposus cell function: effects of the transport properties of the cartilage endplate and potential implications for intradiscal biologic therapy. *Osteoarthritis and Cartilage*, 27(6):956–964, 2019.

[289] Sadaaki Oki, Yoshiro Matsuda, Toshio Itoh, Taihoh Shibata, Hideo Okumura, and Junzo Desaki. Scanning electron microscopic observations of the vascular structure of vertebral end-plates in rabbits. *Journal of Orthopaedic Research*, 12(3):447–449, 1994.

[290] Sheen Gurrib. *Characterisation of Ovine and Human Vertebral Endplates using X-ray Microtomography : the Effects of Degeneration on Structure .* PhD thesis, University of Cambridge, 2020.

[291] Maximilian Rudert and Bemhard Tillmann. Lymph and blood supply of the human intervertebral disc: Cadaver study of correlations to discitis. *Acta Orthopaedica Scandinavica*, 64(1):37–40, 1993.

[292] Nadja A. Farshad-Amacker, Alexander Hughes, Richard J. Herzog, Burkhardt Seifert, and Mazda Farshad. The intervertebral disc, the endplates and the vertebral bone marrow as a unit in the process of degeneration. *European Radiology*, 27(6):2507–2520, 2017.

[293] W. Johannessen, J. D. Auerback, A. J. Wheaton, A. Kurji, A. Borthakur, R. Reddy, and D. M. Elliott. Assessment of Human Disc Degeneration and Proteoglycan Content Using T1-weighted Magnetic Resonance Imaging. *Spine*, 31(11):1253–1257, 2006.

[294] C. W. A. Pfirrmann, A. Metzdorf, M. Zanetti, J. Hodler, and N. Boos. Magnetic Resonance Classification of Lumbar Intervertebral Disc Degeneration. *Spine*, 26(17):1873–1878, 2001.

[295] Azucena G. Rodriguez, Chloe K. Slichter, Frank L. Acosta, Ana E. Rodriguez-Soto, Andrew J. Burghardt, Sharmila Majumdar, and Jeffrey C. Lotz. Human disc nucleus properties and vertebral endplate permeability. *Spine*, 36(7):512–520, 2011.

[296] L. J. Melton, A. W. Lane, C. Cooper, R. Eastell, W. M. O'Fallon, and B. L. Riggs. Prevalence and incidence of vertebral deformities. *Osteoporosis International*, 3(3):113–119, 1993.

[297] Michael C. Nevitt, Steven R. Cummings, Katie L. Stone, Lisa Palermo, Dennis M. Black, Douglas C. Bauer, Harry K. Genant, Marc C. Hochberg, Kristine E. Ensrud, Teresa A. Hillier, and Jane A. Cauley. Risk Factors for a First-Incident Radiographic Vertebral Fracture in Women $\geq$65 Years of Age: The Study of Osteoporotic Fractures. *Journal of Bone and Mineral Research*, 20(1):131–140, 2004.

[298] T. W. O'Neill, D. Felsenbergp, J. Varlow, et al. The prevalence of vertebral deformity in european men and women: The European vertebral osteoporosis study. *Journal of Bone and Mineral Research*, 11(7):1010–1018, 1996.

[299] Felix Repp, Philip Kollmannsberger, Andreas Roschger, Andrea Berzlanovich, Gerlinde M. Gruber, Paul Roschger, Wolfgang Wagermaier, and Richard Weinkamer. Coalignment of osteocyte canaliculi and collagen

fibers in human osteonal bone. *Journal of Structural Biology*, 199(3):177–186, 2017.

[300] Felix Repp, Philip Kollmannsberger, Andreas Roschger, Michael Kerschnitzki, Andrea Berzlanovich, Gerlinde Gruber, Paul Roschger, Wolfgang Wagermaier, and Richard Weinkamer. Spatial heterogeneity in the canalicular density of the osteocyte network in human osteons. *Bone Reports*, 6:101–108, 2017.

[301] Sarah L. Dallas and David S. Moore. Using confocal imaging approaches to understand the structure and function of osteocytes and the lacunocanalicular network. *Bone*, 138, 2020.

[302] Alexander F. van Tol, A. Roschger, F. Repp, J. Chen, P. Roschger, A. Berzlanovich, G. M. Gruber, P. Fratzl, and Richard Weinkamer. Network architecture strongly influences the fluid flow pattern through the lacunocanalicular network in human osteons. *Biomechanics and Modeling in Mechanobiology*, 19(3):823–840, 2020.

[303] Jessica C. Mansfield and C. Peter Winlove. A multi-modal multiphoton investigation of microstructure in the deep zone and calcified cartilage. *Journal of Anatomy*, 220(4):405–416, 2012.

[304] R. A. Stockwell. Cartilage failure in osteoarthritis: Relevance of normal structure and function. A review. *Clinical Anatomy*, 4(3):161–191, 1991.

[305] Laurence Van Gulick, Charles Saby, Hamid Morjani, and Abdelilah Beljebbar. Age-related changes in molecular organization of type I collagen in tendon as probed by polarized SHG and Raman microspectroscopy. *Scientific Reports*, 9(1):1–12, 2019.

[306] Mahmoud Mageed, Dagmar Berner, Henriette Jülke, Christian Hohaus, Walter Brehm, and Kerstin Gerlach. Is sheep lumbar spine a suitable alternative model for human spinal researches? Morphometrical comparison study. *Laboratory Animal Research*, 29(4), 2013.

[307] Maxim Bashkuev, Sandra Reitmaier, and Hendrik Schmidt. Is the sheep a suitable model to study the mechanical alterations of disc degeneration in humans? A probabilistic finite element model study. *Journal of Biomechanics*, 84:172–182, 2019.

[308] Sandra Reitmaier, Hendrik Schmidt, Renate Ihler, Tugrul Kocak, Nicolas Graf, Anita Ignatius, and Hans Joachim Wilke. Preliminary Investigations on Intradiscal Pressures during Daily Activities: An In Vivo Study Using the Merino Sheep. *PLoS ONE*, 8(7):1–10, 2013.

[309] Michael Kerschnitzki, Wolfgang Wagermaier, Paul Roschger, Jong Seto, Ron Shahar, Georg N. Duda, Stefan Mundlos, and Peter Fratzl. The organization of the osteocyte network mirrors the extracellular matrix orientation in bone. *Journal of Structural Biology*, 173(2):303–311, 2011.

[310] Felix Repp. *Computational Analysis of Dynamic Bone Structure and Processes – Osteocyte Networks & Healing –*. PhD thesis, Mathematisch-Naturwissenschaftlichen Fakultät der Humboldt-Universität zu Berlin, 2015.

[311] Felix Repp. Tool for Image and Network Analysis https://bitbucket.org/refelix/tina/src/master/, 2017. Accessed: September 2020.

[312] Michael Kerschnitzki, Philip Kollmannsberger, Manfred Burghammer, Georg N. Duda, Richard Weinkamer, Wolfgang Wagermaier, and Peter

Fratzl. Architecture of the osteocyte network correlates with bone material quality. *Journal of Bone and Mineral Research*, 28(8):1837–1845, 2013.

[313] Richard Weinkamer, Philip Kollmannsberger, and Peter Fratzl. Towards a Connectomic Description of the Osteocyte Lacunocanalicular Network in Bone. *Current Osteoporosis Reports*, 17(4):186–194, 2019.

[314] P. Dierckx. Algorithms for smoothing data with periodic and parametric splines. *Computer Graphics and Image Processing*, 20(2):171–184, 1982.

[315] Caitlyn J. Collins, Orestis G. Andriotis, Vedran Nedelkovski, Martin Frank, Orestis L. Katsamenis, and Philipp J. Thurner. Bone micro- and nanomechanics. In Roger Narayan, editor, *Encyclopedia of Biomedical Engineering*, pages 22–44. Elsevier, Oxford, 2019.

[316] Philip Kollmannsberger, Michael Kerschnitzki, Felix Repp, Wolfgang Wagermaier, Richard Weinkamer, and Peter Fratzl. The small world of osteocytes: Connectomics of the lacuno-canalicular network in bone. *New Journal of Physics*, 19(7), 2017.

[317] Quorum Technologies Ltd. *Q150V S / E / ES plus Instruction Manual*. Number 10. 2021.

[318] Joseph I. Goldstein, Dale E. Newbury, Patrick Echlin, David C. Joy, Charles Fiori, and Eric Lifshin. *Coating Techniques for SEM and Microanalysis*, pages 461–494. Springer US, Boston, MA, 1981.

[319] J. Heřt, P. Fiala, and M. Petrtýl. Osteon orientation of the diaphysis of the long bones in man. *Bone*, 15(3):269–277, 1994.

[320] Karolina Kliskey, Kelly Williams, J. Yu, David Jackson, Jill Urban, and Nick Athanasou. The presence and absence of lymphatic vessels in the adult human intervertebral disc: Relation to disc pathology. *Skeletal Radiology*, 38(12):1169–1173, 2009.

[321] T. G. Kashima, A. Dongre, and N. A. Athanasou. Lymphatic Involvement in Vertebral and Disc Pathology. *Spine (Phila Pa 1976)*, 36:899–904, 2011.

[322] J. Koivu and R. Myllylä. Interchain disulfide bond formation in types I and II procollagen. Evidence for a protein disulfide isomerase catalyzing bond formation. *Journal of Biological Chemistry*, 262(13):6159–6164, 1987.

[323] S. S. Margulies and K. L. Thibault. Infant skull and suture properties: Measurements and implications for mechanisms of pediatric brain injury. *Journal of Biomechanical Engineering*, 122(4):364–371, 2000.

[324] Lynne A. Opperman and Joseph T. Rawlins. The extracellular matrix environment in suture morphogenesis and growth. *Cells Tissues Organs*, 181(3-4):127–135, 2006.

[325] M. J. Baer. Patterns of growth of the skull as revealed by vital staining. *Human Biology*, 26:80–126, 1954.

[326] C. Jaslow. Mechanical Properties of Cranial Sutures. *Journal of Biomechanics*, 23(4):313–321, 1990.

[327] Borja Esteve-Altava, Toni Vallès-Català, Roger Guimerà, Marta Sales-Pardo, and Diego Rasskin-Gutman. Bone Fusion in Normal and Pathological Development is Constrained by the Network Architecture of the Human Skull. *Scientific Reports*, 7(1):1–7, 2017.

[328] Sanjin Idriz, Jaymin H. Patel, Seyed Ameli Renani, Rosemary Allan, and Ioannis Vlahos. CT of Normal Developmental and Variant Anatomy of the Pediatric Skull: Distinguishing Trauma from Normality. *RadioGraphics*, 35(5), 2015.

[329] M. Barszcz and K. Woźniak. Complete sagittal suture closure evaluation based on post mortem computed tomography. *Legal Medicine*, 52, 2021.

[330] Stephen R. F. Twigg and Andrew O. M. Wilkie. A Genetic-Pathophysiological Framework for Craniosynostosis. *American Journal of Human Genetics*, 97(3):359–377, 2015.

[331] R. H. Khonsari, F. Di Rocco, É Arnaud, S. Sanchez, and P. Tafforeau. High-resolution imaging of craniofacial sutures: New tools for understanding the origins of craniosynostoses. *Child's Nervous System*, 28(9):1465–1469, 2012.

[332] Stephen M. Warren, Benjamin Walder, Wojciech Dec, Michael T. Longaker, and Kang Ting. Confocal Laser Scanning Microscopic Analysis of Collagen Scaffolding Patterns in Cranial Sutures. *J Craniofac Surg.*, 19(1):198–203, 2008.

[333] Annemarie K. Leonard, Elizabeth A. Loughran, Yuliya Klymenko, Yueying Liu, Oleg Kim, Marwa Asem, Kevin Mcabee, Matthew J. Ravosa, and M. Sharon. Methods for the visualization and analysis of extracellular matrix protein structure and degradation. *Methods Cell Biol.*, 143:79–95, 2018.

[334] Marie Andrée Houle, Charles André Couture, Stéphane Bancelin, Jarno Van der Kolk, Etienne Auger, Cameron Brown, Konstantin Popov, Lora Ramunno, and François Légaré. Analysis of forward and backward Second

Harmonic Generation images to probe the nanoscale structure of collagen within bone and cartilage. *Journal of Biophotonics*, 8(11-12):993–1001, 2015.

[335] Tengteng Tang, Wolfgang Wagermaier, Roman Schuetz, Qiong Wang, Felipe Eltit, Peter Fratzl, and Rizhi Wang. Hypermineralization in the femoral neck of the elderly. *Acta Biomaterialia*, 89:330–342, 2019.

[336] P. Roschger, P. Fratzl, J. Eschberger, and K. Klaushofer. Validation of quantitative backscattered electron imaging for the measurement of mineral density distribution in human bone biopsies. *Bone*, 23(4):319–326, 1998.

[337] John G. Skedros, Jennifer L. Holmes, Eric G. Vajda, and Roy D. Bloebaum. Cement lines of secondary osteons in human bone are not mineral-deficient: New data in a historical perspective. *Anatomical Record - Part A Discoveries in Molecular, Cellular, and Evolutionary Biology*, 286(1):781–803, 2005.

[338] Pei Dong, Sylvain Haupert, Bernhard Hesse, Max Langer, Pierre Jean Gouttenoire, Valérie Bousson, and Françoise Peyrin. 3D osteocyte lacunar morphometric properties and distributions in human femoral cortical bone using synchrotron radiation micro-CT images. *Bone*, 60:172–185, 2014.

[339] Elliott Goff, Federica Buccino, Chiara Bregoli, Jonathan P. McKinley, Basil Aeppli, Robert R Recker, Elizabeth Shane, Adi Cohen, Gisela Kuhn, and Ralph Müller. Large-scale quantification of human osteocyte lacunar morphological biomarkers as assessed by ultra-high-resolution desktop micro-computed tomography. *Bone*, 152, 2021.

[340] Linda C. P. Croton, Kaye S. Morgan, David M. Paganin, Lauren T. Kerr, Megan J. Wallace, Kelly J. Crossley, Suzanne L. Miller, Naoto Yagi, Kentaro Uesugi, Stuart B. Hooper, and Marcus J. Kitchen. In situ phase contrast X-ray brain CT. *Scientific Reports*, 8:1–12, 2018.

[341] Stephan Preibisch, Stephan Saalfeld, and Pavel Tomancak. Globally optimal stitching of tiled 3D microscopic image acquisitions. *Bioinformatics*, 25(11):1463–1465, 2009.

[342] Johannes Schindelin, Ignacio Arganda-Carreras, Erwin Frise, Verena Kaynig, Mark Longair, Tobias Pietzsch, Stephan Preibisch, Curtis Rueden, Stephan Saalfeld, Benjamin Schmid, Jean Yves Tinevez, Daniel James White, Volker Hartenstein, Kevin Eliceiri, Pavel Tomancak, and Albert Cardona. Fiji: An open-source platform for biological-image analysis. *Nature Methods*, 9(7):676–682, 2012.

[343] Markus A. Hartmann, Stéphane Blouin, Barbara M. Misof, Nadja Fratzl-Zelman, Paul Roschger, Andrea Berzlanovich, Gerlinde M. Gruber, Peter C. Brugger, Jochen Zwerina, and Peter Fratzl. Quantitative Backscattered Electron Imaging of Bone Using a Thermionic or a Field Emission Electron Source. *Calcified Tissue International*, 109(2):190–202, 2021.

[344] P. Roschger, H. Plenk Jr, K. Klaushofer, and J. Eschbeger. A new scanning electron microscopy approach to the quantification of bone mineral distribution: backscattered electron image grey-levels correlated to calcium K alpha-line intensities. *Scanning Microscopy*, 9:75–88, 1995.

[345] M. A. Hayat. *Principles and Techniques of Electron Microscopy Biological Applications*. Edward Arnolds, 1981.

[346] MATLAB. *version 9.4.0.8 (R2018a)*. The MathWorks Inc., Natick, Massachusetts, 2018.

[347] Habibah T. U., Amlani D. V., and Brizuela M. *Hydroxyapatite Dental Material*. StatPearls Publishing, 2022.

[348] Victoria Schemenz, André Gjardy, Fereshteh F Chamasemani, Andreas Roschger, Paul Roschger, Paul Zaslansky, Lukas Helfen, Manfred Burghammer, Peter Fratzl, Richard Weinkamer, Roland Brunner, Bettina M Willie, and Wolfgang Wagermaier. Heterogeneity of the osteocyte lacunocanalicular network architecture and material characteristics across different tissue types in healing bone. *Journal of Structural Biology*, 212(2), 2020.

[349] K. M. Delahunty, L. G. Horton, H. F. Coombs III, K. L. Shultz, K. L. Svenson, M. A. Marion, M. F. Holick, W. G. Beamer, and C. J. Rosen. Gender and compartment specific bone loss in C57BL/6J mice: correlation to season? *J Clin Densitom*, 12(1):89–94, 2009.

[350] G. Mabilleau, A. Mieczkowska, H. Libouban, Y. Simon, M. Audran, and Daniel Chappard. Comparison between quantitative X-ray imaging, dual energy X-ray absorptiometry and microCT in the assessment of bone mineral density in disuse-induced bone loss. *Journal of Musculoskeletal Neuronal Interactions*, 15(1):42–52, 2015.

[351] Keita Nishi, Daisuke Endo, Takashi Hasegawa, Takefumi Moriuchi, Keiko Ogami-Takamura, Kazunobu Saiki, Kiyohito Murai, Toshio Higashi, Toshiyuki Tsurumoto, Yoshitaka Manabe, and Joichi Oyamada. Similarities and Differences in Bone Mineral Density between Multiple Sites in the

Same Individual: An Elderly Cadaveric Study. *BioMed Research International*, 2022, 2022.

[352] Zengqian Liu, Marc A. Meyers, Zhefeng Zhang, and Robert O. Ritchie. Functional gradients and heterogeneities in biological materials: Design principles, functions, and bioinspired applications. *Progress in Materials Science*, 88:467–498, 2017.

[353] Robert O. Ritchie, Markus J. Buehler, and Paul Hansma. Plasticity and toughness in bone. *Physics Today*, 62(6):41–47, 2009.

[354] X. W. Su, Q. L. Feng, F. Z. Cui, and X. D. Zhu. Microstructure and micromechanical properties of the mid-diaphyses of human fetal femurs. *Connective Tissue Research*, 36(3):271–286, 1997.

[355] Emily G. Pendleton, Kayvan F. Tehrani, Ruth P. Barrow, and Luke J. Mortensen. Second harmonic generation characterization of collagen in whole bone. *Biomedical Optics Express*, 11(8), 2020.

[356] Daniela Farke, Carsten Staszyk, Klaus Failing, Robert M. Kirberger, and Martin J. Schmidt. Sensitivity and specificity of magnetic resonance imaging and computed tomography for the determination of the developmental state of cranial sutures and synchondroses in the dog. *BMC Veterinary Research*, 15(1):1–14, 2019.

[357] S. Weiner, T. Arad, I. Sabanay, and W. Traub. Rotated plywood structure of primary lamellar bone in the rat: Orientations of the collagen fibril arrays. *Bone*, 20(6):509–514, 1997.

[358] S. Weiner and H. D. Wagner. The material bone: Structure-mechanical function relations. *Annual Review of Materials Science*, 28(1):271–298, 1998.

[359] Charles H. Turner, M. R. Forwood, J. Y. Rho, and T. Yoshikawa. Mechanical loading thresholds for lamellar and woven bone formation. *Journal of Bone and Mineral Research*, 9(1):87–97, 1994.

[360] Susanne Schrof, Peter Varga, Leonardo Galvis, Kay Raum, and Admir Masic. 3D Raman mapping of the collagen fibril orientation in human osteonal lamellae. *Journal of structural biology*, 187(3):266–275, 2014.

[361] Jean E. Aaron. Periosteal Sharpey's fibers: A novel bone matrix regulatory system. *Frontiers in Endocrinology*, 3:1–10, 2012.

[362] J. I. Goldstein, D. E. Newbury, D. C. Joy, C. E. Lyman, P. Echlin, E. Lifshin, L. Sawyer, and J. R. Michael. *Scanning Electron Microscopy and X-Ray Microanalysis: Third Edition*. Scanning Electron Microscopy and X-ray Microanalysis. Springer US, 2003.

[363] Tomasz Glawdel, Zeyad Almutairi, Shuwen Wang, and Carolyn Ren. Photobleaching absorbed Rhodamine B to improve temperature measurements in PDMS microchannels. *Lab on a Chip*, 9(1):171–174, 2009.